Mathematical Modelling of the Czochralski Crystal Growth Process

Thesis Presented for the Degree of

DOCTOR OF PHILOSOPHY

in the Department of

Mathematics and Applied Mathematics

UNIVERSITY OF CAPE TOWN

Thomas W. Brakel, M.A.Sc., B.Sc.(Eng.)

Supervisor: Prof. T. G. Myers

Abstract

In this document a mathematical model for the Czochralski crystal growth process is developed. The trend in current research involves developing cumbersome numerical simulations that provide little or no understanding of the underlying physics. We attempt to review previous research methods, mainly devoted to silicon, and develop a novel analytical tool for indium antimonide (InSb) crystal growth. This process can be subdivided into two categories: solidification and fluid mechanics.

Thus far, crystal solidification of the Czochralski process has been described in the literature mainly qualitatively. There has been little work in calculating actual solidification dynamics. Czochralski crystal growth is a very sensitive process, particularly for InSb, so it is crucial to describe the system as accurately as possible. A novel 1D quasi-steady method is proposed for the shape and temperature field of an InSb crystal, incorporating the effects of the melt.

The fluid mechanics of the Czochralski melt have been modelled by numerous researchers, with calculations performed using commercial software. However, a description of the buoyancy and rotation interaction in the melt has not been adequately performed. Many authors have presented flow patterns but none have indicated either: melt conditions preferential for crystal growth or at least a description of a typical melt structure. In this work, a scale analysis is performed that implies an idealized flow structure. An asymptotic model is then derived based on this order of magnitude analysis, resulting in a fast and efficient fluid flow calculation. The asymptotic model is validated against a numerical solution to ensure that the macroscopic features of the flow structure are present. The asymptotic model does not show exact agreement, but does provide an estimate of the melt heat flux that is necessary for the solidification calculation. The asymptotic model is also used to predict macroscopic changes in the melt due to rotation.

Finally, the solidification and asymptotic fluid flow calculations are coupled to give

an overall process model. The applications of this model are numerous for the industrialist, allowing many process parameters to be calculated. Examples are presented where the crucible temperature, ambient gas temperature and of course the crystal shape are computed. If experimental data were available, such as temperature measurements, the resulting calculations could be used to optimize or upgrade the entire grower apparatus. This work is meant to be simple and efficient so the calculations can be run on any modern computer, by someone with a moderate mathematics background.

Acknowledgements

This project would not be possible without the financial contributions from Firebird Semiconductors, the University of British Columbia, the Pacific Institute of Mathematical Science and the South African National Research Foundation. I am very privileged to have been able to take part in this research with such financial support.

I would like to thank the following people. Ian Frigaard for his inspiration and mentorship throughout this project, it was a pleasure to have been under his supervision at UBC. Dominik Schötzau for bringing me up to speed in the Finite Element Method, his patience and enthusiasm. Bill Micklethwaite of Firebird Semiconductors for initiating this project and his never-ending curiosity. Jean Charpin pour son aide avec la méthode des différences finies, et pour ses gâteaux. And of course, Tim Myers for being more than a supervisor to me, also a dear friend.

Personally, I have to mention how wonderful the people of South Africa have treated me. Especially, Allan, Johan and Mary-Kate Versfeld for making me feel like a part of their family. Hiddingh Hall Rugby Club for definitely the most outrageous experiences during my stay. James Dallas for his words of wisdom and letting me drive his Audi. Monaheng, Drishti, Lehana and Seboko for my interesting stay at beautiful Liesbeeck Gardens. The staff at the Mathematics Department who were knowledgeable and efficient, particularly Mrs. Di Loureiro.

I would like to dedicate this Thesis to my family: Pieter, Hendrik and Betty, who have supported throughout my endeavours. I would never have made it this far if it was not for there unwavering love and support. Futhi ngithanda ukubonga isithandwa sami uThokozile. Ungifundise izinto eziningi, ukuthemba nothando. Angazi ukuthi bengizokwenza kanjani uma bekangekho.

I will never, ever forget these past three years in Cape Town.

T. W. Brakel

February 2006

Contents

1 Introduction - The Czochralski Crystal Growth Method **1**

1.1 Overview 1

1.1.1 History 1

1.1.2 Indium Antimonide (InSb) Crystal Growth 2

1.1.3 Thesis Objective 5

1.2 Crystal Solidification 7

1.3 Melt Fluid Mechanics 8

1.3.1 Model Boundaries 11

1.4 Summary 13

2 Crystal Solidification **15**

2.1 Previous Work and Motivation 16

2.2 Governing Equations 18

2.2.1 Averaged Temperature Model 21

2.3 Temperature Profiles and Solidification Rates 22

2.3.1 Cylindrical Crystals 23

2.3.2 Conical Crystals 26

2.3.3 Non-Standard Crystal Shapes in a Variable Temperature Gas 28

2.4 Time Dependent Equations 28
2.4.1 Derivation 29
2.5 Results 33
2.5.1 Model Validation 33
2.5.2 Variable Gas Temperature 36
2.6 Summary 38

3 Melt Fluid Mechanics I: Governing Equations **39**

3.1 Model Derivation 39
3.1.1 Axisymmetry 41
3.1.2 Time Independence 41
3.2 Non-Dimensionalization of Equations 42
3.3 Boundary Conditions 44
3.4 Scale Analysis 45
3.4.1 Crucible Wall 45
3.4.2 Crystal 50
3.5 Summary 52

4 Melt Fluid Mechanics II: Coupled Boundary Layer Model **54**

4.1 Previous Work and Motivation 55
4.2 Core Model 58
4.3 Crucible Boundary Layer 59
4.3.1 Coordinate Transformation 60

4.3.2 Similarity Substitution 62
4.3.3 Simplifications for Circular Geometry 63
4.4 Crystal Boundary Layer 65
4.4.1 Governing Equations for a Rotating Crystal 66
4.5 Model Closure 69
4.6 Results 70
4.6.1 Crucible Boundary Layer Calculations 70
4.6.2 Crystal Boundary Layer Calculations 72
4.6.3 Coupled Model with Crystal Growth Profile 73
4.7 Summary 75

5 Melt Fluid Mechanics III: Finite Element Solution **77**

5.1 Previous Work and Motivation 77
5.2 Geometry and Coordinate System 78
5.2.1 Discretization of Domain (Meshing) 78
5.2.2 Coordinate Transformation 79
5.2.3 Element Interpolation Functions 80
5.3 Weak Form 81
5.3.1 Finite Element Method 83
5.3.2 Linearization 85
5.4 Matrix Formulation 86
5.4.1 Relaxation Factor 88
5.5 Results for a Specified Flow Field 89

5.5.1 Solver Accuracy and Convergence 89
5.5.2 Heat Flux / Torque Calculation 91
5.5.3 Boundary Conditions for Melt Flow 94
5.6 Summary 95

6 Melt Structure and Coupled Boundary Layer Model Validation 96

6.1 Overview 96
6.2 FE Simulation Results I: The Effect of Buoyancy and Rotation 98
6.2.1 Structure of Crucible Flow 99
6.2.2 Radial Velocity (u_r) Profiles 100
6.2.3 Azimuthal Velocity (u_θ) Profiles 101
6.2.4 Axial Velocity (u_z) Profiles 102
6.2.5 Velocity Vectors (r, z) 103
6.2.6 Temperature (T) Profiles 104
6.2.7 Pressure (P) Profiles 105
6.3 Coupled Boundary Layer Model Validation 106
6.4 Temperature Gradient at the Crystal 112
6.5 Summary 113

7 Quasi-Steady Crystal Growth with Varying Parameters 114

7.1 Overview 115
7.2 FE Simulation Results II: Variable Crystal Radius and Melt Height . 116
7.2.1 Radial Velocity (u_r) Profiles 117
7.2.2 Azimuthal Velocity (u_θ) Profiles 118
7.2.3 Axial Velocity (u_z) Profiles 119

7.2.4 Velocity Vectors (r, z) . . . 120
7.2.5 Temperature (T) Profiles) . . . 121
7.2.6 Pressure (P) Profiles . . . 122
7.2.7 Temperature Gradient Comparison . . . 123
7.3 Transient Crucible Wall Temperature . . . 124
7.4 Transient Gas Temperature . . . 126
7.5 Crystal Shape Prediction . . . 127
7.6 Summary . . . 132

8 Conclusions and Future Work **133**
8.1 Solidification . . . 133
8.2 Fluid Mechanics . . . 134
8.3 Coupled Model . . . 135
8.4 Future Work . . . 136

A Crucible Boundary Layer Equations Derivation **138**
A.1 Similarity Solution . . . 138
A.1.1 S-Momentum Equation . . . 139
A.1.2 Energy Equation . . . 140
A.1.3 θ-Momentum Equation . . . 141
A.1.4 Summary . . . 141

Bibliography **141**

List of Figures

1.1 Schematic of InSb crystal grower (courtesy M. Ebbehoj UBC Mech. Eng.) 3

1.2 InSb crystal growth (photo courtesy Firebird Semiconductors Ltd.) . . . 4

1.3 The evolution of InSb crystal diameters 5

1.4 Schematic of InSb crucible with boundaries 12

2.1 InSb crystal grown at Firebird Semiconductors, Trail BC, Canada 18

2.2 InSb crystal geometry and linear fit (courtesy of Firebird Semiconductors) 18

2.3 Schematic of the solidification problem 19

2.4 Temperature variation in differently shaped crystals 27

2.5 Summary of numerical time-dependent solution 32

2.6 Results of 1D calculations at a) $t = 0.1$, b) $t = 0.5$, c) $t = 1.0$ 34

2.7 Solidification with melt recession 35

2.8 Results of 1D calculations at a) $t = 0.01$, b) $t = 0.05$, c) $t = 0.1$ 35

2.9 Time dependent crystal growth 36

2.10 Crystal profiles with varying ambient gas temperatures 37

3.1 Boundary conditions for crucible flow 44

3.2 Schematic of crucible with idealizations for scale analysis 46

3.3 Comparison of thermal and viscous boundary layers (adapted from [51]) . 49

3.4 Schematic of region underneath crystal for scale analysis 50

4.1 Schematic of coupled boundary layer flow regimes and boundary conditions 56

4.2 Schematic of crucible with coordinates normal and tangential to surface . 60

4.3 Schematic of momentum boundary layer underneath crystal 65

4.4 Crucible boundary layer profiles 71

4.5 Crystal boundary layer profiles 72

4.6 Input values for coupled calculation 73

4.7 Calculated core temperature and rotation rates 74

4.8 Comparison of heat flow and temperature gradient at crystal 75

5.1 Coarse mesh with 518 vertices and 294 elements and refined mesh with 1118 and 571 elements 79

5.2 Linear triangle (left) and quadratic triangle (right) used in calculations . . 81

5.3 Integration point locations 87

5.4 Results from test calculation 90

5.5 Temperature and azimuthal velocity gradients at $z = 1$ 93

5.6 Temperature and azimuthal gradients along crucible wall 93

5.7 Boundary conditions for 2D axisymmetric finite element model 95

6.1 Simulated radial velocity profiles 100

6.2 Simulated azimuthal velocity profiles 101

6.3 Simulated axial velocity profiles 102

6.4 Simulated velocity fields (r, z) 103

6.5 Simulated temperature fields 104

6.6 Simulated pressure fields 105

6.7 Integrated temperature gradients at crystal and crucible 108
6.8 Integrated azimuthal velocity gradients at crystal and crucible 109
6.9 Temperature gradients at crystal 109
6.10 Temperature gradients at crucible 110
6.11 Azimuthal velocity gradients at crystal 111
6.12 Azimuthal velocity gradients at crucible 111
6.13 Temperature gradient profiles at crystal 112

7.1 Radial velocity profiles 117
7.2 Azimuthal velocity profiles 118
7.3 Axial velocity profiles 119
7.4 Velocity vectors in (r, z) 120
7.5 Temperature profiles 121
7.6 Pressure profiles 122
7.7 Integrated temperature gradients at crystal 124
7.8 Supplied radial growth rates and melt heights 125
7.9 Calculated crucible wall temperature 125
7.10 Calculated and imposed crucible wall temperature 126
7.11 Surrounding gas temperature profile 127
7.12 Summary of algorithm for coupled calculation 128
7.13 Crystal calculations coupled with melt 129
7.14 Imposed profiles for final simulations 130
7.15 Crystal calculations coupled with melt 131

List of Tables

1.1 Non-dimensional numbers for InSb melt with grower parameters 9

2.1 Material properties and physical parameters 23

2.2 Non-dimensional simulation parameters 33

3.1 Material properties of liquid InSb and physical parameter values 49

5.1 Integration Points and Weights 87

5.2 Convergence of FE solver on test case 91

5.3 Non-dimensional heat flow and torque values for specified flow field 94

6.1 Parameters used in FE calculation of crucible flow 97

6.2 Simulation parameters for melt with Pr = 0.5 98

6.3 Simulation labels for flux / torque comparison 108

7.1 Crystal radius and melt heights for QS simulations 116

Chapter 1

Introduction - The Czochralski Crystal Growth Method

1.1 Overview

1.1.1 History

Over 80 years ago, Jan Czochralski was developing a process to measure the crystallization rate of different low-melting point metals (Sn, Pb, Zn). This was part of his work as chief of AEG's metals laboratory in Berlin. His idea was to dip a capillary into a crucible containing liquid metal, and pull the capillary upwards as the metal solidified. He realized the rate of withdrawal must be directly related to the solidification rate. He published this work in 1918 [1] and managed to pull wires of 0.2, 0.5 and 1 mm in diameter. These wires were exceptional because they were all single crystal wires; the metal atoms were arranged almost perfectly according to their crystal lattices. This new technique was described in his later work up until 1927 [2, 3, 4]. Although Czochralski had made a remarkable discovery, he did not

realize the full potential of his research.

In December of 1948, Teal and Little at Bell Laboratories in New Jersey, pulled their first single crystal of germanium from a melt. At this time there was little mention of Czochralski's work on solidification. In 1951, W. E. Buckley published his book [5] on crystal growth, making widespread acknowledgment to Czochralski for pulling metal single crystals from a liquid melt. There is still an ongoing debate whether Teal is the true originator of this process for making semiconductors [6] rather than Czochralski, but it seems clear Czochralski did have the idea of pulling crystals from a melt before Teal [7]. In either case, Teal made significant improvements that were critical to making high-quality semiconductor materials. His historic pulling of a germanium single crystal gave rise to the electronics revolution and is described in [8, 9].

Today, the Czochralski process is used for making large semiconductor crystals that are cut into wafers for the electronics industry. These wafers are then used to create all sorts of devices: light emitting diodes, integrated circuits, lasers, infra-red detectors, transistors, representing an industry in the billions of dollars annually.

1.1.2 Indium Antimonide (InSb) Crystal Growth

One of the crucial steps in processing InSb is to transform high-purity raw material into a low-defect, single crystal form, which is then used by electronics manufacturers. Indium antimonide is the material of choice, at the date of this publication, for infra-red sensors and emittors. The intrinsic ability of InSb to respond to infra-red radiation comes from its unique electronic structure. Extreme care and caution is required when attempting to manufacture any semiconductor crystal in order to ensure the electronic properties of the resulting material are homogeneous.

A schematic of a modern InSb crystal grower is shown in Figure 1.1. The crystal growth process can be summarized as follows. First, the high-purity solid charge is placed in the crucible and an InSb seed crystal is placed in the seed chuck (at the end

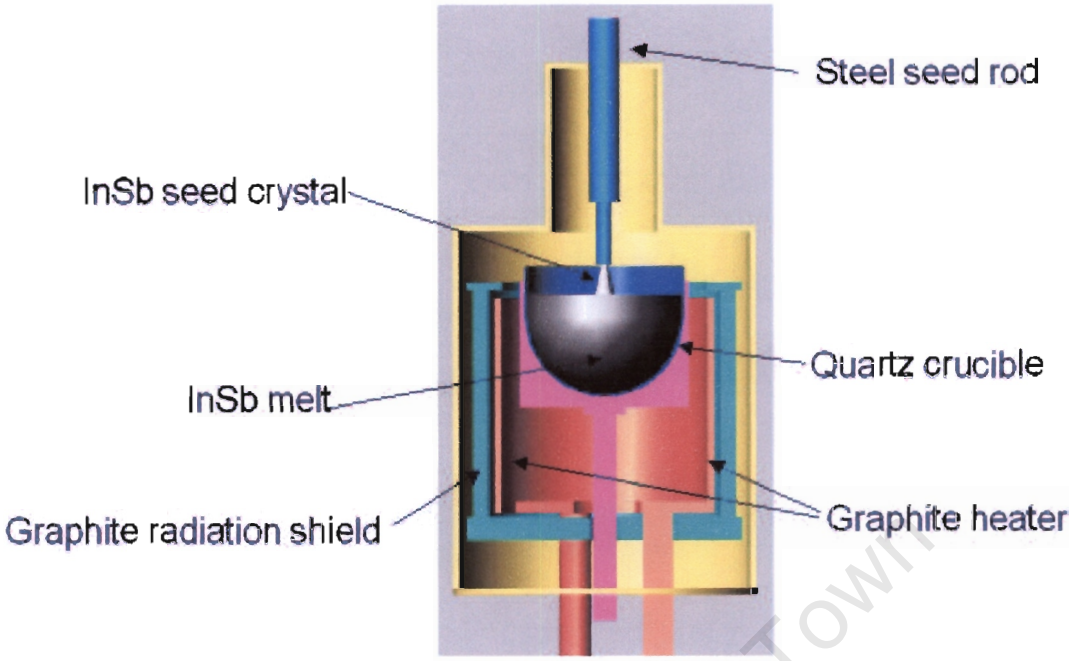

Figure 1.1: Schematic of InSb crystal grower (courtesy M. Ebbehoj UBC Mech. Eng.)

of the seed rod). Quartz is used for the crucible material because it does not react with InSb. The grower is then sealed and hydrogen is pumped into the chamber to create a non-oxidizing environment. The graphite heaters are then activated to melt the InSb charge. Once the melt is at the desired temperature, the seed rod is lowered, dipping the seed crystal into the melt and then slowly pulled upwards. The speed of growth may vary but is approximately 2 cm per hour. The crystal and crucible are constantly counter-rotated, to ensure even heating and circulation of the melt. Figure 1.2 shows an InSb crystal being pulled from the melt, viewed through a viewing window.

Silicon has dominated the semiconductor research arena so far, since it is commonly used in integrated circuits. InSb and Si crystals are grown in a similar manner, but there are several differences. The main difference arises from the crystallography, which makes it more difficult to grow InSb single crystals. In addition, InSb has more extreme material properties than other semiconductors. The chapter by

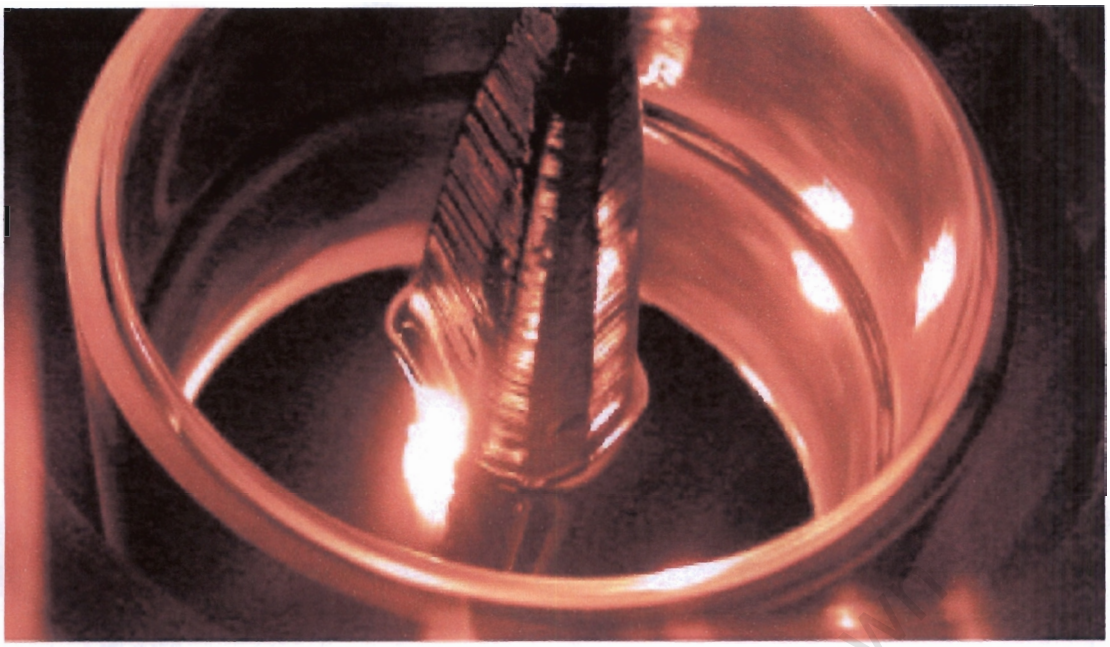

Figure 1.2: InSb crystal growth (photo courtesy Firebird Semiconductors Ltd.)

Micklethwaite [10] provides a detailed discussion of the crystallography, properties and other features of InSb. The importance for this thesis is that InSb crystals are smaller and grown under different conditions than Si. Since Si crystals are much larger (see [10] for a comparison of crystal sizes), the size of the crucible and the melt volume are much greater, resulting in a turbulent flow field. The geometry and rotation rates for InSb crystal growth imply the flow should be laminar but the low viscosity makes this uncertain. At the dimensions currently used with InSb, the melt flow field is very unlikely to be turbulent and appears laminar from inspection. A more detailed estimate, performed in Chapter 3, reveals that the flow is likely transitional.

A less obvious difference between Si and InSb is the amount of technology developed specifically for making Si crystals. It is currently possible to purchase computer automated Si crystal growers, that use a magnetic field to stabilize the melt. The book by Hurle [11] provides a thorough overview of the Czochralski process with some of the modern enhancements, while Lan's work [12] gives an account of the most recent developments in modelling and simulation of the entire process. In

comparison, there are currently no commercial growers for InSb at the time of this publication. InSb is currently being produced on a relatively small scale since the process is still not fully understood. There are still uncertainties about making high-purity, low-defect InSb crystals. Figure 1.3 shows the evolution of InSb crystal diameter in production over the past decade. The most recent milestone is the capability to produce crystals 100 mm in diameter. A deeper understanding of the underlying physics would likely lead to the ability to make larger crystals, which would be of significant technological benefit.

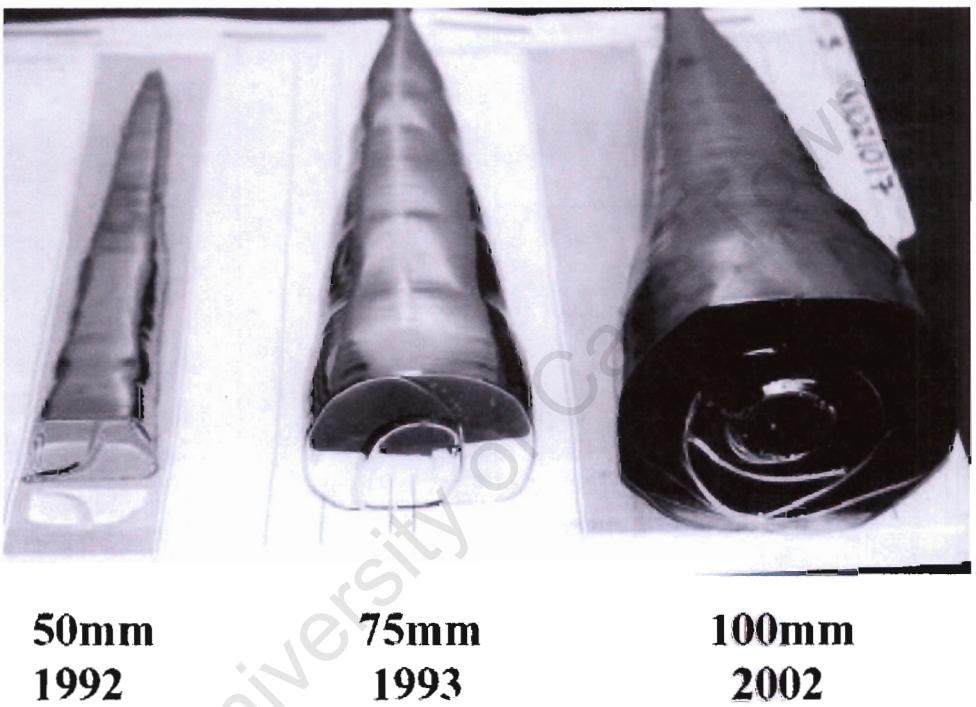

Figure 1.3: The evolution of InSb crystal diameters

1.1.3 Thesis Objective

The goal of this thesis is to develop a mathematical model of the overall Czochralski crystal growth process to further our understanding and to help producers make larger crystals. This requires a multi-disciplinary approach to determine what factors influence the crystal shape and quality. It is necessary to study each part of

the crystal growth process to understand the effect of control parameters.

The first and most obvious place to start is by examining the crystal itself. It is necessary to model the thermal behaviour and solidification dynamics since these determine the crystal growth rate. The result is a simplified calculation that engineers can use to describe the process parameters without resorting to expensive commercial software. The important or sensitive features of the process can then be identified.

This analysis would not be complete without looking at the melt fluid mechanics and heat transfer. We initially approach this problem with an asymptotic framework, hypothesizing a structure of the melt flow. By estimating the magnitude of the different forces we will construct an approximation of the flow field. Some of the melt conditions are idealized, but we are mainly interested in the macroscopic trends and developing a more fundamental understanding of the melt. In particular, we attempt to encapsulate the effects of the crystal rotation, crucible rotation and buoyancy of this system into a single model. We also seek to understand how the flow field changes with these parameters. It will become clear that the Czochralski melt flow is surprisingly complex.

No asymptotic model can be useful without being validated. The Finite Element (FE) Method is then used to solve the full equations and verify the asymptotic assumptions. There is one caveat to the numerical analysis: any numerical scheme is likely to be unstable at the actual process parameters. As mentioned previously, the flow is likely transitional and the low Pr number makes the flow field very difficult to solve numerically. The approach that we take is to validate the asymptotic model at a higher viscosity and hope that it holds at the actual, lower value. In any case, qualitative trends of the melt flow field can be obtained. It should be noted that a commercial CFD software package was initially used and gave unsatisfactory results, particularly at low Pr numbers. A FE solution was subsequently implemented so that explicit control of the solving methods and matrices was readily available.

Chapter 2 comprises the derivation and implementation of the solidification model, with results showing the effect of melt recession and with a varying gas temperature. In Chapter 3, the Navier-Stokes equations are non-dimensionalized and a scale analysis is performed that implies the presence of a boundary layer at the crucible wall and underneath the crystal. In Chapter 4, we develop an asymptotic model for the melt flow field, based on the scale analysis and assuming the presence of boundary layers. Results are presented for the boundary layer equations and for a specified crystal profile. Chapter 5 describes the derivation of the Finite Element approximation to the full Navier-Stokes equations. A test calculation is performed with a specified solution to show the accuracy of the solver. Chapter 6 is a compilation of all the results for the melt flow, including a description of the effects of buoyancy and rotation. A comparison between the asymptotic and numerical results is also presented. In Chapter 7, calculations of the overall crystal growth process are performed by coupling the solidification and melt flow. Chapter 8 provides the conclusions and a summary of the key findings in this research. We draw to a close by proposing future research ideas that could be pursued.

We now proceed by separating the analysis of the Czochralski process into two areas: solidification and fluid mechanics.

1.2 Crystal Solidification

The crystal solidification is a dynamic process that depends on many factors. Neglecting the melt momentarily, there are several features that affect crystal growth that are difficult to model, such as the surrounding gas temperature [13], the crystal/melt interface shape [14] and radiative heat transfer [15], to name the most prominent. Muller provides a more detailed description [16] of the challenges facing the crystal modelling community. Any attempt to combine all of these effects will produce an exhausting numerical model.

The main objection to performing such a huge calculation is that the results usually

provide little information in terms of a fundamental understanding of the process. There is also the question of the feasibility of solving a huge system of equations. The approach taken in this work is to include only the dominant forces in the model to see how they affect the overall crystal solidification. It is our goal to develop a solidification model that captures the governing physics and an engineer can solve on a personal computer in a reasonable amount of time. Furthermore, we intend to couple the solidification model with the melt fluid mechanics, thus requiring a rapid and efficient computation.

As shown in Figure 1.2, the resulting InSb crystal is not axisymmetric, however we wish to avoid modelling asymmetrical (3D) crystals. It is assumed that the crystal is 2D axisymmetric since the analysis of the crystallographic orientation during growth is the subject of intense research on its own, as discussed in [17]. The temperature field will be averaged in the radial direction, resulting in a one-dimensional profile, which avoids requiring a 2D/3D numerical scheme. Since the crystals are pulled very slowly, we will show the time dependence can be neglected and then make use of the quasi-steady assumption. Our analysis comprises the macroscopic growth features of the Czochralski crystal growth process, but we wish to also include the effects of the melt dynamics.

1.3 Melt Fluid Mechanics

Mathematical results of the Czochralski melt fluid mechanics were first published in the 1970s, the most notable by Kobayashi [18] and Langlois [19] for Si. These pioneering calculations provided the first detailed insight into melt convection. Although, these works did not have the advantage of the mathematical methods that came out in the late 80s for computational fluid dynamics and Finite Element methods for partial differential equations. The 1990s produced a wealth of numerical results for the Czochralski process, partly due to the increase in the computational ability of computers. Basu *et al* [20] provide a review of some of the 3D simulations

for Si and oxide melts that have been performed up until 2000. The most recent simulations include direct numerical simulation (DNS) of a turbulent melt, such as the work by Enger [21] and Wagner [22]. The majority of the research in Czochralski melts is relevant for Si or semiconductor oxide melts.

The flow field of a Czochralski melt must be assumed either laminar or turbulent a priori to performing any calculations. For current Si simulations, the melt is usually assumed fully developed turbulent flow, thus the numerical scheme will include a turbulence model to stabilize the solver. Oxide melts have a very high viscosity, making the numerical solutions well behaved. InSb melts are somewhere in between the laminar and turbulent regimes. They have a very low viscosity, similar to Si, but the process parameters indicate a laminar or transitional flow field.

To give the reader a feel for the flow properties of liquid InSb, typical non-dimensional numbers using process values are presented in Table 1.1. A range is presented where the value of the temperature difference or velocity is not exactly known.

Non-dimensional number	Value
Reynolds $(\mathrm{Re} = \frac{UR_c}{\nu})$	1000-5000
Prandtl $(\mathrm{Pr} = \frac{\nu}{\alpha})$	0.055
Boussinesq $(\mathrm{Bo} = \frac{R_c^3 g\beta\Delta T}{\alpha^2})$	$3 \times 10^5 - 5 \times 10^5$
Rayleigh number $(\mathrm{Ra} = \frac{R_c^3 g\beta\Delta T}{\alpha\nu})$	$4 \times 10^6 - 6 \times 10^6$
Grashof $(\mathrm{Gr} = \frac{R_c^3 g\beta\Delta T}{\nu^2})$	$7 \times 10^7 - 9 \times 10^7$

Table 1.1: Non-dimensional numbers for InSb melt with grower parameters

The Reynolds number can be described as the ratio of inertial forces to viscous forces. In simple flow fields a numerical estimate can be obtained for the onset of turbulence. Since the crucible melt comprises buoyancy and rotation, this transition occurs over a range of values and will depend on process parameters. The Prandtl number is simply the ratio of the fluid momentum diffusivity to the thermal diffusivity. The Boussinesq number comes from the heat equation (for a convective flow), it

can be described as the ratio of the fluid buoyancy to the thermal diffusivity. The Rayleigh number is associated with the heat transfer balance within the fluid. When the Rayleigh number is relatively low, the heat transfer is primary in the form of conduction; when it is large, heat transfer is primarily in the form of convection. The Grashof number represents the ratio of the buoyant forces to the viscous forces in a convective flow.

It should be made clear that the InSb fluid mechanics modeller has two choices. Either model the flow as laminar and expect the numerical solution to become unstable, or, model the flow as turbulent even though this may not be the case. In this work, the former choice was made in an attempt to be closer to the actual process.

There have also been attempts to solve fully coupled melt and gas flow equations for the entire grower. The gas flow and crucible melt profiles are then determined using only internal heating rates and grower boundary conditions. Earlier work by Van den Bogaert [23] and more recently by Lukanina [24] provide examples of these massive grower models. The down side to these calculations is they tend to be very time consuming and the geometry very restrictive, since significant work is required in meshing the entire system. These models account for the gas flow, but provide little physical insight to the melt fluid mechanics or crystal solidification. It is our intention to analyze and describe the structure of Czochralski InSb melts.

An asymptotic model is first presented to estimate some key quantities of the thermal and flow fields, using only the dominant forces. The asymptotic model can be easily modified for different process parameters that vary throughout the growth period. The basic premise is to assume the presence of a boundary layer at the crucible wall and underneath the crystal; and then couple them using conservation of energy and angular momentum. Since no meshing is required, the calculation time is relatively fast compared to a full numerical solution. The key question for the validity of the asymptotic model is: does the assumed structure really exist in an actual melt?

A Finite Element solution is also developed to resolve the velocity and temperature profiles within the crucible. There are two reasons for the numerical solution. First, for verifying if the structure assumed for the asymptotic model is valid or at least reasonable. Secondly, to show the different types of solutions that can exist, even if at slightly higher Pr numbers, under different crystal/crucible rotation. It is desirable to have some sort of picture of the melt flow field under crystal growing conditions. Unfortunately, the solver is unstable at actual Prandtl number and process parameters.

There is one feature of the Czochralski process that can dramatically simplify the calculations. The relatively slow pull rate has motivated many quasi-steady models for the crystal growth, and steady-state models for the melt fluid mechanics. There has been literature supporting the fact that small transients and anti-symmetric profiles can arise, as shown early by Kakimoto [25], and in the calculations by Enger [21] but the magnitude of these transients or fluctuations is negligible compared to the overall flow field. We will construct a steady-state melt calculation for the melt flow field that can be coupled to the solidification model. Our intent is to obtain an overall process model, not to calculate small fluctuations.

The other assumptions for the melt, such as the idealization of the geometry and boundary conditions, need to be discussed further before proceeding.

1.3.1 Model Boundaries

When modelling the crucible flow it is necessary to define the appropriate boundaries surrounding the melt. The main boundary enclosing the liquid InSb can be separated into four regions, as shown in Figure 1.4:

1. the crucible wall (R1)
2. the gas/melt interface (R2)
3. the crystal/melt interface (R3)

4. the axis of symmetry at the center (R4)

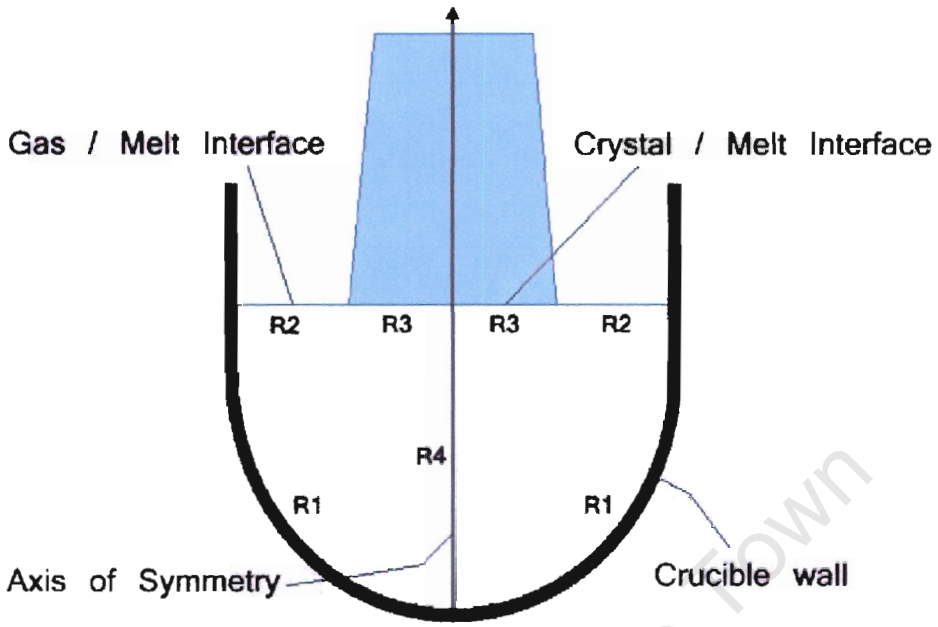

Figure 1.4: Schematic of InSb crucible with boundaries

The crucible is heated by graphite heaters, so the wall temperature is determined by a combination of radiation and convection. These features would over complicate our model, so we assume the crucible to be at a known temperature or at least has a specified temperature profile. This is also to make the model easily compatible with experimental data. For instance, if the crucible temperature profile were measured, it could easily be entered into our calculations. Unfortunately, at the present time, crucible temperature measurements are not available. For the velocity components we apply the no-slip condition at the crucible wall.

In an actual melt, the gas/melt interface is a free surface with a meniscus at the crystal and at the crucible wall. To simplify calculations, a fixed, horizontal surface is assumed. We also assume the gas/melt interface is unaffected by the fluid velocity and the surface tension is neglected. The height of the fluid decreases only due to the volume of liquid that has solidified. The heat transfer from the melt to the gas is relatively low, so the derivative of the temperature is assumed to be zero. Since

the amount of shear between the melt and gas will also be relatively small, no-shear is a reasonable assumption for this location.

The crystal/melt interface is also assumed horizontal and axisymmetric. The temperature of the crystal at this location must always be at the melting point of InSb. No-slip conditions are applied to the crystal face for the velocity components.

Only one half of the crucible is considered since it is assumed axisymmetric. In the case of the coupled boundary layer model, the center of the crucible is omitted because it does not directly contribute to heating or driving the melt. For the numerical calculation symmetry boundary conditions are applied: the gradients are zero for the temperature and vertical velocity component, but the radial and azimuthal velocity components must be zero.

This completes the general discussion for the fluid mechanics model of the Czochralski melt. More specific assumptions will be discussed later.

1.4 Summary

The inventive work of J. Czochralski and G. Teal have provided our generation with a myriad of modern electronic devices that still rely on their crystal pulling technique. The Czochralski crystal growth process continues to be a very active and challenging research field. The current trend is to construct numerical models in an attempt to model all of the physics and complexities inside the grower. However, there has been little description on how to improve the Czochralski process or discussion of the fundamental melt structure for InSb crystal growth.

This work is dedicated mainly to growing InSb crystals, but could be used for other semiconductor materials with similar properties. It is intended to increase the fundamental understanding of the overall process by describing the structure of the melt fluid mechanics, the crystal solidification and their interaction. We now proceed by deriving a 1D solidification model for the crystal, followed by an asymptotic and

numerical solution for the melt flow. The results of these calculations will be used to construct an overall description of the Czochralski crystal growth process.

Chapter 2

Crystal Solidification

It is crucial to have an understanding of the crystal solidification dynamics in order to accurately determine optimal process parameters. In particular, knowing the ideal crystal pull rate, thermal behaviour and radial growth rate can be invaluable when scaling up industrial equipment or trying to pull crystals of new materials. A mathematical model of the temperature field, vertical growth rate and radial growth rate is proposed to provide insight on these variables and their dependencies.

In this chapter, we analyze the temperature field in a Czochralski crystal and consequently determine the radial growth rate. To do this we exploit the fact that the radial temperature variation is small, thus allowing us to deal with an average temperature field. An approximate, pseudo-steady model is developed first and solutions are presented for cylindrical and conical crystals. A numerical solution for the fully time-dependent problem is then presented. Results are compared in order to validate the approximate solution. The extension of the method to arbitrarily shaped crystals is also discussed. The heat flux from the melt is estimated since it requires a more elaborate calculation, which is performed in Chapters 4 and 5.

2.1 Previous Work and Motivation

In the following work we will make two key approximations: the time-dependence and radial variation may be neglected in the crystal heat equation. Both approximations may be justified on physical and mathematical grounds. There are two reasons for taking this asymptotic approach, as opposed to solving the full equations numerically. First, we wish to clearly illustrate how the process parameters affect the crystal growth by looking at the dominant terms in the heat and solidification equations. Preliminary models by Hurle [26, 27] and Crowley [28] attempted to describe the solidification dynamics but did not accurately calculate the crystal temperature field. Secondly, since crystal growth depends significantly on the melt, we wish to couple the solidification model with a fluid mechanics calculation. Solving for the crystal temperature field and melt flow field numerically would be excessively time consuming. It is for these reasons we resort to a quasi-steady approach for the crystal growth.

Since the crystal is pulled at a slow rate (typically of the order 10^{-6}m/s), a pseudo or quasi-steady approximation is likely to hold, *i.e.* time drops out of the governing equation, but may remain in the boundary conditions. In this case, the physical interpretation is that the heat equilibrates over a much more rapid time-scale than motion occurs, hence we can partially uncouple the thermal problem from the solidification one. A number of authors have taken the pseudo-steady approach to predict other features of crystal growing. For example, Louchev [29] and Bohun [30] used a steady-state temperature profile to determine the thermal stress distribution in a crystal; while Wu [31] used a steady-state model to predict the crystal/melt interface shape. However, it was Derby and Brown who formalized the arguments as to the validity of this assumption [32] and is further discussed by Dupret [33]. Their arguments are based mainly on physical reasoning. The first goal of this work is to validate the argument from a mathematical viewpoint. In so doing we will be able to determine exactly what parameter or material property ranges are necessary

for this approximation to be valid.

The second approximation we will use is that the temperature is primarily one-dimensional. Van der Hart and Uelhoff argued, on physical grounds, that the radial dependence of the crystal temperature could be neglected [34]. This viewpoint is confirmed by the numerical work of Schvezov *et al* [35]. These authors used a Finite Element solution to produce 2D axisymmetric crystal temperature profiles for GaAs. Their results show that there is little temperature variation in the radial direction, with only a slight curvature appearing towards the edge of the crucible, with the curvature becoming more noticeable towards the melt. Tatarchenko [36] used a one-dimensional temperature profile but without formal justification. Recent results of Bohun *et al* [30] for InSb also show temperature profiles with a small radial variation, where they derive the one-dimensional relationship using an asymptotic expansion. In the following we will assume the radial variation is negligible, except perhaps in a thin region near the surface of the crystal in contact with the surrounding gas.

The use of the 1D crystal temperature profile has recently become prevalent in the literature by Louchev [29, 37], for estimating the axial stress in crystals. Louchev cites Indenbom's work [38] where the 1D equation was presented in Russian (and unavailable to the author). We will derive the 1D relationship and show the limiting factors to the quasi-steady assumption, which has yet to be presented.

Two shapes will be considered in the following analysis, cylindrical crystals with vertical sides (except for near the seed crystal) and conical crystals with linearly varying sides. It is current practice, for materials such as silicon (Si) to be grown primarily at constant radius, as can be seen at [39]. In contrast, other materials, such as InSb are grown in a highly conical shape, as shown in Figure 2.1. The process data in Figure 2.2 from Firebird Semiconductors shows that the radial profile of their InSb crystals is strongly linear, especially if the first data point is excluded. Although imposing such shapes is a limitation to our model, it is not useful to model (or fabricate) crystals with high curvature or strange shapes, we expect the geometry to deviate only slightly from this idealization.

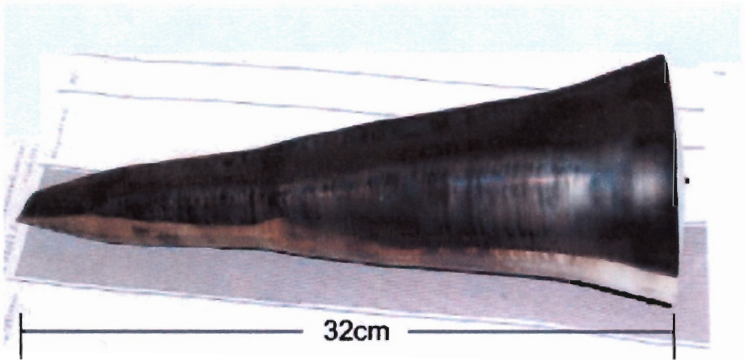

Figure 2.1: InSb crystal grown at Firebird Semiconductors, Trail BC, Canada

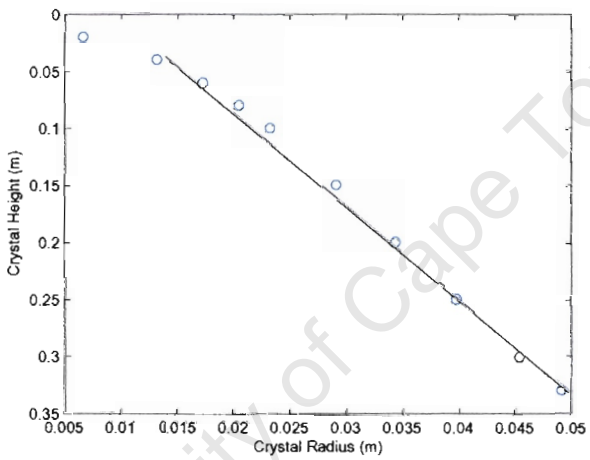

Figure 2.2: InSb crystal geometry and linear fit (courtesy of Firebird Semiconductors)

In the following section we will investigate the crystal temperature profile. Once determined, we can then look into the growth rate of a crystal, which is carried out in §2.3. Finally, we develop a numerical scheme of the fully time dependent problem to verify the approximations made in the analytical work.

2.2 Governing Equations

Consider the Czochralski crystal grower layout shown in Figure 2.3. The process involves pulling a seed crystal upward from the melt so that directional solidification

occurs. We choose a coordinate system moving with the seed crystal so that at time t the seed crystal is at position $z = 0$, the position of the crystal/melt interface is $z = b(t)$, the crystal radius at the melt is $r = a(t)$.

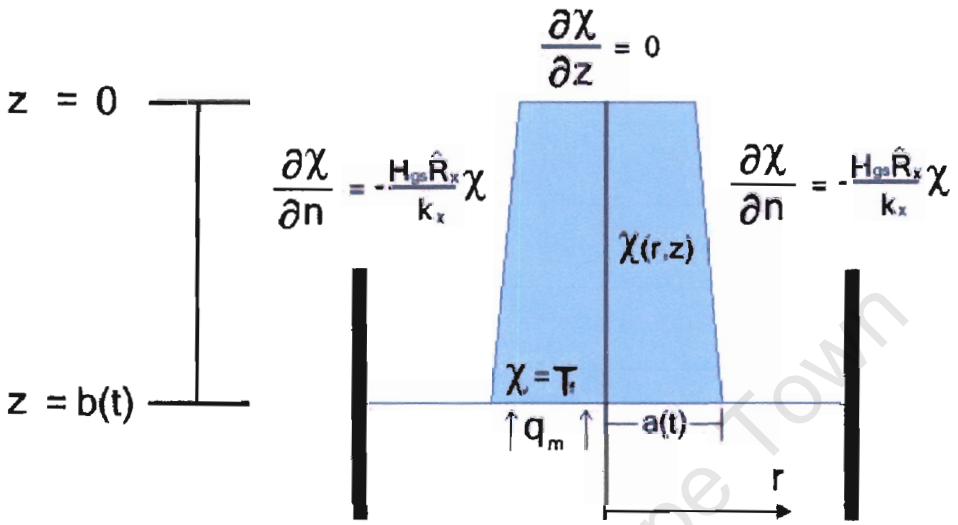

Figure 2.3: Schematic of the solidification problem

The crystal pull rate (and consequently the vertical growth rate) is specified, so our aim is to estimate the radial crystal growth rate. To do this requires knowledge of the crystal temperature field. In order to describe this situation mathematically, we must solve the heat equation in this region:

$$\frac{1}{\hat{r}}\frac{\partial}{\partial \hat{r}}\left(\hat{r}\frac{\partial \hat{\chi}}{\partial \hat{r}}\right) + \frac{\partial^2 \hat{\chi}}{\partial \hat{z}^2} = \frac{\rho_x c_x}{k_x}\frac{\partial \hat{\chi}}{\partial \hat{t}} \qquad 0 \le \hat{z} \le \hat{b}, \qquad 0 \le \hat{r} \le \hat{a}, \tag{2.1}$$

where hats denote dimensional variables. The crystal growth rate is determined by the Stefan condition

$$\frac{\rho_x L_f}{\hat{A}}\frac{\partial \hat{V}}{\partial \hat{t}} = k_x \frac{\partial \hat{\chi}}{\partial \hat{z}} - \hat{Q}_m \,, \tag{2.2}$$

where $\hat{A} = \hat{A}(\hat{t})$ is the cross-sectional area $\pi \hat{a}^2(\hat{t})$, $\hat{Q}_m$ is the heat flux from the melt and L_f is the latent heat of freezing. The expression for the volume $\hat{V}$ depends on the type of crystal (conical or cylindrical).

The next step is to non-dimensionalize equations (2.1) and (2.2) using typical values for the crystal radius ($\hat{R}_x$), crystal height ($\hat{L}_x$), crystal pull rate ($\hat{v}$), the surrounding gas temperature ($\hat{T}_g$) and the melting temperature of the solid ($\hat{T}_f$):

$$(r, a) = \frac{(\hat{r}, \hat{a})}{\hat{R}_x}, \qquad (z, b) = \frac{(\hat{z}, \hat{b})}{\hat{L}_x}, \qquad t = \left(\frac{\hat{v}}{\hat{L}_x}\right)\hat{t}, \qquad \chi = \frac{\hat{\chi} - \hat{T}_g}{\Delta\hat{T}}\ , \tag{2.3}$$

where $\Delta\hat{T} = \hat{T}_f - \hat{T}_g$. The area and volume become $A = \hat{A}/\pi\hat{R}_x^2$, $V = \hat{V}/\pi\hat{R}_x^2\hat{L}_x$, obviously for a cylindrical crystal $\hat{R}_x = \hat{a}$ is constant. The non-dimensional equations become:

$$\frac{1}{r}\frac{\partial}{\partial r}\left(r\frac{\partial\chi}{\partial r}\right) + \frac{\hat{R}_x^2}{\hat{L}_x^2}\frac{\partial^2\chi}{\partial z^2} = \frac{\rho_x c_x \hat{R}_x^2 \hat{v}}{k_x \hat{L}_x}\frac{\partial\chi}{\partial t} \qquad 0 \le z \le b\ , \tag{2.4}$$

$$\frac{\partial V}{\partial t} = a^2\left(S^{-1}\frac{\partial\chi}{\partial z} - q_m\right)\ , \tag{2.5}$$

where the Stefan number $S = \rho_x L_f \hat{L}_x \hat{v}/k_x\Delta T$ and $q_m = \hat{Q}_m/\rho_x L_f \hat{v}$.

The boundary conditions for this system are chosen as typical process values. At the solid/liquid interface ($z = b$), the temperature must remain at the non-dimensional freezing temperature of InSb ($\chi = 1$). At the surface of the crystal, the heat loss will be proportional to the difference between the surface and ambient temperature, in non-dimensional form:

$$k_x\frac{\partial\chi}{\partial n} = -H_{gs}\hat{R}_x\chi\ , \tag{2.6}$$

where H_{gs} is the heat transfer coefficient between the gas and the crystal. In the case where the ambient gas temperature varies along the surface the crystal, boundary condition (2.6) becomes

$$k_x\frac{\partial\chi}{\partial n} = H_{gs}\hat{R}_x(\chi_g(z) - \chi). \tag{2.7}$$

The temperature $\chi_g(z)$ will be used to model the scenario where the ambient gas is warmer near the melt and cooler towards the seed. At the top of the crystal ($z = 0$), where we assume no heat is lost ($\partial\chi/\partial z = 0$) since it is connected to an insulated seed chuck.

2.2.1 Averaged Temperature Model

The problem of solving for the temperature in the crystal can be significantly simplified by noting firstly that the temperature upon formation of new crystal is independent of r. This is reflected in the boundary condition that $\chi(r, b, t) = 1$ is constant. When the seed crystal is inserted there is also no radial variation in the temperature field. It therefore seems likely that in general the radial temperature variation is small, except perhaps in a thin layer at the outer edge of the crystal, which is specified by $r = s(z)$. This is exactly what is observed in the numerical calculations of [30, 35]. Hence, we now assume $\chi(r, z, t) \approx \chi(z, t)$ except for in the immediate vicinity of $r = s$.

Multiplying equation (2.4) by r and integrating with respect to r then gives

$$r\frac{\partial \chi}{\partial r}\bigg|_{r=0}^{r=s} + \frac{\hat{R}_x^2}{\hat{L}_x^2}\frac{\partial^2 \chi}{\partial z^2}\frac{s^2}{2} = \frac{\rho_x c_x \hat{R}_x^2 \hat{v}}{k_x \hat{L}_x}\frac{\partial \chi}{\partial t}\frac{s^2}{2} . \tag{2.8}$$

Note, in order to carry out this integration we have imposed the condition that the temperature is approximately independent of r. The only exception to this occurs near the crystal/gas interface, hence we retain the term involving $\frac{\partial \chi}{\partial r}$. This then permits us to take into account the surface cooling. To deal with this term requires two conditions. Firstly, within the crystal our approximation has $\frac{\partial \chi}{\partial r} = 0$ (however at $r = 0$ symmetry requires this even in the absence of the approximation) hence $\frac{\partial \chi}{\partial r} = 0$ at $r = 0$. At the surface of the crystal $r = s$, the convective heat transfer boundary condition (2.6) is applied. For the moment we will assume the ambient gas temperature is constant but later on we will apply condition (2.7) to allow the temperature to vary. Both of these conditions are in terms of the normal derivative, which we need to convert to the radial derivative.

The normal derivative may be written in terms of r and z:

$$\frac{\partial \chi}{\partial n} = \nabla \chi \cdot \hat{n} = \frac{1}{\sqrt{1 + (\partial r/\partial z)^2}}\left(\frac{\partial \chi}{\partial r} - \frac{\partial r}{\partial z}\frac{\partial \chi}{\partial z}\right) ,$$

where $\hat{n}$ is the unit normal. For a vertical sided crystal the radial co-ordinate and normal co-ordinate coincide and $\frac{\partial r}{\partial z} = 0$. For a linear crystal we may also neglect

terms involving $\frac{\partial r}{\partial z}$ provided the slope is steep. For a typical InSb crystal, as shown in Figure 2.2, $\frac{\partial r}{\partial z} \sim 0.13$, hence $\frac{\partial \chi}{\partial n} \approx \frac{\partial \chi}{\partial r}$. Substituting $\frac{\partial \chi}{\partial r}$ for the normal derivative and applying (2.6) to (2.8) results in

$$\gamma^2 s \frac{\partial^2 \chi}{\partial z^2} - \chi = \epsilon s \frac{\partial \chi}{\partial t} \qquad 0 \leq z \leq b \ , \tag{2.9}$$

where

$$\gamma^2 = \frac{\hat{R}_x k_x}{2 H_{gs} \hat{L}_x^2} \qquad \epsilon = \frac{\rho_x c_x \hat{R}_x \hat{v}}{2 H_{gs} \hat{L}_x} \ .$$

Using the data in Table 2.1 we see that for InSb $\gamma^2 \sim 0.17$, $\epsilon \sim 0.10$. In general, the time derivative is the smallest term in the equation, except at very small times. This is easily understood by considering the ratio $\epsilon/\gamma^2 \sim \hat{L}_x$. At the start of the process when the length is small, the time derivative dominates the equation, subsequently conduction in the z direction takes over. The switch in behaviour may also be seen in the crystal growth data of Figure 2.2, where the early growth behaviour, when $\hat{b} < 0.05$, differs from the subsequent growth.

In the following section we will exploit the fact that the time derivative is small and neglect this term. In effect, we are taking the leading order solution in an asymptotic expansion in terms of ϵ. This leads us to a pseudo-steady problem where time drops out of the governing equation but still appears in the position of the moving boundary $z = b(t)$. A similar approach has been successfully applied to ice growth in [40]. In §2.4 we will present a numerical solution of the problem to validate the results of this section and so justify the approximations.

2.3 Temperature Profiles and Solidification Rates

The temperature profile for a crystal is determined by equation (2.9). We now impose $\epsilon \ll 1$ and neglect terms of $\mathcal{O}(\epsilon)$. Note that, although γ^2 is also small, neglecting the diffusion term will prevent us from satisfying the boundary conditions at $z = 0$ and $z = b(t)$, hence we must retain this term.

Property	Symbol	Value	Units
		Solid InSb	
thermal conductivity	k_x	4.57	W/m/K
density	ρ_x	5640	kg/m^3
heat capacity	c_x	266	J/kg/K
latent heat of solidification	L_f	2.3×10^5	J/kg
melting temperature	$\hat{T}_f$	798	K
		Parameters	
maximum crystal radius	$\hat{R}_x$	0.05	m
maximum crystal length	$\hat{L}_x$	0.33	m
seed rod velocity	$\hat{v}$	5.56×10^{-6}	m/s
surrounding gas temperature	$\hat{T}_g$	648	K
heat transfer coefficient (gas)	H_{gs}	6.0	W/m^2/K

Table 2.1: Material properties and physical parameters

2.3.1 Cylindrical Crystals

In the case of cylindrical crystals, the radius is constant and it is unnecessary to calculate the radial growth rate. The aim here is to analyze the heat flow in the crystal to be able to predict the optimal and maximum crystal pull rate. Imposing a constant (non-dimensional) radius, $s = 1$, the problem reduces to a linear homogenous ODE for the temperature:

$$\gamma^2 \frac{\partial^2 \chi}{\partial z^2} - \chi = 0 \qquad 0 \leq z \leq b \; . \tag{2.10}$$

Applying appropriate boundary conditions, as shown in Figure 2.3,

$$\chi(b) = 1, \qquad \left.\frac{\partial \chi}{\partial z}\right|_{z=0} = 0 \tag{2.11}$$

we find

$$\chi(z) = \frac{\cosh(z/\gamma)}{\cosh(b/\gamma)} \; . \tag{2.12}$$

The temperature therefore decreases monotonically from the melt interface to the seed crystal.

With the temperature now known in the crystal we may turn our attention to the Stefan condition (2.5) which gives a relation between the growth rate and the heat fluxes into the crystal and the melt. The non-dimensional volume $V = b$ (since the non-dimensional radius $a = 1$) giving

$$\frac{\partial b}{\partial t} = S^{-1}\frac{\partial \chi}{\partial z} - q_m \ .$$

The fact that the heat conduction is significantly faster than the growth rate means that both $\frac{\partial \chi}{\partial z}$ and q_m can be determined from steady-state (or pseudo-steady at least) calculations. A steady-state calculation of the temperature field in the melt has been carried out in the numerical study of Kobayashi [41], and is performed in Chapters 4 and 6. For our current analysis it is sufficient to state that q_m is a known input parameter. The solution of the steady-state equation (2.10), given by (2.12), determines $\frac{\partial \chi}{\partial z}$. It is worth pointing out that the heat equations in the two regions, melt and crystal, are essentially uncoupled and may be solved separately. The only coupling comes through the mass transfer, so that as the crystal grows the melt shrinks and so the domain over which the heat equations are to be solved changes with time. The consequence for our current study is that we must take care in distinguishing between the growth rate $\frac{\partial b}{\partial t}$ and the pull rate v (which is unity in non-dimensional form).

If h represents the height of the fluid in the melt then the change in height due to crystal formation is given by a simple mass balance

$$-\rho_m A_m \frac{\partial h}{\partial t} = \rho_x A v = \rho_x \ ,$$

where m denotes melt properties. Since both the non-dimensional pull rate and radius are unity, the actual growth rate becomes

$$\frac{\partial b}{\partial t} = v - \frac{\partial h}{\partial t} = 1 + \frac{\rho_x}{\rho_m R_m^2} \ ,$$

where R_m is the melt radius that may be varying with time as well. From this we can see that if the crystal cross-sectional area is much smaller than the melt area, $A \ll A_m$ or $1 \ll R_m$, then the melt height decreases very slowly and the crystal growth rate is approximately the same as the pull rate.

The Stefan condition now becomes

$$1 + \frac{\rho_x}{\rho_m R_m^2} = S^{-1}\frac{\partial \chi}{\partial z} - q_m \ . \tag{2.13}$$

This provides a relation between the pull rate and the heat fluxes at the interface. We take q_m as an input from a separate (uncoupled) numerical calculation and $\frac{\partial \chi}{\partial z}$ from equation (2.12). If we write (2.13) in dimensional form we find

$$\rho_x L_f \hat{v}\left(1 + \frac{\rho \hat{a}^2}{\rho_m \hat{R}_m^2}\right) = \frac{k_x \Delta \hat{T}}{\gamma \hat{L}_x}\tanh\left(\frac{\hat{b}}{\hat{L}_x \gamma}\right) - \hat{Q}_m \ . \tag{2.14}$$

Rearranging equation (2.14) provides the optimal pull rate $\hat{v}_{opt}$ based on balancing the heat flow at the crystal/melt interface

$$\hat{v}_{opt} = \frac{\frac{k_x \Delta \hat{T}}{\gamma \hat{L}_x}\tanh\left(\frac{\hat{b}}{\hat{L}_x \gamma}\right) - \hat{Q}_m}{\rho_x L_f\left(1 + \frac{\rho_x \hat{a}^2}{\rho_m \hat{R}_m^2}\right)} \ , \tag{2.15}$$

which can be used to solve for the melt heat flux $\hat{Q}_m$ if the pull rate is specified. Notice all of the input parameters are constant, except for the crystal height ($\hat{b}$) and possibly the melt radius ($\hat{R}_m$). This means the optimal pull rate can be determined for any time in the crystal growing process.

In the limit of large x ($\tanh(x) \to 1$), we can state that the maximum heat flux at the melt interface occurs at large crystal lengths

$$k_x \lim_{b\to\infty} \left.\frac{\partial \hat{\chi}}{\partial \hat{z}}\right|_{z=b} = \frac{k_x \Delta \hat{T}}{\hat{L}_x} \lim_{b\to\infty} \frac{1}{\gamma}\tanh\left(\frac{\hat{b}}{\hat{L}_x \gamma}\right) \to \frac{k_x \Delta \hat{T}}{\hat{L}_x \gamma} = \Delta \hat{T}\sqrt{\frac{2 H_{gs} k_x}{\hat{R}_x}} \ . \tag{2.16}$$

The final term in (2.16) shows that the heat flux in the crystal increases with increasing heat transfer coefficient, conductivity and temperature difference $\Delta \hat{T}$ whilst it decreases with crystal radius. This is inline with physical intuition. The faster heat flows (larger k_x) and is transferred out the sides to the ambient gas (high $\Delta \hat{T}, H_{gs}$), the more rapid solidification can occur. Since the melt is the heat source for the

crystal, larger radius crystals will require longer to solidify since there is more energy that has to be extracted into the surrounding gas.

Using (2.16) we can therefore write down an expression for the maximum pull rate ($\hat{v}_{max}$), in terms of the crystal parameters and the melt heat flux:

$$\hat{v}_{max} = \frac{\Delta\hat{T}\sqrt{\frac{2H_{gs}k_x}{\hat{R}_x}} - \hat{Q}_m}{\rho_x L_f \left(1 + \frac{\rho_x \hat{a}^2}{\rho_m \hat{R}_m^2}\right)} . \tag{2.17}$$

Alternatively, if we wish to specify a pull rate this expression allows us to determine a heating strategy. Realistically, the only way to change the pull rate for a given crystal size is to alter the temperature of the surrounding gas, $\hat{T}_g$, or to change the temperature profile in the melt.

2.3.2 Conical Crystals

When the crystal radius is changing with time then s is no longer a constant; assuming a linear variation we may write $s(z) = s_0 + mz$. Here, s_0 is the crystal radius where the linear profile commences and m is the slope. For the crystal shown in Figure 2.1, appropriate values are of the order $s_0 \sim 0.1$ and $m \sim 0.9$. Our leading order heat equation is now:

$$\gamma^2(s_0 + mz)\frac{\partial^2\chi}{\partial z^2} - \chi = 0 \qquad 0 \leq z \leq b . \tag{2.18}$$

An exact solution to this equation, subject to boundary conditions (2.11) may be written in terms of Bessel functions. However, computing this solution then requires the numerical evaluation of the zeroes of the functions and then the calculation of a series. Instead we opt for using an ODE solver that uses collocation. This method and other standard techniques for solving two-point boundary value problems are discussed in the work by Ascher *et al* [42].

To compare conical and cylindrical crystals, temperature maps and profiles for each geometry are shown in Figure 2.4. The maximum radius of the conical crystal is $a = 1$ and for the cylinder is $r = 1/\sqrt{3}$, so the crystal volumes are identical.

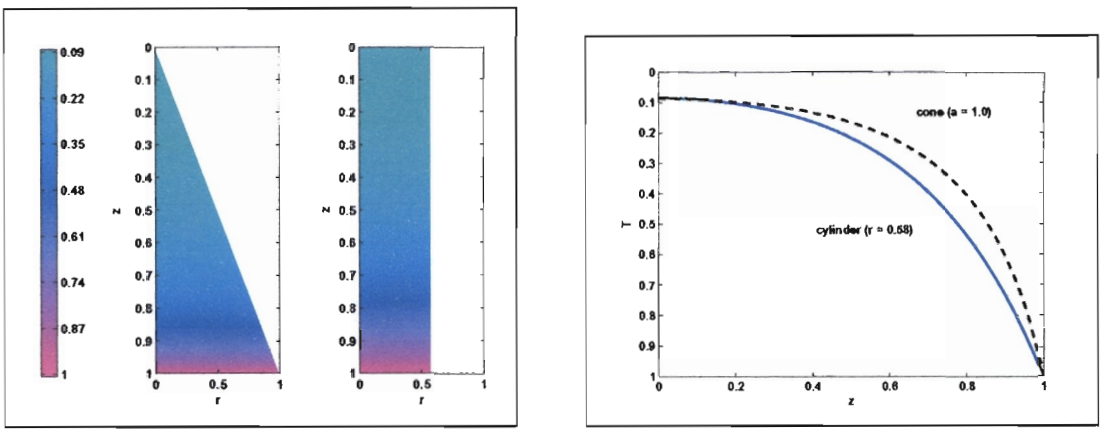

(a) Temperature map

(b) Temperature vs. vertical position

Figure 2.4: Temperature variation in differently shaped crystals

In order to show the distribution of the crystal temperature, the steady state profiles for the cylindrical and conical crystals are presented in Figure 2.4(b). As expected, the temperature gradient at $z = 1 = b$ is much for the cone since the surface area increases closer to the melt. The cylindrical crystal displays a slower decrease in temperature. Both profiles decay similarly after approximately halfway down either crystal.

For a conical crystal the rate of change of volume is

$$\frac{\partial V}{\partial t} = \frac{1}{3}\left(2ab\frac{\partial a}{\partial t} + a^2\frac{\partial b}{\partial t}\right) . \tag{2.19}$$

As before, the growth rate differs from the pull rate and, in this case, is given by

$$\frac{\partial b}{\partial t} = 1 + \frac{\rho_x a^2}{\rho_m R_m^2} . \tag{2.20}$$

Realizing $a = s_0 + mb$, the Stefan condition can be rearranged as an ODE for the radial growth rate, written as:

$$\frac{da}{dt} = \frac{ma}{2(a - s_0)}\left[3S^{-1}\left(\frac{\partial \chi}{\partial z} - q_m\right) - \left(1 + \frac{\rho a^2}{\rho_m R_m^2}\right)\right] . \tag{2.21}$$

The vertical growth rate can be written in terms of b and t only:

$$\frac{db}{dt} = 1 + \frac{\rho_x (s_0 + mb)^2}{\rho_m R_m^2} . \tag{2.22}$$

Equations (2.21) and (2.22) provide two ODEs for the two unknowns: the crystal radius (a) and the height (b).

2.3.3 Non-Standard Crystal Shapes in a Variable Temperature Gas

The method applied in the previous subsection could be also used for an arbitrary shaped crystal. One further useful addition is to allow the gas temperature to vary in the z direction as well. Applying boundary condition (2.7), results in a more general form of the first order heat equation:

$$\gamma^2 s(z)\frac{\partial^2 \chi}{\partial z^2} + (\chi_g(z) - \chi) = 0 \qquad 0 \leq z \leq b\,. \tag{2.23}$$

We can then solve numerically for χ via equation (2.23) now with $s = s(z)$ and $T_g \neq 0$, $T_g = \chi_g(z)$. This is solvable provided that at each time step the shape is relatively smooth (which will likely be true for sufficiently small times). Then equation (2.23) will provide the value for $\frac{\partial \chi}{\partial z}$ required in the subsequent Stefan condition. It should also be noted the addition of the variable gas temperature could also be performed in the other crystal heat equations (2.10) and (2.18), but was omitted for clarity.

2.4 Time Dependent Equations

An asymptotic solution was derived in the previous section by neglecting the time dependence in the crystal. The pseudo-steady assumption is a simplification, but to be useful must accurately approximate the solutions to the full heat equation (2.1). This section is devoted to validating this assumption by solving the time dependent system.

A fully implicit scheme was used for the temperature and an explicit scheme was used for the growth rates. A moving grid system is required since the domain is changing with time. The same substitutions were used to non-dimensionalize all variables, as in §2.2, but terms involving ϵ are no longer neglected.

2.4.1 Derivation

Since we are dealing with a moving boundary problem, the first step is to realize that the spatial variable is now also time dependent. Expressing this formally for the temperature means

$$\chi(x,t) \rightarrow \chi(x(t),t).$$

In terms of heat equation (2.1), the second order spatial derivative is unchanged but the time derivative needs to be replaced by the total derivative

$$\frac{D\chi}{Dt} = \left(\frac{\partial \chi}{\partial t} + \frac{\partial \chi}{\partial z}\frac{\partial z}{\partial t}\right). \tag{2.24}$$

The approach we are using is discussed by Crank [43] and used for multiple moving boundary problems by Gupta *et al* [44]. The governing equation for the moving boundary scheme in terms of partial derivatives can then be restated by adding the convective term to heat equation (2.9)

$$\epsilon\frac{\partial \chi}{\partial t} = \gamma^2\frac{\partial^2 \chi}{\partial z^2} - \frac{\chi}{s} + \epsilon\frac{\partial \chi}{\partial z}\frac{\partial z}{\partial t}\,. \tag{2.25}$$

To account for the changing crystal length, the temperature profile is calculated on a moving grid with a constant number of equally spaced points. Since the height of the crystal varies with time, the grid spacing of the mesh must be recalculated at each time step.

The points within the crystal are numbered from 0 at the melt interface and n at the seed chuck. Equation (2.25) can be integrated over a distance Δz and timestep Δt to obtain the finite difference scheme for the crystal. This is a common technique for deriving finite difference equations and is discussed in [45]. The resulting numerical scheme inside the crystal is then

$$\left(\frac{\gamma^2\Delta t}{\Delta z^2} + \frac{\epsilon\Delta t}{2\Delta z}\left.\frac{\partial z}{\partial t}\right|_{i+1/2} - \frac{\Delta t}{4s}\right)\chi_{i+1}^{k+1} - \left(\epsilon + \frac{2\gamma^2\Delta t}{\Delta z^2} + \frac{\Delta t}{2s}\right)\chi_i^{k+1} + \left(\frac{\gamma^2\Delta t}{\Delta z^2} - \frac{\epsilon\Delta t}{2\Delta z}\left.\frac{\partial z}{\partial t}\right|_{i-1/2} - \frac{\Delta t}{4s}\right)\chi_{i-1}^{k+1} = -\epsilon\chi_i^k\,. \tag{2.26}$$

The grid speed $\partial z/\partial t$ is calculated by using the vertical growth rate:

$$\left.\frac{\partial z}{\partial t}\right|_{i+1/2} = \frac{i+1/2}{n}\frac{db}{dt}, \tag{2.27}$$

where db/dt is given by equation (2.22). Note the grid moves at speed db/dt at the melt interface and is stationary at the seed chuck ($z = 0$). The grid spacing Δz^{k+1} now depends on the length of the crystal and must be updated every timestep using

$$\Delta z^{k+1} = \frac{b^k}{n} .$$

The remaining step is to apply boundary conditions (2.11) to the numerical scheme:

$$\left.\frac{\partial \chi}{\partial z}\right|_{z=0} = 0, \qquad \chi(b) = T_f = 1. \tag{2.28}$$

At the seed chuck ($z = 0$) , the no flux condition is applied by:

$$\left(\frac{2\gamma^2\Delta t}{\Delta z^2} + \frac{\epsilon\Delta t}{\Delta z}\left.\frac{\partial z}{\partial t}\right|_{i+1/2} - \frac{\Delta t}{4s}\right)\chi_1^{k+1} - \left(\epsilon + \frac{2\gamma^2\Delta t}{\Delta z^2} + \frac{3\Delta t}{4s}\right)\chi_0^{k+1} = -\epsilon\chi_0^k . \tag{2.29}$$

At the melt interface ($z = b$), the melting temperature is imposed by setting the n^{th} temperature to unity:

$$\chi_n^{k+1} = 1 . \tag{2.30}$$

Solving for the temperature at the $k+1$ timestep reduces then to inverting a single tri-diagonal matrix. The numerical solution in the crystal is given by constructing a tri-diagonal matrix using the order ($\chi_0..\chi_n$), with equations given by (2.26, 2.29, 2.30). The terms in these equations need to be updated at each time step as the mesh is continuously changing. Inverting this matrix completely solves for the temperature in the crystal.

The next step is to calculate the crystal height and radius. Using the conical approximation for the volume change of the crystal, the radial growth rate can be determined by the modified Stefan condition (2.21):

$$\left(\frac{da}{dt}\right)^{k+1} = \frac{ma^k}{2(a^k - s_0)}\left[3S^{-1}\left(\left[\frac{\partial\chi}{\partial z}\right]^{k+1} - q_m\right) - \left(1 + \frac{\rho_s(a^k)^2}{\rho_m R_m^2}\right)\right] . \tag{2.31}$$

The temperature derivative is now calculated numerically using the following three-point approximation:

$$\left[\frac{\partial \chi}{\partial z}\right]^{k+1} = \left(\frac{3\chi_1^{k+1} - 4\chi_2^{k+1} + \chi_3^{k+1}}{2\Delta z}\right). \tag{2.32}$$

The vertical crystal growth rate is calculated as in equation (2.22)

$$\left(\frac{db}{dt}\right)^{k+1} = 1 + \frac{\rho_x(s_0 + mb^k)^2}{\rho_m R_m^2}. \tag{2.33}$$

The melt radius can either be held constant since it varies little, or can vary by keeping track of the volume and height of the melt. In the calculations performed in this work the melt radius is constant for simplicity.

The last part of the algorithm requires updating the crystal radius and crystal height by:

$$a^{k+1} = a^k + \left(\frac{da}{dt}\right)^{k+1} \Delta t, \quad b^{k+1} = b^k + \left(\frac{db}{dt}\right)^{k+1} \Delta t. \tag{2.34}$$

This completes the numerical algorithm for one timestep. After Δt, the new temperature is recalculated by reconstructing and inverting the tri-diagonal matrix with equations (2.26, 2.29, 2.30). Subsequently, the next radial growth rate is determined by (2.31) and the vertical growth rate by (2.33). The new height and radius are then given by equation (2.34), which can be then used to reformulate the crystal temperature matrices and carry on the calculation at the next timestep. This process is repeated for the desired time interval and is summarized in Figure 2.5.

The initial conditions for the time dependent case are taken to model the actual physical process. In our opinion, the most realistic choice is a linear fit with $\chi(b) = 0$ at the melt, and $\chi(b) = 1$ at the seed chuck. This will lead to a slight discrepancy in the steady-state and the transient model, but is necessary. In the numerical calculations 40 mesh points were used in both the crystal and melt regions. In the results presented, 20000 timesteps were used. Doubling the number of mesh points and/or timesteps had a negligible effect on the solution (changed by less than 0.1 %).

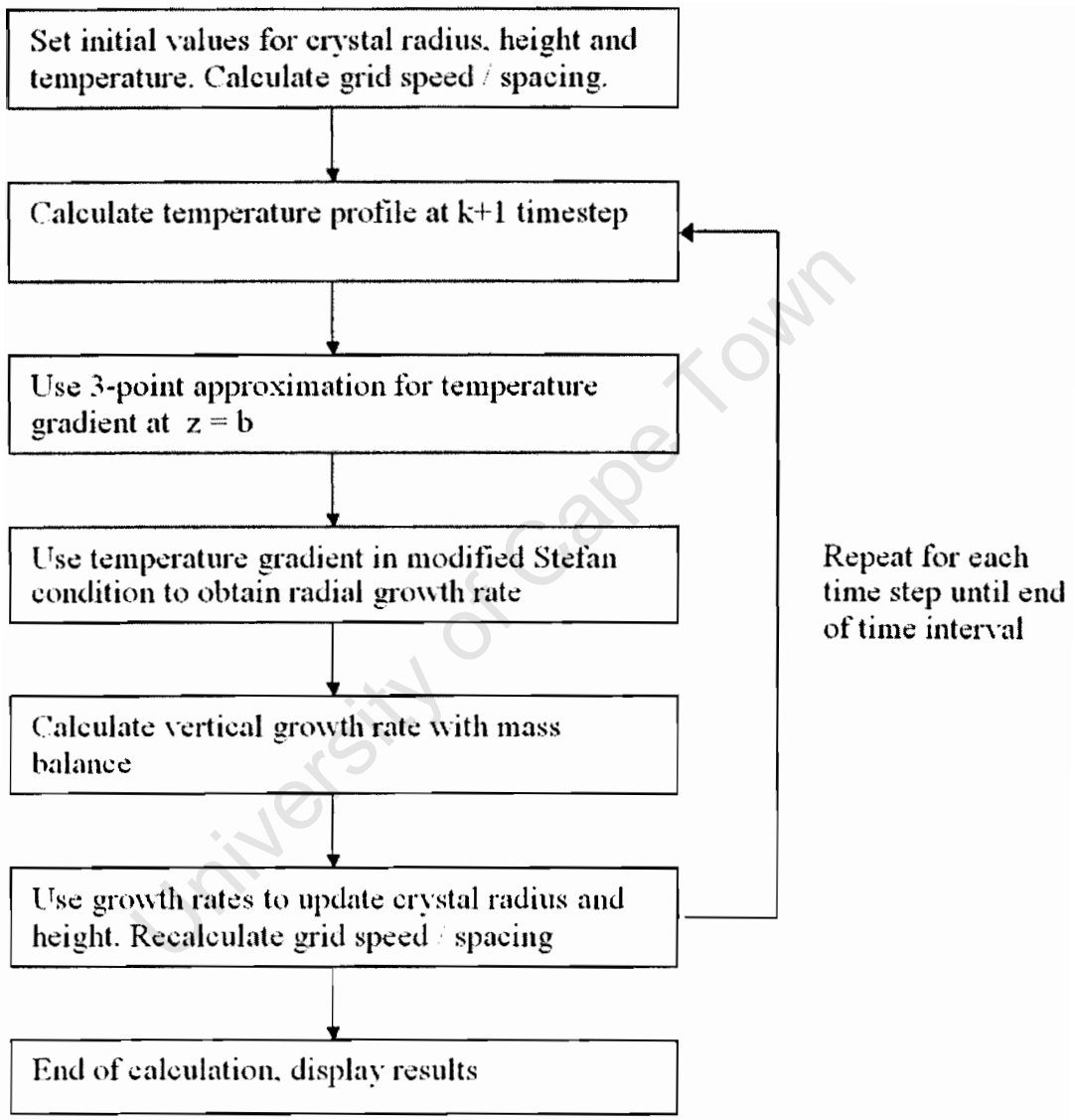

Figure 2.5: Summary of numerical time-dependent solution

2.5 Results

The main objective of this section is to show we can model the crystal thermal behaviour by solving only a second-order ODE for the temperature, and calculate the shape by using the temperature gradient in a modified Stefan condition. It should be emphasized that this is valid only under the conditions discussed in §2.2.1 to ensure that the time derivative can be neglected. We will increase the pull rate to show how large discrepancies arise if the quasi-steady model is improperly applied, and neglecting the time dependence is no longer appropriate.

The secondary objective is to apply the solidification model to investigate process parameters that are of interest to the industrial crystal grower. In the following results, we show the effect of melt recession and model a crystal in a variable temperature gas. The reason for these calculations is to enable the industrialist to determine how process parameters affect the crystal thermal profile and shape.

2.5.1 Model Validation

The purpose here is to examine the difference between the pseudo-steady and time dependent solutions. The following crystal simulations were run with the parameters given in table 2.2.

property	symbol	value
melt radius	R_m	2.0
time interval	t	1.0
initial crystal radius	a_0	0.10
initial crystal height	b_0	0.10
melt heat flux	q_m	1.0

Table 2.2: Non-dimensional simulation parameters

Figure 2.6 shows how the time dependent and time independent solution compare

throughout the growth period for appropriate pseudo-steady conditions ($\epsilon = 0.17$). Initially, there is a slight disagreement because the quasi-steady model is singular at $t = 0$, so the initial conditions can not be satisfied. The crystal temperature profile reaches steady-state conditions relatively quickly and the solutions show strong agreement. It should also be noted that the disagreement in the temperature field usually occurs at the seed chuck $z = 0$, not at the melt interface $z = b$, where the gradient is calculated for the Stefan condition.

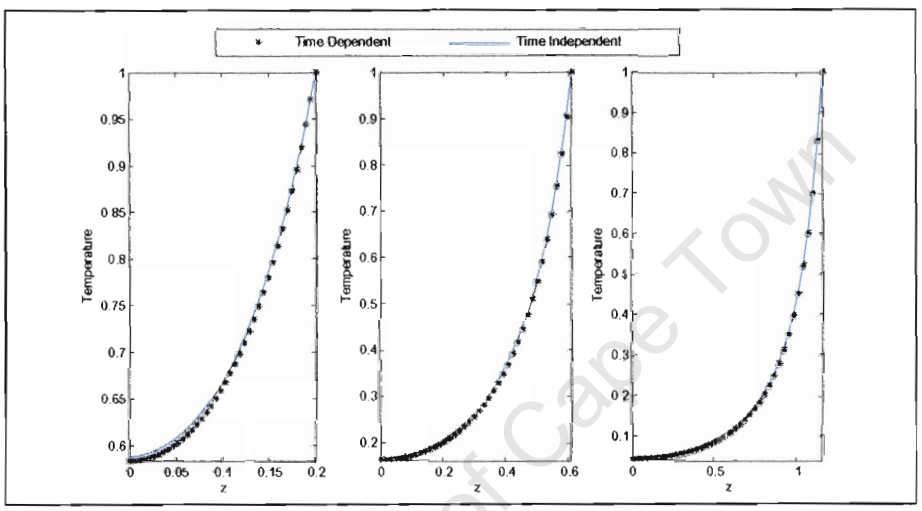

Figure 2.6: Results of 1D calculations at a) $t = 0.1$, b) $t = 0.5$, c) $t = 1.0$

Figure 2.7 compares the growth profiles under the same operating conditions, except the bottom series accounts for the melt recession as the crystal solidifies, and the top series omits this effect. This is equivalent to growing crystals in a small versus a relatively large crucible. As expected, the receding fluid causes the crystal to be longer and thinner. Figure 2.7 also shows that it is unnecessary to solve the full time dependent solution and the quasi-steady assumption is valid in this case, since the final radii are within 1% of each other.

Care must be taken because the quasi-steady assumption is not valid under all growing conditions, it requires $\epsilon \ll 1$. If this is not the case, transient effects can build up and lead to significant discrepancies in the calculation, as shown in Figure 2.8. In these calculations the crystal pull rate has been doubled to increase the value

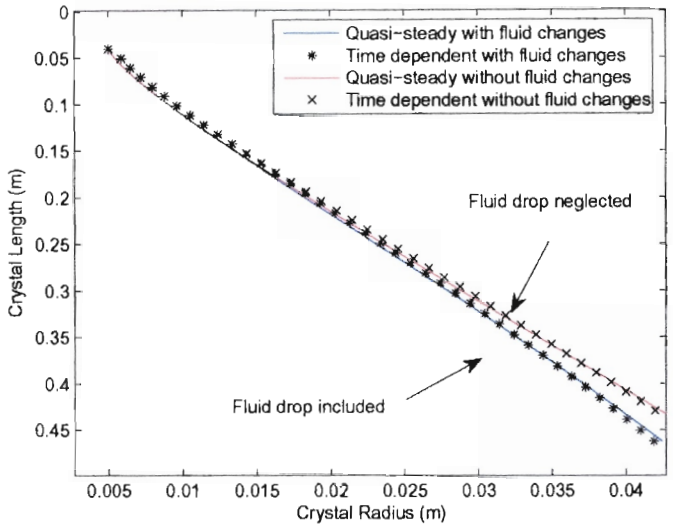

Figure 2.7: Solidification with melt recession

of ϵ to 0.34. It is our intention to illustrate the disagreement that occurs between the time-dependent and pseudo-steady profiles. In the first stages of crystal growth, we can clearly see the temperature profile is not approximated by the time independent solution. As the solution progresses, the temperature profiles become closer.

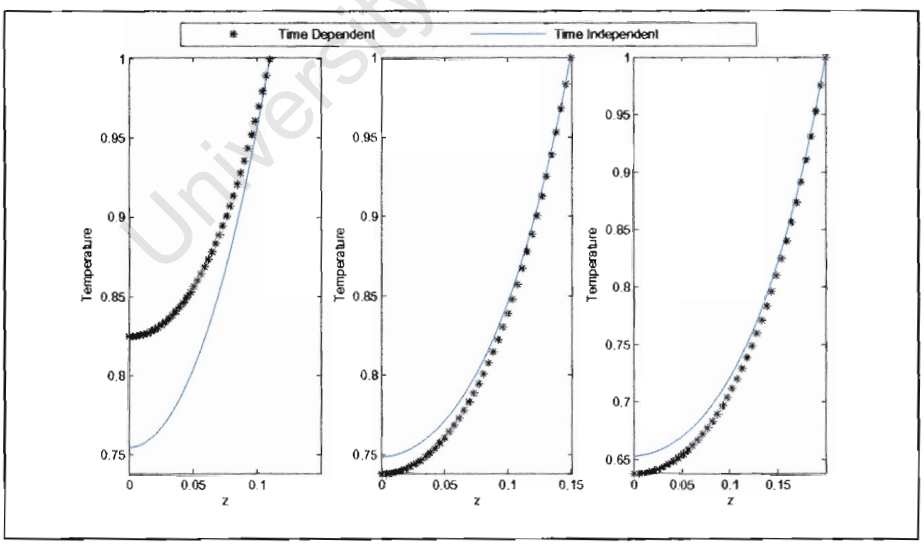

Figure 2.8: Results of 1D calculations at a) $t = 0.01$, b) $t = 0.05$, c) $t = 0.1$

The disagreement mainly occurs initially, within the first 5% of radial growth. Figure

2.9 shows the crystal profiles up to only $t = 0.5$ to illustrate this discrepancy. There appears to be two regions that form in the solution. The first is the initial time dependent stage that occurs at the very start of the process, when transient effects are still very significant and the length of the crystal is small. If ϵ is relatively large, the time required for the crystal temperature profile to reach steady-state becomes very significant and the model does not depict the shape accurately. The initial transient keeps the two profiles apart. It is also clear that past this initial transient the models agree much more closely and it is believed the steady analysis is once again valid. This means that the quasi-steady model can be used more reliably at later stages of crystal growth. In Figure 2.7, this initial transient is much smaller and does not significantly affect the crystal growth.

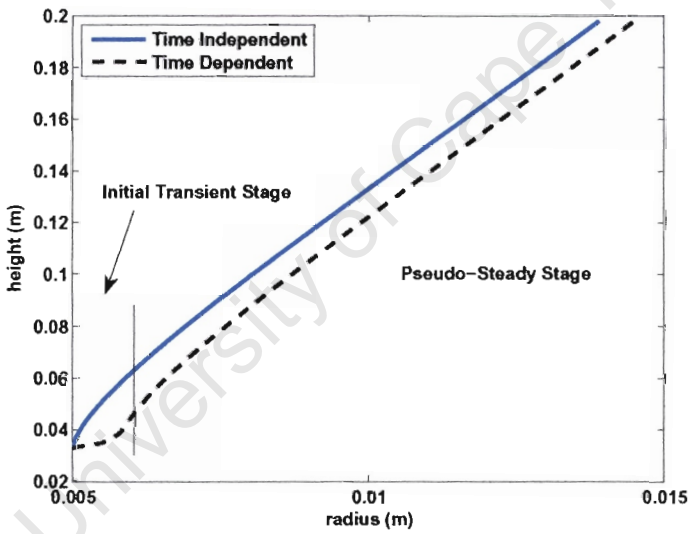

Figure 2.9: Time dependent crystal growth

2.5.2 Variable Gas Temperature

The final part of this work is to provide a practical application of the quasi-steady solidification model. In this example, we show the effect of a variable gas temperature on the crystal growth. The form we use for the gas temperature profile remains

at $\chi_g = 0$ at the melt interface, but decrease linearly away towards the seed chuck in the form

$$\chi_g(z) = T_g + \sigma(z - b), \tag{2.35}$$

where σ is a temperature factor that needs to be specified. For example, if $b = 1$ and $\sigma = 0.1$, then the temperature will vary from 0 at the melt to -0.1 at the seed chuck, in our case a 15 K variation. Figure 2.10 shows the original crystal shape for $\sigma = 0$ compared with variable gas temperatures for $\sigma = 0.05, 0.1$. The dotted series are the corresponding time-dependent solutions, the solid lines are the quasi-steady results. Clearly, these produce larger crystals since there is more heat being lost,

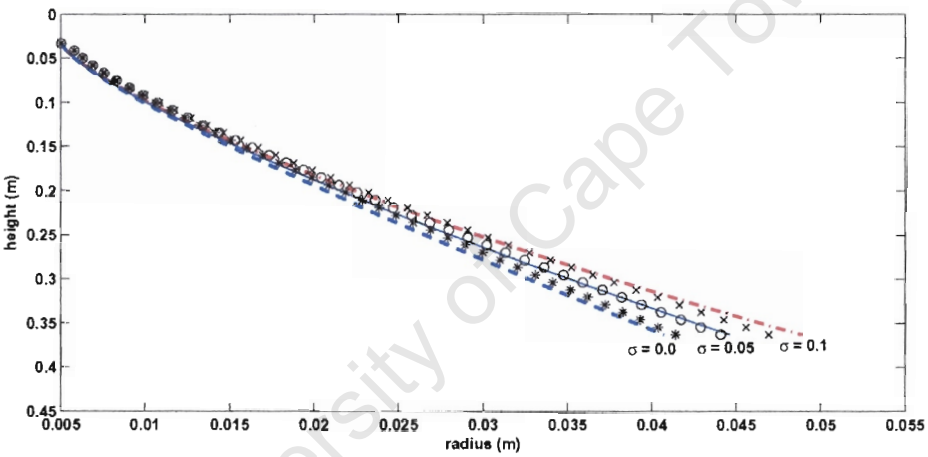

Figure 2.10: Crystal profiles with varying ambient gas temperatures

but note an accurate estimate of the change in the crystal shape can be determined. Using $\sigma = 0.1$ we obtain approximately a 5 cm increase in the crystal radius.

2.6 Summary

This Chapter consisted of developing a pseudo-steady model for the crystal solidification dynamics. The motivation for this asymptotic approach is to be able to couple the solidification model with a fluid dynamics calculation for the melt. We first made a 1D approximation, based on the work of other authors. Then we proceeded to analyze the resulting heat equation. Using the actual process values of InSb, it appeared reasonable to assume the time dependence could be neglected. It was shown that the quasi-steady assumption only holds for small values of ϵ, and needs to be verified for each case. Numerical results showed that the majority of the time-dependent behaviour occurs right at the beginning of the crystal growth process, when the length is small.

The Stefan condition was modified for cylindrical and conical geometry. The cylindrical geometry enabled the prediction of optimal and maximal pull rates via the quasi-steady simplification. The cylindrical geometry enables the calculation of the radial growth rate. There is currently no method in the literature that calculates the radial crystal growth rate in such a concise manner.

Now that a model has been developed for the crystal solidification, an examination of the melt fluid mechanics is now required.

Chapter 3

Melt Fluid Mechanics I: Governing Equations

In this chapter we examine the governing equations for the velocity and thermal field of a Czochralski melt. We will begin by non-dimensionalizing the full Navier-Stokes equations. The resulting form suggests the presence of a boundary layer near the solid boundaries. Subsequently, a scale analysis with boundary layer theory is used to determine the dominant forces in this system. The outcome of the scale analysis is the motivation for the asymptotic flow model, developed in Chapter 4.

3.1 Model Derivation

In order to obtain the velocity and temperature profiles of a Czochralski melt, we consider conservation of mass, momentum and energy. These relationships (in the field of fluid mechanics) are more commonly referred to as the Navier-Stokes equations (with energy). For the crucible geometry we will use three-dimensional cylindrical coordinates (r, θ, z). We will also assume the semiconductor melt is in-

compressible. The derivation of these equations can be found in any modern fluid mechanics textbook, for example see Batchelor [46]. In dimensional form, the incompressible Navier-Stokes equations are:

Continuity

$$\frac{\partial \hat{u}_r}{\partial \hat{r}} + \frac{\hat{u}_r}{\hat{r}} + \frac{1}{\hat{r}}\frac{\partial \hat{u}_\theta}{\partial \hat{\theta}} + \frac{\partial \hat{u}_z}{\partial \hat{z}} = 0 \tag{3.1}$$

Momentum (r, θ, z)

$$\rho\left(\frac{\partial \hat{u}_r}{\partial \hat{t}} + \hat{u}_r\frac{\partial \hat{u}_r}{\partial \hat{r}} + \frac{\hat{u}_\theta}{\hat{r}}\frac{\partial \hat{u}_r}{\partial \hat{\theta}} + \hat{u}_z\frac{\partial \hat{u}_r}{\partial \hat{z}} - \frac{\hat{u}_\theta^2}{\hat{r}}\right) = -\frac{\partial \hat{P}}{\partial \hat{r}} + \mu\left(\hat{\nabla}^2\hat{u}_r - \frac{\hat{u}_r}{\hat{r}^2} - \frac{2}{\hat{r}^2}\frac{\partial \hat{u}_\theta}{\partial \hat{\theta}}\right) - \hat{F}_r \tag{3.2}$$

$$\rho\left(\frac{\partial \hat{u}_\theta}{\partial \hat{t}} + \hat{u}_r\frac{\partial \hat{u}_\theta}{\partial \hat{r}} + \frac{\hat{u}_\theta}{\hat{r}}\frac{\partial \hat{u}_\theta}{\partial \hat{\theta}} + \hat{u}_z\frac{\partial \hat{u}_\theta}{\partial \hat{z}} + \frac{\hat{u}_r\hat{u}_\theta}{\hat{r}}\right) = -\frac{\partial \hat{P}}{\partial \hat{\theta}} + \mu\left(\hat{\nabla}^2\hat{u}_\theta - \frac{\hat{u}_\theta}{\hat{r}^2} - \frac{2}{\hat{r}^2}\frac{\partial \hat{u}_r}{\partial \hat{\theta}}\right) - \hat{F}_\theta \tag{3.3}$$

$$\rho\left(\frac{\partial \hat{u}_z}{\partial \hat{t}} + \hat{u}_r\frac{\partial \hat{u}_z}{\partial \hat{r}} + \frac{\hat{u}_\theta}{\hat{r}}\frac{\partial \hat{u}_z}{\partial \hat{\theta}} + \hat{u}_z\frac{\partial \hat{u}_z}{\partial \hat{z}}\right) = -\frac{\partial \hat{P}}{\partial \hat{z}} + \mu\hat{\nabla}^2\hat{u}_z + \hat{F}_z \tag{3.4}$$

Energy

$$\rho c_l\left(\frac{\partial \hat{T}}{\partial \hat{t}} + \hat{u}_r\frac{\partial \hat{T}}{\partial \hat{r}} + \frac{\hat{u}_\theta}{\hat{r}}\frac{\partial \hat{T}}{\partial \hat{\theta}} + \hat{u}_z\frac{\partial \hat{T}}{\partial \hat{z}}\right) = k_l\hat{\nabla}^2\hat{T}. \tag{3.5}$$

where the dimensional Laplacian is:

$$\hat{\nabla}^2 = \frac{\partial^2}{\partial \hat{r}^2} + \frac{1}{\hat{r}}\frac{\partial}{\partial \hat{r}} + \frac{1}{\hat{r}^2}\frac{\partial^2}{\partial \hat{\theta}^2} + \frac{\partial^2}{\partial \hat{z}^2} \tag{3.6}$$

There will be no body forces in the radial and azimuthal direction ($\hat{F}_r = \hat{F}_\theta = 0$). The rotation will be accounted for in the boundary conditions. A z body force term is present due to the weight of the fluid ($\hat{F}_z = \rho g$). For convective flows, it is convenient to assume the fluid density only varies with temperature in the z body force, and then linearize the density at an appropriate value. In this case, we use

the reference density ρ_0 at the melt freezing temperature ($\hat{T}_f$). This simplification is commonly known as the Boussinesq approximation for the density and can be written as:

$$\rho = \rho_0(1 - \beta(\hat{T} - \hat{T}_f)), \qquad \beta = -\frac{1}{\rho_0}\frac{\partial\rho(\hat{T}_f)}{\partial\hat{T}}. \tag{3.7}$$

Before proceeding it is necessary to discuss the steady-state and axisymmetric assumptions we will make to system (3.1)-(3.5) to simplify our analysis.

3.1.1 Axisymmetry

One of the assumptions in this work is that the crucible flow is axisymmetric in the azimuthal direction. This is done primarily for convenience but also because there is no strong evidence for large anti-symmetry in laminar melt flows. For example, simulations by Givoli *et al* [47] for lower Grashof numbers Gr = 10^5 show flow fields that are highly axisymmmetric. Even for turbulent Si flows, non-symmetric calculations, such as [20, 48], show small variations in the θ direction. Furthermore, there are a number of authors who use the axisymmetric assumption for detailed melt calculations, as in the global model of Li *et al* [49]. It is for these reasons we will make use of the axisymmetric assumption and set all derivatives with respect to theta equal to zero.

3.1.2 Time Independence

The other fundamental assumption we make is to neglect the time dependence in the melt, based on physical reasoning. The crystal pull rate is approximately 5×10^{-6} m/s, compared to the typical rotational velocity at the crucible wall (5 RPM $\sim$ 0.05 m/s), which is larger by four orders of magnitude. Since the crystal is being pulled at such a slow rate, the changes in the flow field will occur on a much shorter time scale than in the crystal. In addition, all of the boundary conditions for the melt vary on the same time scale as the crystal pull rate.

There have been many steady-state flow calculations, such as the early work by Kobayashi [18] and by Givoli *et al* [47]. Recent work on time dependent flows deals primarily with calculating small oscillations or fluctuations that occur in the flow field, such as in [25, 50]. For this thesis, we are interested in the dominant flow behaviour, not slight oscillations, which is why a steady-state model for the flow and temperature is utilized.

3.2 Non-Dimensionalization of Equations

In order to analyze equations (3.1)-(3.5), it is necessary to non-dimensionalize them with the appropriate physical quantities. The typical variable values are taken from the crucible geometry and melt physical properties. The radial and vertical length scale chosen is the crucible radius ($\hat{R}_c$). The temperature scale is the difference between the crucible wall temperature ($\hat{T}_c$) and the melt freezing temperature ($\hat{T}_f$). The pressure is non-dimensionalized using the static and dynamic pressure; while the velocity scale ($\hat{U}$) is chosen to balance the buoyancy with the inertial terms in the z-momentum equation (3.4), as given below. These values are used for the following substitutions:

$$\underline{u} = \frac{\hat{\underline{u}}}{\hat{U}}, \qquad \omega = \frac{\hat{R}_c}{\hat{U}}\hat{\omega}, \qquad r = \frac{\hat{r}}{\hat{R}_c}, \qquad z = \frac{\hat{z}}{\hat{R}_c}, \tag{3.8}$$

$$T = \frac{\hat{T} - \hat{T}_f}{\Delta\hat{T}}, \qquad \Delta\hat{T} = \hat{T}_c - \hat{T}_f, \qquad P = \frac{\hat{P} - \hat{P}_{atm} + \rho_0 g(\hat{z} - \hat{R}_c)}{\rho_0 \hat{U}^2}, \tag{3.9}$$

where $\underline{\hat{u}} = \hat{u}(r, \theta, z)$ and the buoyant velocity scale is defined by

$$\hat{U} = (\hat{R}_c g \beta \Delta\hat{T})^{1/2}. \tag{3.10}$$

The value of the buoyant velocity using the parameters in Table 3.1 is ($\hat{U} \sim 0.03$ m/s), compared to the rotational velocity component at the crucible wall (5 RPM $\sim$ 0.05 m/s), which are the same order of magnitude. Using these approximate values it is clear that both the rotation and buoyancy are significant. Note it does

not matter which velocity is used to non-dimensionalize equations (3.1)-(3.5), but in order to model flow in the absence of rotation, a non-zero velocity must be used. Therefore, we use the buoyant velocity as given in (3.10).

At this point we proceed with the axisymmetric, steady form of the Navier-Stokes equations, where all derivatives with respect to θ and t are zero. The non-dimensional equations for conservation of mass, momentum and energy, in cylindrical coordinates can then be written as:

Continuity

$$\frac{\partial u_r}{\partial r} + \frac{u_r}{r} + \frac{\partial u_z}{\partial z} = 0 \tag{3.11}$$

Momentum (r, θ, z)

$$u_r \frac{\partial u_r}{\partial r} + u_z \frac{\partial u_r}{\partial z} - \frac{u_\theta^2}{r} = -\frac{\partial P}{\partial r} + \frac{\mathrm{Pr}}{\mathrm{Bo}^{1/2}} \left(\frac{\partial^2 u_r}{\partial r^2} + \frac{1}{r}\frac{\partial u_r}{\partial r} - \frac{u_r}{r^2} + \frac{\partial^2 u_r}{\partial z^2} \right) \tag{3.12}$$

$$u_r \frac{\partial u_\theta}{\partial r} + u_z \frac{\partial u_\theta}{\partial z} + \frac{u_r u_\theta}{r} = \frac{\mathrm{Pr}}{\mathrm{Bo}^{1/2}} \left(\frac{\partial^2 u_\theta}{\partial r^2} + \frac{1}{r}\frac{\partial u_\theta}{\partial r} - \frac{u_\theta}{r^2} + \frac{\partial^2 u_\theta}{\partial z^2} \right) \tag{3.13}$$

$$u_r \frac{\partial u_z}{\partial r} + u_z \frac{\partial u_z}{\partial z} = -\frac{\partial P}{\partial z} + \frac{\mathrm{Pr}}{\mathrm{Bo}^{1/2}} \left(\frac{\partial^2 u_z}{\partial r^2} + \frac{1}{r}\frac{\partial u_z}{\partial r} + \frac{\partial^2 u_z}{\partial z^2} \right) + T \tag{3.14}$$

Energy

$$u_r \frac{\partial T}{\partial r} + u_z \frac{\partial T}{\partial z} = \frac{1}{\mathrm{Bo}^{1/2}} \left(\frac{\partial^2 T}{\partial r^2} + \frac{1}{r}\frac{\partial T}{\partial r} + \frac{\partial^2 T}{\partial z^2} \right) \tag{3.15}$$

and the Boussinesq number (Bo) and Prandtl number (Pr) are defined by

$$\mathrm{Bo} = \frac{\hat{R}_c^3 g \beta \Delta \hat{T}}{\alpha^2} \qquad \mathrm{Pr} = \frac{\nu}{\alpha}. \tag{3.16}$$

Notice we have reduced all the material properties and physical parameters to only two non-dimensional numbers: Bo and Pr, before including the boundary conditions. This system is the foundation of all the fluid mechanics analysis to follow.

3.3 Boundary Conditions

The boundary conditions to system (3.11)-(3.15) are shown in Figure 3.1. The physical set up can be summarized as follows. We are analyzing a heated crucible containing liquid InSb that is rotating at a rate $\hat{\omega}_c$. The crucible wall is assumed to be at a constant temperature ($T_c = 1$) and the no-slip condition is applied at this surface.

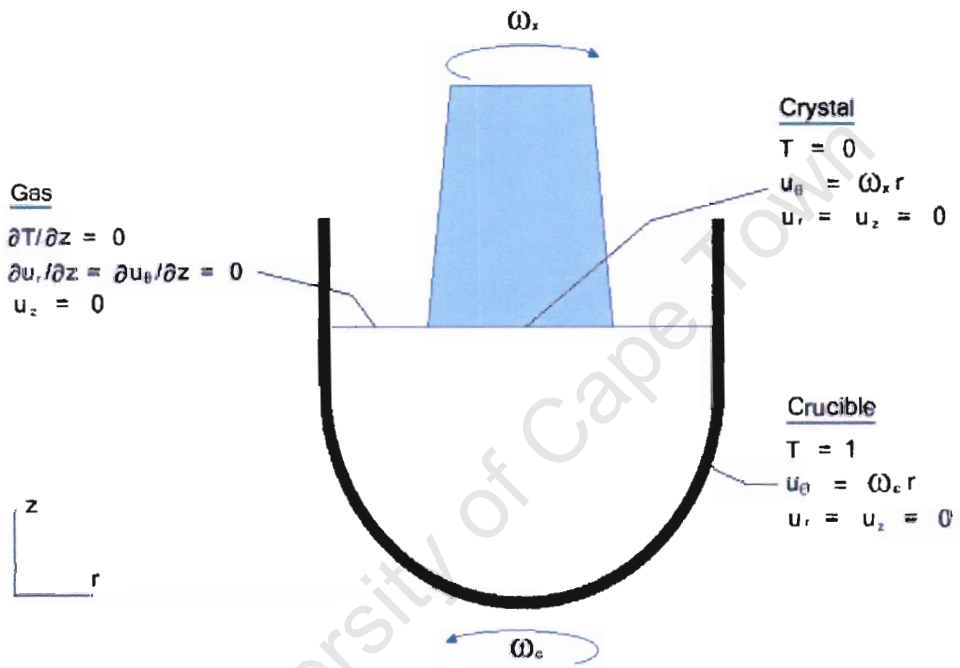

Figure 3.1: Boundary conditions for crucible flow

Above the melt, at the center of the flow is the crystal interface, which is rotating in the opposite direction to the crucible at a rate $\hat{\omega}_x$. The crystal must be at the freezing temperature of InSb ($T_f = 0$) and the no-slip condition is applied at the crystal face.

The final region is the free surface in contact with the surrounding gas. We assume the gas/melt interface is horizontal to avoid calculating the location of the free surface. In reality the meniscus will be curved where the fluid makes contact with the crystal and crucible. However, we assume this will have a small effect on the

melt dynamics. Since the heat exchange is low between the melt and the gas, no heat loss is assumed. Similarly, since the ambient gas will impose a very slight amount of shear, we neglect this effect and impose no-shear at this location.

This completes the mathematical description of the equations necessary to describe our model of the Czochralski melt system. We wish to examine these equations in more detail to be able to describe any possible structure of the flow field.

3.4 Scale Analysis

Using the data in Table 3.1, we obtain values for the critical parameters $\mathrm{Pr}/\mathrm{Bo}^{1/2} \sim 10^{-5}$ and $1/\mathrm{Bo}^{1/2} \sim 10^{-4}$. Since $\mathrm{Pr}/\mathrm{Bo}^{1/2} \ll 1$ and $1/\mathrm{Bo}^{1/2} \ll 1$, this suggests the viscous terms in equations (3.12)-(3.15) can be neglected. The problem with doing so is that the boundary conditions cannot be satisfied, indicating the presence of boundary layers. A scale analysis will be used to determine if this is indeed the case. We will first consider the crucible wall, and verify if a boundary layer is likely to form due to convection.

3.4.1 Crucible Wall

The scale analysis technique used in this section was developed by Bejan (for natural convection) and is discussed in his book [51] on convective heat transfer. The geometry is idealized as shown in Figure 3.2, which consists of an enclosure with a vertical wall at T_c, a cooler region at T_f, and the boundary layer region. This is by no means an exact analysis, we are only trying to estimate the force balance at the crucible wall and the size of the boundary region. This methodology first assumes the majority of the flow occurs in a slender region of thickness $\hat{\delta}$ and maximum height $\hat{R}_c$, near the vertical heated boundary (crucible wall). The value of $\hat{\delta}$ is unknown at this point but we assume it is much smaller than the crucible radius to make use of standard boundary layer assumptions to simplify our analysis.

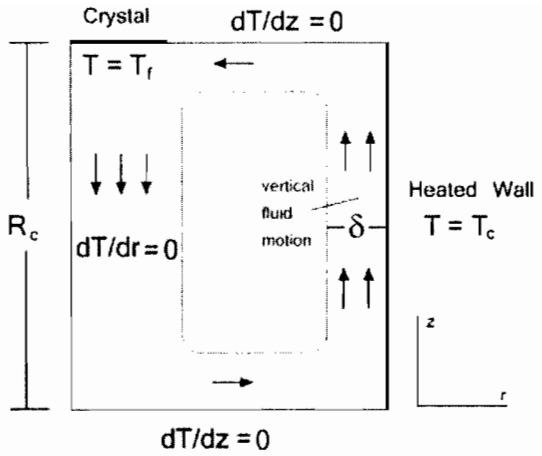

Figure 3.2: Schematic of crucible with idealizations for scale analysis

Assuming $\hat{\delta} \ll \hat{R}_c$ ensures that only the derivatives with respect to $\hat{r}$ remain from the $\hat{\nabla}^2$ operator in equations (3.12)-(3.15). An introductory text on fluid mechanics or boundary layer theory will provide the necessary background description, such as found in Chapter 8 by Acheson [52].

Once an estimate of the magnitude of $\hat{\delta}$ is obtained it can be compared to the crucible radius. If $\hat{\delta}$ is much smaller than the radius, then the majority of the flow occurs in a boundary layer at the crucible wall, otherwise if $\hat{\delta} \sim \hat{R}_c$ the initial assumptions are not valid and the majority of the flow is not confined to a slender region.

We proceed by using a typical velocity scale for $\hat{u}_r \sim \hat{U}$, $\hat{u}_z \sim \hat{V}$ that are unknown at this point. The temperature change will be approximated by the temperature difference between the crystal and crucible ($\Delta\hat{T}$). The characteristic length in the radial ($\hat{r}$) direction is of order $\hat{\delta}$ and the characteristic height in the axial ($\hat{z}$) direction is of order $\hat{R}_c$. Substituting these values into the dimensional form of energy equation (3.15) gives a balance between conduction and convection:

$$\underbrace{\frac{\hat{U}\Delta\hat{T}}{\hat{\delta}}, \frac{\hat{V}\Delta\hat{T}}{\hat{R}_c}}_{convection} \sim \underbrace{\frac{\alpha\Delta\hat{T}}{\hat{\delta}^2}}_{conduction} . \tag{3.17}$$

Substituting the same values corresponding to the slender region into the continuity

equation (3.11) reveals

$$\frac{\hat{U}}{\hat{\delta}} \sim \frac{\hat{V}}{\hat{R}_c}, \tag{3.18}$$

meaning both convection terms in (3.17) are of order $\hat{V}\Delta\hat{T}/\hat{R}_c$. Thus, we can restate the energy balance as

$$\frac{\hat{V}\Delta\hat{T}}{\hat{R}_c} \sim \frac{\alpha\Delta\hat{T}}{\hat{\delta}^2}. \tag{3.19}$$

Solving for $\hat{V}$ yields an estimate for the vertical velocity

$$\hat{V} = \frac{\alpha\hat{R}_c}{\hat{\delta}^2}, \tag{3.20}$$

in terms of the unknown width $\hat{\delta}$. Next, we turn our attention to the dimensional form of the z momentum equation (3.14). As mentioned earlier, the boundary layer assumption reduces $\hat{\nabla}^2$ to $\partial^2/\partial\hat{r}^2$, due to the fact this is only an order of magnitude estimate at the cylinder wall. As a further simplification we only consider the static pressure, $P = \rho_0 g(\hat{z} - \hat{R}_c)$, leaving

$$\hat{u}_r\frac{\partial\hat{u}_z}{\partial\hat{r}} + \hat{u}_z\frac{\partial\hat{u}_z}{\partial\hat{z}} = \nu\frac{\partial^2\hat{u}_z}{\partial\hat{r}^2} + g\beta(\hat{T} - \hat{T}_f) \tag{3.21}$$

to provide an estimate of the vertical force balance. Again, we substitute the typical values for the boundary layer analysis into equation (3.21) to obtain the balance:

$$\underbrace{\frac{\hat{U}\hat{V}}{\hat{\delta}}, \frac{\hat{V}^2}{\hat{R}_c}}_{inertia}, \quad \underbrace{\frac{\hat{V}\nu}{\hat{\delta}^2}}_{friction}, \quad \underbrace{g\beta\Delta\hat{T}}_{buoyancy}. \tag{3.22}$$

Clearly there must be a balance among these 3 forces: inertia, friction and buoyancy. The buoyancy cannot be negligible because it is the main force driving the crucible flow. Using the continuity balance (3.18), we see that both of the inertial terms are of the order $\hat{V}^2/\hat{R}_c$. By substituting the vertical velocity (3.20) into balance (3.22) and dividing through by $g\beta\Delta\hat{T}$, we obtain

$$\underbrace{\left(\frac{\hat{R}_c}{\hat{\delta}}\right)^4 \mathrm{Bo}^{-1}}_{inertia}, \quad \underbrace{\left(\frac{\hat{R}_c}{\hat{\delta}}\right)^4 \mathrm{Bo}^{-1}\mathrm{Pr}}_{friction}, \quad \underbrace{1}_{buoyancy}, \tag{3.23}$$

Relationship (3.23) shows the overall balance of the different forces. The fluid property that sets the first two terms apart is the Prandtl number, which for InSb is approximately 0.055. Since the Prandtl $\ll 1$, we see that the inertial terms must balance the buoyancy in (3.23). Balancing inertia with buoyancy and solving for $\hat{\delta}$ provides an estimate of the boundary layer thickness

$$\hat{\delta}_T \sim \frac{\hat{R}_c}{\mathrm{Bo}^{1/4}}. \tag{3.24}$$

The length scale determined by (3.24) is termed the thermal boundary layer thickness (denoted by $\hat{\delta}_T$), since the flow in this region is governed by the heat transfer to the fluid adjacent to the wall. In this region the buoyancy is balanced with inertia, meaning fluid is heated and rises along the wall, and the viscous effects are insignificant. For our analysis this is important because it implies that the fluid outside of the boundary layer is isothermal and motionless.

To better understand the boundary layer structure we also consider the balance between the viscous friction and buoyancy. Balancing the appropriate terms in (3.23), we obtain the viscous boundary layer thickness $\hat{\delta}_v$:

$$\hat{\delta}_v \sim \mathrm{Pr}^{1/2}\hat{\delta}_T = \frac{\hat{R}_c \mathrm{Pr}^{1/2}}{\mathrm{Bo}^{1/4}}. \tag{3.25}$$

Relationship (3.25) shows the viscous boundary layer is smaller than the thermal boundary layer. The majority of the fluid motion therefore occurs in a layer of width $\hat{\delta}_T$. Using the values in Table 3.1, the boundary layer thickness is estimated to be approximately 0.5 cm, which is definitely small compared to the crucible radius.

As a result of the boundary layer analysis we can sketch the expected temperature and velocity profiles, shown in Figure 3.3. In low Prandtl number melts, the viscous effects are very small and the buoyancy dominates the transition region.

property	symbol	value	units
		properties of liquid InSb	
kinematic viscosity (μ/ρ_0)	ν	3.3×10^{-7}	m^2/s
thermal diffusivity ($k_l/\rho_0/c_l$)	α	6×10^{-6}	m^2/s
thermal expansion	β	1×10^{-4}	/K
		physical parameters	
crucible radius	$\hat{R}_c$	0.10	m
gravitational acceleration	g	9.81	m/s^2
freezing temperature	$\hat{T}_f$	798	K
crucible temperature	$\hat{T}_c$	808	K
crystal rotation rate	$\hat{\omega}_x$	-5.0	RPM
crucible rotation rate	$\hat{\omega}_c$	5.0	RPM

Table 3.1: Material properties of liquid InSb and physical parameter values

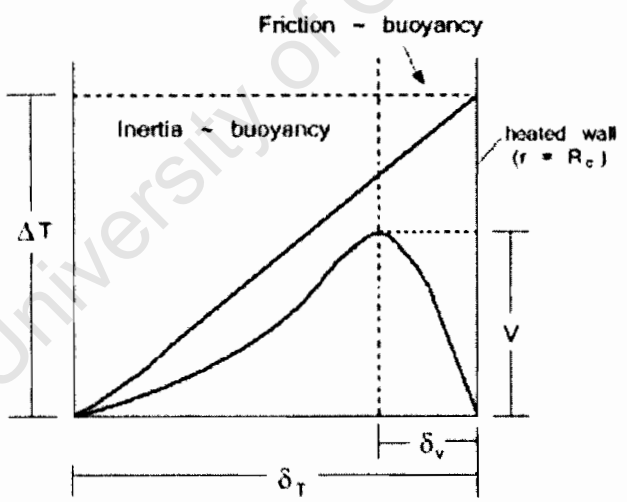

Figure 3.3: Comparison of thermal and viscous boundary layers (adapted from [51])

3.4.2 Crystal

The other location in the melt where the velocity field is likely to change quickly is near the crystal. Figure 3.4 shows the region underneath the crystal where we will perform another scale analysis to determine the dominating forces. The flow near the crystal will now be governed by the rotational velocity component, not the buoyancy.

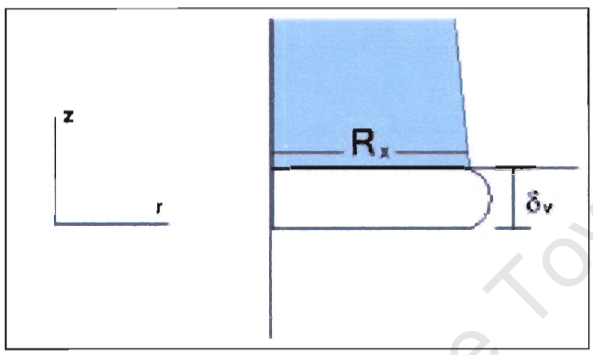

Figure 3.4: Schematic of region underneath crystal for scale analysis

The typical velocities will be $\hat{u}_r \sim \hat{U}$, $\hat{u}_z \sim \hat{V}$, $\hat{u}_\theta \sim \hat{W}$ that are unknown and are not the same as in §3.4.1. The radial length is scaled by $\hat{R}_x$ while the vertical length will be $\hat{\delta}_v$. The starting point will be to examine the dimensional form of the radial momentum equation (3.12) since the azimuthal velocity component appears in the inertial terms. We wish to estimate the relative magnitude of the azimuthal velocity compared to the radial velocity. Since the slender region is now horizontal, only the derivatives with respect to $\hat{z}$ remain from the $\hat{\nabla}^2$ operator. Momentum equation (3.12) becomes

$$\hat{u}_r \frac{\partial \hat{u}_r}{\partial \hat{r}} + \hat{u}_z \frac{\partial \hat{u}_r}{\partial \hat{z}} - \frac{\hat{u}_\theta^2}{\hat{r}} = -\frac{\partial \hat{P}}{\partial \hat{r}} + \nu \frac{\partial^2 \hat{u}_r}{\partial \hat{z}^2}. \tag{3.26}$$

To estimate the pressure gradient we use the dynamic pressure with the radial velocity component $\hat{P} = \rho_0 \hat{u}_r^2$. Using this form of the pressure and substituting the length and velocity scales, the balance of the terms in the radial momentum

equation (3.12) becomes

$$\underbrace{\frac{\hat{U}^2}{\hat{R}_x}, \frac{\hat{U}\hat{V}}{\hat{\delta}_v}, \frac{\hat{W}^2}{\hat{R}_x}}_{inertia} \sim \underbrace{\frac{2\hat{U}^2}{\hat{R}_x}}_{pressure}, \underbrace{\frac{\nu\hat{U}}{\hat{\delta}_v^2}}_{friction}. \tag{3.27}$$

Since the crystal rotation will be driving the flow in this region, the azimuthal velocity term should be considered separately from the other inertial terms. We can use the continuity relation (3.18) to eliminate the vertical velocity and then by collecting terms of order $\hat{U}^2/\hat{R}_x$ we are left with

$$\underbrace{\frac{\hat{U}^2}{\hat{R}_x}}_{inertia/pressure}, \quad \underbrace{\frac{\hat{W}^2}{\hat{R}_x}}_{rotation} \sim \underbrace{\frac{\nu\hat{U}}{\hat{\delta}_v^2}}_{friction}. \tag{3.28}$$

The balance in (3.28) shows the three forces governing the flow underneath the crystal: inertia, rotation and friction. In order to obtain an estimate of the boundary layer thickness, we need to determine the magnitude of the radial velocity.

The next equation to consider is the dimensional form of azimuthal momentum equation (3.13), since we need to obtain the radial velocity from the azimuthal force balance. We substitute the typical velocity and length scales leaving

$$\frac{\hat{U}\hat{W}}{\hat{R}_x}, \frac{\hat{V}\hat{W}}{\hat{\delta}_v}, \frac{\hat{U}\hat{W}}{\hat{R}_x} \sim \frac{\nu\hat{W}}{\hat{\delta}_v^2}. \tag{3.29}$$

Using continuity relation (3.18) we eliminate the z velocity component and collect terms of order $\hat{U}\hat{W}/\hat{R}_x$. The remaining terms reveal a balance between inertia and friction

$$\underbrace{\frac{\hat{U}\hat{W}}{\hat{R}_x}}_{inertia} \sim \underbrace{\frac{\nu\hat{W}}{\hat{\delta}_v^2}}_{friction}. \tag{3.30}$$

Solving for the radial velocity gives

$$\hat{U} \sim \frac{\nu\hat{R}_x}{\hat{\delta}_v^{\,2}}. \tag{3.31}$$

Substituting (3.31) into the balance (3.28) leaves

$$\underbrace{\frac{\nu^2\hat{R}_x}{\hat{\delta}_v^4}}_{inertia}, \quad \underbrace{\frac{\hat{W}^2}{\hat{R}_x}}_{rotation} \sim \underbrace{\frac{\nu^2\hat{R}_x}{\hat{\delta}_v^4}}_{friction}. \tag{3.32}$$

Balance (3.32) implies the inertia and friction are the same order of magnitude in the slender region underneath the crystal. By collecting the terms of order $(\nu^2\hat{R}_x)/(\hat{\delta}_v^4)$ and solving for $\hat{\delta}_v$ gives

$$\hat{\delta_v} \sim \left(\frac{\nu\hat{R}_x}{\hat{W}}\right)^{1/2}, \tag{3.33}$$

an estimate for the viscous boundary layer thickness. If the azimuthal velocity were replaced with the crystal rotation rate multiplied by the radial distance ($\hat{W} = \hat{\omega}_x\hat{R}_x$), we see that the boundary layer thickness only depends on the crystal rotation rate and the viscosity:

$$\hat{\delta_v} \sim \left(\frac{\nu}{\hat{\omega}_x}\right)^{1/2}. \tag{3.34}$$

The next step is to determine the approximate thermal boundary layer thickness. If we consider a region underneath the crystal, now of height $\hat{\delta}_T$, and substitute the typical velocities into the dimensional form of heat equation (3.15) we obtain

$$\frac{\hat{U}\Delta\hat{T}}{\hat{R}_x}, \frac{\hat{V}\Delta\hat{T}}{\hat{\delta}_T} \sim \frac{\alpha\Delta\hat{T}}{\hat{\delta}_T^2}. \tag{3.35}$$

Continuity relation (3.18) can be used to show the convection and conduction terms are of similar order of magnitude. Collecting the convection terms which are both order $\hat{U}\Delta\hat{T}/\hat{R}_x$ results in

$$\frac{\hat{U}}{\hat{R}_x} \sim \frac{\alpha}{\hat{\delta}_T^2}. \tag{3.36}$$

The final step is to substitute the radial velocity scale (3.31) from the azimuthal velocity balance, resulting in

$$\hat{\delta}_T = \left(\frac{\alpha}{\nu}\right)^{1/2}\hat{\delta}_v = \mathrm{Pr}^{-1/2}\hat{\delta}_v, \tag{3.37}$$

which is the same result as in (3.25), for the crucible boundary layer.

3.5 Summary

The system of equations (3.11)-(3.15) are the foundation for the melt fluid mechanics analysis in this work. These equations provide a framework for investigating the fluid

flow by simplifying the process variables and material properties to only two non-dimensional terms, the Prandtl and Boussinesq numbers (excluding the boundary conditions).

Our scale analysis resulted in an estimate of a buoyant boundary layer at the crucible wall and a momentum layer at the crystal wall. It is believed that the majority of the melt motion occurs inside these regions. In both cases the thermal boundary layer depends on the Prandtl number. For $\mathrm{Pr} \ll 1$, the thermal boundary layer thickness is larger by a factor $\mathrm{Pr}^{-1/2}$, which is consistent with the description by Jeong [53].

In the following chapter we will make use of the results from our scale analysis and develop an asymptotic flow calculation with a core region surrounded by a buoyant boundary layer at the crucible wall, and a momentum boundary layer underneath the crystal.

Chapter 4

Melt Fluid Mechanics II: Coupled Boundary Layer Model

This chapter focuses on the derivation of an asymptotic model for the velocity and thermal field of a Czochralski melt, based on the scale analysis presented in §3.4. We will use this asymptotic model as a means to describe the fundamental flow structure of the melt. The main output values from the asymptotic analysis will be the heat flux to the crystal, the average temperature and average rotation of the melt. In addition, in Chapter 7 we will couple the solidification calculation from Chapter 2, with the calculated melt heat flux devised in this chapter, to allow the crystal growth model to be dependent on the melt conditions.

The asymptotic approximation becomes invaluable because the solutions will continue to be valid at even lower Prandtl or higher Boussinesq numbers. We expect that as the Prandtl number decreases or the Boussinesq number increases, the flow field will become unstable as it becomes transitional and eventually turbulent. The consequences for the numerical calculation are that the elliptical part of the Navier-Stokes equations becomes small and the non-linear terms dominate, which can lead

to bifurcations, or other types of numerical instabilities.

This analysis can also be used to model crystal growth with parameters that vary throughout the process. For example, time dependent rotation rates or crucible temperature profiles could be easily implemented.

4.1 Previous Work and Motivation

Czochralski melt flows are dominated by two forces: buoyancy and rotation. Davidson [54] showed the similarities between swirling and buoyant flows via their generation of vorticity at the solid boundaries. He used a similarity substitution and then a momentum integral analysis to determine some of the flow parameters that were either dominated by buoyancy or swirling effects. The limitation of this work for the Czochralski process is that it is not clear whether rotational effects or buoyancy are dominant. It is likely that both effects can be dominant at different stages of the growth process. At the beginning of the growth period, the flow will resemble solid body rotation since the crystal radius is very small, restricting heat flow and the effect of crystal counter-rotation. As the crystal becomes larger, more heat is transported by the melt, increasing the buoyancy. The crystal rotation will be dominant towards the end of the process since by then the crystal area is greater and the melt height has decreased significantly. Furthermore, it is believed there are different regions within the crucible where either rotation, buoyancy or a combination of these effects dominate the flow. Hence, it is crucial to consider the effects simultaneously and to identify the locations where either or both forces govern the melt dynamics.

Several attempts have been made to describe the flow field of a Czochralski melt analytically. The most notable works are by Wheeler [55] and Irizarry-Rivera [56], both incorporating von Karman's rotational symmetry [57] underneath the crystal. Wheeler did not adequately model the flow near the crucible wall, and Irizarry-Rivera uses a complicated network of cells for the core. Neither models were compared with experimental or numerical results. The work by Jeong *et al* [53] focused

mainly on the melt temperature field to predict the crystal melt interface shape. They were not attempting to model the melt fluid dynamics, and they assumed the melt flow field took either one of two possible flow patterns. No other calculations were found that attempt to fully describe a Czochralski melt analytically or semi-analytically.

The aim of this work is to propose a boundary layer model that encompasses the dominant fluid mechanics of a Czcohralski melt. Using the values in Table 3.1, the critical parameters $\mathrm{Pr/Bo}^{1/2} \sim 10^{-5}$ and $1/\mathrm{Bo}^{1/2} \sim 10^{-4}$, suggest the viscous terms in equations (3.11)-(3.15) can be neglected. Neglecting these terms is reasonable, except near solid boundaries, where the derivatives can be very large and the boundary conditions cannot be satisfied.

In order to proceed it is necessary to assume some type of structure for the melt flow field. The proposed model consists of a rotating core region, surrounded by a thermal boundary layer at the crucible wall, and a momentum boundary layer under the crystal, as shown in Figure 4.1.

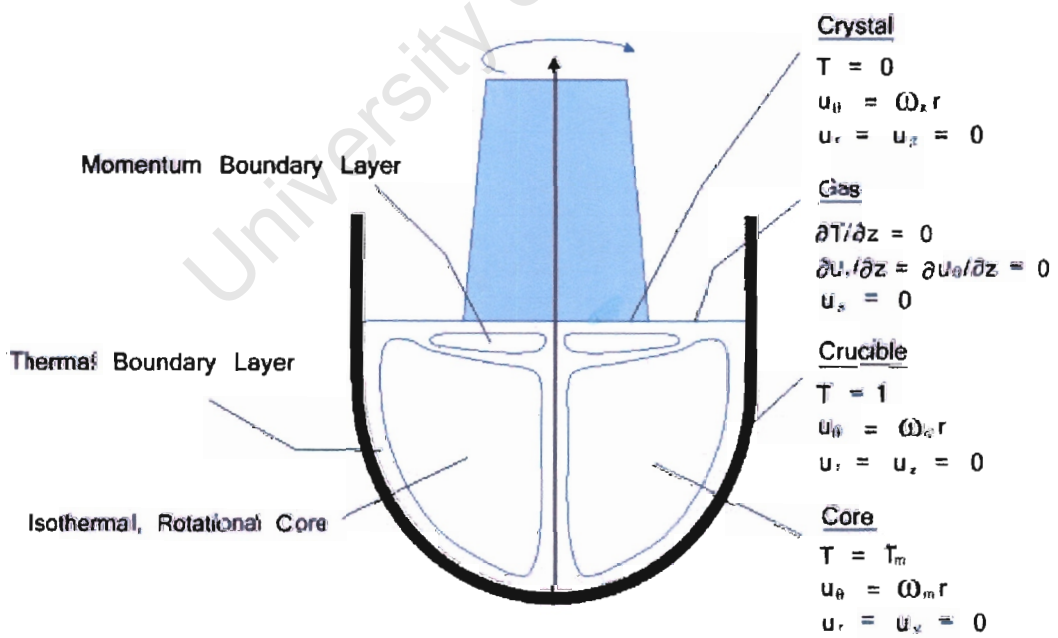

Figure 4.1: Schematic of coupled boundary layer flow regimes and boundary conditions

In §3.4.1 it was shown that the majority of buoyant fluid motion occurred in a thin region of thickness ($\hat{\delta}_T \sim \hat{R}_c/\mathrm{Bo}^{1/4}$) at the crucible wall. The mathematical approach we will use to model the flow field is a combination of the analysis by Kinnear and Davidson [58], and the similarity method by Lloyd and Sparrow [59] for forced convection over a flat plate. We will adapt the analysis for a curved surface and employ a similarity substitution to obtain a simplified form of the Navier-Stokes equations valid in the vicinity of the crucible wall.

Near the crystal, there is a rapid change in the flow field due to the counter rotation between the bulk of the melt and the crystal face. It was shown in §3.4.2 a viscous boundary layer is likely to be present underneath the crystal of width ($\hat{\delta}_v \sim \left(\frac{\nu}{\hat{\omega}_x}\right)^{1/2}$). For this reason, a momentum boundary layer is assumed directly underneath the crystal, with a velocity field described by the system developed by von Karman [57] for flow near a rotating disk. The flow underneath the crystal has already been described by the von Karman system by other authors such as Hurle [60].

The crucible and crystal boundary layers are then coupled together by a core region, with constant properties T_m and ω_m. All three of these regions are linked together to give a closed, consistent model of the Czochralski melt flow. It will also provide an idealized structure for comparison with a numerical solution that is presented in Chapter 6.

In the laminar simulations carried out by Givoli *et al*, no boundary layers are visible, presumably due to the fact that their simulations were carried out at low Grashof numbers ($\mathrm{Gr} = 5.6\times10^5$). At the opposite end of the scale, the direct-numerical simulations (DNS) by Wagner and Friedrich [48] using $\mathrm{Gr} = 2.0\times10^9$ showed temperature stratification at the crucible wall but it appears that turbulence has eliminated the possibility of an overall structure in the bulk of the melt.

We believe the InSb process is in a regime where a prominent boundary layer structure should form ($\mathrm{Gr} \sim 10^7$). Furthermore, the analysis by Davidson [54] and the work in §3.4 strongly suggest boundary layers are present. The numerical solution

in Chapter 5 becomes particularly useful to demonstrate if any of the assumed flow structure actually occurs.

4.2 Core Model

If the viscous terms are neglected in equations (3.11)-(3.15), the resulting system becomes

Continuity

$$\frac{\partial u_r}{\partial r} + \frac{u_r}{r} + \frac{\partial u_z}{\partial z} = 0 \tag{4.1}$$

Momentum (r, θ, z)

$$u_r \frac{\partial u_r}{\partial r} + u_z \frac{\partial u_r}{\partial z} - \frac{u_\theta^2}{r} = -\frac{\partial P}{\partial r} \tag{4.2}$$

$$u_r \frac{\partial u_\theta}{\partial r} + u_z \frac{\partial u_\theta}{\partial z} + \frac{u_r u_\theta}{r} = 0 \tag{4.3}$$

$$u_r \frac{\partial u_z}{\partial r} + u_z \frac{\partial u_z}{\partial z} = -\frac{\partial P}{\partial z} + T \tag{4.4}$$

Energy

$$u_r \frac{\partial T}{\partial r} + u_z \frac{\partial T}{\partial z} = 0. \tag{4.5}$$

We will assume that the majority of buoyant fluid motion occurs outside of this core region in the thermal boundary layer. If the buoyancy is negligible, this amounts to setting $u_z = 0$ and the temperature constant $T = T_m$ in the core region. The other assumption that we make is that the core is rotating at speed $u_\theta = \omega_m r$. Here, T_m and ω_m are the constant melt temperature and rotation rate respectively, which are unknown at this point. Substituting $u_z = 0$, into equation (4.3), makes u_r also zero. The only non-trivial equations remaining are (4.2) and (4.4), which reduce to

$$\frac{\partial P}{\partial r} = \omega_m^2 r, \qquad \frac{\partial P}{\partial z} = T_m. \tag{4.6}$$

The constants of integration for the pressure can be determined by the following conditions. The dynamic pressure must be zero at $r = 0$ and the static pressure must also be zero at $z = H$. Integrating equations in (4.6) then results in

$$P = \frac{\omega_m^2 r^2}{2} + T_m(z - H). \tag{4.7}$$

This gives a simplified core model that is consistent with the Navier-Stokes equations. The flow in this region can be summarized as isothermal with constant rotation: $u_r = u_z = 0$, $u_\theta = \omega_m r$ and $T = T_m$. It is now necessary to derive solutions that are valid near the boundaries: the crucible wall and the crystal.

4.3 Crucible Boundary Layer

The next step is to examine the flow at the crucible wall. The core flow is required to match the crucible conditions, which is accomplished via the introduction of a (non-dimensional) boundary layer of thickness $\delta_T = \hat{\delta}_T / \hat{R}_c$.

To consider both rotation and buoyancy, the following strategy has been implemented. We begin by assuming the presence of a convective boundary layer, that is a combination of free and forced convection. This is analogous to the work of Lloyd and Sparrow [59] for a flat plate, but we extend the methodology for a curved surface. By retaining the θ component of the Navier-Stokes equations we allow for a rotational component of motion that is coupled to the core layer.

We will make use of boundary layer theory to neglect derivatives parallel to the direction of the boundary layer. Before proceeding we require to change coordinate systems to express the differential equations in terms of directions normal and tangential to the crucible wall.

4.3.1 Coordinate Transformation

To simplify the analysis of the flow adjacent to the crucible wall it is necessary to change from cylindrical coordinates (r, θ, z) to a coordinate system that is normal and tangential to the surface (n, θ, s), as shown in Figure 4.2. Here, ϕ is defined as

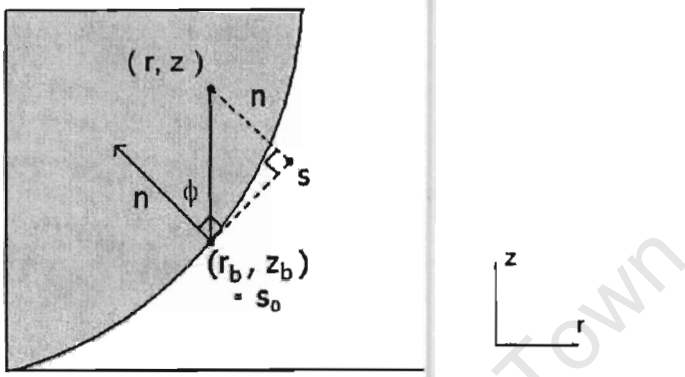

Figure 4.2: Schematic of crucible with coordinates normal and tangential to surface

the angle between the normal to the surface n and the z-axis, or, the angle between the tangential direction and the r-axis.

The tangential distance s, from the point s_0 on the crucible is defined by:

$$s - s_0 = (r - r_b)\cos\phi + (z - z_b)\sin\phi, \tag{4.8}$$

where r_b, z_b are points that lie on the crucible wall. The orthogonal distance n to any point in the melt, is defined in a similar way, but it must be scaled with the non-dimensional form of the thermal boundary layer thickness (3.24), $\delta_T = 1/\mathrm{Bo}^{1/4}$. The reason for rescaling the normal component is to apply the boundary layer assumptions whereby the region is slender. The normal distance is given by

$$n = \frac{-(r - r_b)\sin\phi + (z - z_b)\cos\phi}{\delta_T}. \tag{4.9}$$

We can now define (r, z) in terms of (n, s) and ϕ :

$$r = r_b - \delta_T n \sin\phi + (s - s_0)\cos\phi \tag{4.10}$$

$$z = z_b + \delta_T n \cos\phi + (s - s_0)\sin\phi. \tag{4.11}$$

The velocity components can also be rewritten in terms of the normal and tangential components:

$$u_r = -\delta_T \sin\phi u_n + \cos\phi u_s \tag{4.12}$$

$$u_z = \delta_T \cos\phi u_n + \sin\phi u_s. \tag{4.13}$$

By scaling the normal direction and velocity by the boundary layer thickness we are essentially applying the boundary layer assumptions ($\delta_T \ll 1$) in non-dimensional form. This allows us to neglect the second derivatives with respect to the tangential (s) direction from the Laplacian. By redefining the Navier-Stokes equations in the new coordinates (n, θ, s) and neglecting terms $\mathcal{O}(\delta_T)$, we obtain the following boundary layer equations for the crucible wall

Continuity

$$\frac{\partial u_n}{\partial n} + \frac{1}{r_b + (s - s_0)\cos\phi}\frac{\partial}{\partial s}\left(\left[r_b + (s - s_0)\cos\phi\right] u_s\right) = 0 \tag{4.14}$$

Momentum(n, θ, s)

$$-\frac{\partial P}{\partial n} = 0 \tag{4.15}$$

$$u_n\frac{\partial u_\theta}{\partial n} + u_s\frac{\partial u_\theta}{\partial s} + \frac{u_s u_\theta \cos\phi}{r_b + (s - s_0)\cos\phi} = \mathrm{Pr}\frac{\partial^2 u_\theta}{\partial n^2} \tag{4.16}$$

$$u_n\frac{\partial u_s}{\partial n} + u_s\frac{\partial u_s}{\partial s} - \frac{(u_\theta^2 - u_{\theta m}^2)\cos\phi}{r_b + (s - s_0)\cos\phi} = \mathrm{Pr}\frac{\partial^2 u_s}{\partial n^2} + (T - T_m)\sin\phi \tag{4.17}$$

Energy

$$u_n\frac{\partial T}{\partial n} + u_s\frac{\partial T}{\partial s} = \frac{\partial^2 T}{\partial n^2}. \tag{4.18}$$

Notice in the s-momentum balance (4.17), the pressure gradient $\partial P/\partial s$ was calculated using the core pressure expression (4.7) differentiated with respect to s and by changing the angular rotation into the azimuthal velocity component by $\omega_m r = u_{\theta m}$,

$$\frac{\partial P}{\partial s} = \frac{u_{\theta m}^2 \cos\phi}{r_b + (s - s_0)\cos\phi} + T_m \sin\phi.$$

The crucible boundary layer equations are now coupled to the melt rotation $u_{\theta m}$ in (4.17), thus linking the crucible flow to the core flow. It will also be linked to the core flow via the boundary conditions that are summarized below in the new variables (n, θ, s), where $n = 0$ corresponds to the crucible wall and $n = \infty$ represents the core region:

$$\begin{aligned} T(0,\theta,s) &= 1 & T(\infty,\theta,s) &= T_m \\ u_r(0,\theta,s) &= 0 & u_r(\infty,\theta,s) &= 0 \\ u_\theta(0,\theta,s) &= \omega_c r_b & u_\theta(\infty,\theta,s) &= u_{\theta m}. \\ u_z(0,\theta,s) &= 0 & u_z(\infty,\theta,s) &= 0 \end{aligned}$$

Although the boundary layer scaling has reduced the number of terms from (3.11)-(3.15), we can reduce the system further by making use of a similarity substitution.

4.3.2 Similarity Substitution

To solve boundary layer equations (4.14)-(4.18), we seek a similarity solution. This is essentially the same approach developed by Blasius [61] for fluids and Pohlhausen [62] for heat transfer. Lloyd and Sparrow [59] extended their work by using a similarity solution for mixed convection, over a flat vertical surface.

First, we reformulate equations (4.14)-(4.18) in terms of a stream function $\psi(n, s)$:

$$u_s = -\frac{1}{X}\frac{\partial \psi}{\partial n} \qquad u_n = \frac{1}{X}\frac{\partial \psi}{\partial s}, \tag{4.19}$$

where X denotes the transformed radial coordinate $X = r_b + (s - s_0)\cos\phi$. Note that the continuity equation is satisfied identically because the differential operators become:

$$\frac{\partial X}{\partial n} = 0 \qquad \frac{\partial X}{\partial s} = \cos\phi \qquad \frac{\partial}{\partial s}\left(\frac{1}{X}\right) = -\frac{\cos\phi}{X^2}.$$

We then transform equations (4.14)-(4.18) from (n, s) to the similarity variables (η, ξ). For a low-Pr number fluid the appropriate similarity variable is given by (see

[51] for details):

$$\eta = \frac{n}{s^{1/4}} \qquad \xi = s. \tag{4.20}$$

Then define $f(\eta)$ in terms of the stream function:

$$\psi = f(\eta)\ \xi^{3/4}. \tag{4.21}$$

As shown in Appendix A.1, these substitutions simplify our system to a set of 3 PDEs:

$$X\mathrm{Pr}\frac{\partial^3 f}{\partial \eta^3} - \frac{3}{4}\frac{\partial^2 f}{\partial \eta^2} f + (\frac{\partial f}{\partial \eta})^2 \left(\frac{1}{2} - \frac{\cos\phi\ \xi}{X}\right)$$

$$= X\cos\phi(u_\theta^2 - u_{\theta\infty}^2) + X^2 \sin\phi(T - T_m) \tag{4.22}$$

$$\frac{\partial^2 T}{\partial \eta^2} X = \frac{3}{4} f\ \frac{\partial T}{\partial \eta} - \xi \frac{\partial f}{\partial \eta}\frac{\partial T}{\partial \xi} \tag{4.23}$$

$$\frac{3}{4} f\ \frac{\partial u_\theta}{\partial \eta} - \xi \frac{\partial f}{\partial \eta}\left(\frac{\partial u_\theta}{\partial \xi} + \frac{\cos\phi\ u_\theta}{X}\right) = X\mathrm{Pr}\frac{\partial^2 u_\theta}{\partial \eta^2}. \tag{4.24}$$

The original system of five equations has been reduced to three, but it is desirable to make further simplifications to bring this model to a set of three non-linear ODEs that can be solved numerically relatively easily. The boundary conditions will be discussed at the end of this section.

4.3.3 Simplifications for Circular Geometry

It is convenient to make use of the spherical geometry and the constant temperature boundary condition to simplify the system further. In order to simplify the PDEs (4.22)-(4.24), it is convenient to make the following substitutions:

$$h = \frac{f(\eta)}{X}, \qquad T = T_m + (1 - T_m)\Theta. \tag{4.25}$$

Since the crucible is at a constant temperature, the temperature variation in the ξ-direction (along the crucible) will be zero, hence ($\Theta = \Theta(\eta)$). The transformed energy equation (4.23) then becomes

$$\Theta'' = \frac{3}{4} h\, \Theta'. \tag{4.26}$$

In this section the prime denotes differentiation with respect to η. The azimuthal velocity is specified in a form that eliminates the middle term in equation (4.24)

$$u_\theta = \frac{[\omega_m + \Delta\omega_c g(\eta)] r_b^2}{X}, \tag{4.27}$$

where $\Delta\omega_c = (\omega_c - \omega_m)$ and $g(\eta)$ is an undetermined function with $g(0) = 1$ and $g(\infty) = 0$. Equation (4.27) also ensures the melt rotation at the wall ($\eta = 0$) is the crucible rotation ω_c, and at the far-field ($\eta = \infty$) the melt is rotating at the core rate ω_m.

To simplify the geometric specifications we set $\xi = s = s_0$, which constrains ξ to a single point on the crucible wall. The reason for doing so is because these equations will be reevaluated at several points along the crucible wall. This means that for a given location on the crucible wall, the terms r_b, z_b, ϕ now become constants.

The final form of the equations is obtained by noting a few features for circular geometry. The angle ϕ varies along a quarter circle $0 \leq \phi \leq \pi/2$. Since ξ is tangential coordinate along the crucible surface clearly, $\xi = \phi$. Then the crucible radius can be defined by $r_b = \sin\phi$. These substitutions give the final form of the similarity equations for spherical crucible geometry:

$$\begin{aligned} \mathrm{Pr} h''' - \frac{3}{4} h'' h + (h')^2 \left(\frac{1}{2} - \frac{\phi}{\tan\phi} \right) \\ = \frac{\sin(2\phi)}{2} (\Delta\omega_c^2 g^2 + 2\omega_m \Delta\omega_c g) + \sin\phi (1 - T_m)\Theta \end{aligned} \tag{4.28}$$

$$\Theta'' = \frac{3}{4} h\, \Theta' \tag{4.29}$$

$$\mathrm{Pr} g'' = \frac{3}{4} h g'. \tag{4.30}$$

At $\eta = 0$ we impose the crucible wall conditions and $\eta \to \infty$ the flow and temperature must match the core conditions. In terms of the new variables the boundary conditions for the crucible boundary layer are then

$$h(0) = h'(0) = 0 \qquad h'(\infty) = 0 \tag{4.31}$$

$$g(0) = 1 \qquad g(\infty) = 0 \tag{4.32}$$

$$\Theta(0) = 1 \qquad \Theta(\infty) = 0. \tag{4.33}$$

This system now consists of only 3 ODEs with the following parameters: $\mathrm{Pr}, \phi, \omega_m, T_m$. The Prandtl number is known from the fluid properties and ϕ is the location on the crucible where the functions are being evaluated. Only the parameters ω_m, T_m remain to be determined. To calculate these values we need to consider the momentum boundary layer under the crystal and then the model can be closed.

4.4 Crystal Boundary Layer

Since the crystal is counter rotating relative to the crucible and bulk of the melt, we assume the presence of a momentum boundary layer underneath the crystal. Figure 4.3 summarizes the geometry relevant to this analysis and shows the exaggerated boundary layer.

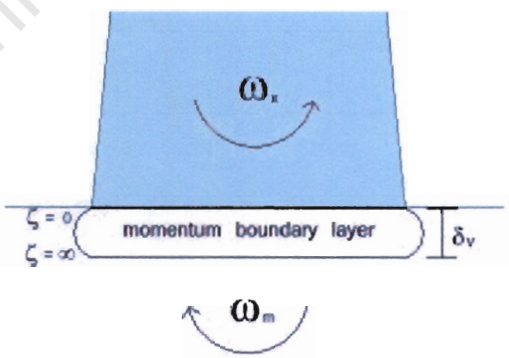

Figure 4.3: Schematic of momentum boundary layer underneath crystal

The analysis in this section is a combination of the work of von Karman [57] and

that of Rogers and Lance [63], but we extend it to include the effects of heating. Von Karman solved the problem of a rotating disk immersed in an infinite fluid by assuming azimuthal symmetry for the velocity components. Rogers and Lance extended this model to allow the fluid at infinity to be rotating as well. We wish to solve for the flow field between two counter-rotating heated disks, representing the core and crystal, which results in Ekman flow. However, a difficulty arises since it is necessary to specify the domain width or boundary layer thickness. Adapting the model by Rogers and Lance is possible but does not provide a unique finite boundary thickness, i.e. the system is solvable but the domain width then needs to be specified. We will make use of the approximate values from §3.4 to provide the appropriate boundary layer thicknesses.

4.4.1 Governing Equations for a Rotating Crystal

We proceed by using von Karman's model for a rotating disk that assumes a form such that $u_r/r, u_\theta/r$ and u_z are all functions of z only, to simplify equations (3.11)-(3.14). We extend this methodology by including energy equation (3.15) and impose the temperature field T also to be a function of z only.

The velocities are scaled by the difference in rotation $\Delta\omega_x = \omega_m - \omega_x$. The length scale is the non-dimensional form of the boundary layer thickness given in (3.34), which is the square root of the viscosity divided by the rate of rotation. The temperature is scaled with the core temperature since it is the maximum value. The rescaling of the dimensionless variables can be summarized as:

$$u_r = r\Delta\omega_x f(\zeta), \quad u_\theta = r\Delta\omega_x g(\zeta), \quad u_z = \left(\frac{\mathrm{Pr}}{\mathrm{Bo}^{1/2}}\Delta\omega_x\right)^{1/2} h(\zeta) \tag{4.34}$$

$$P = \left(\frac{\mathrm{Pr}}{\mathrm{Bo}^{1/2}}\Delta\omega_x\right) Q(\zeta), \quad T = (T_m)\,\Theta(\zeta), \tag{4.35}$$

with z transformed to the boundary layer coordinate ζ

$$z = H - \left(\frac{\mathrm{Pr}}{\mathrm{Bo}^{1/2}\Delta\omega_x}\right)^{1/2} \zeta. \tag{4.36}$$

Substituting these scaled quantities into our original system of equations (3.11)-(3.15) results in a system of ordinary differential equations that depend on ζ only:

Continuity

$$2f + h' = 0 \tag{4.37}$$

Momentum

$$f'' = f^2 - g^2 + hf' \tag{4.38}$$

$$g'' = 2fg + hg' \tag{4.39}$$

$$Q' = h'' - hh' - \left(\frac{T_m}{\Delta\omega_x^{3/2}}\frac{\mathrm{Pr}^{1/2}}{\mathrm{Bo}^{1/4}}\right)\Theta \tag{4.40}$$

Energy

$$\Theta'' = \mathrm{Pr}\Theta' h. \tag{4.41}$$

Since the velocity fields are now decoupled from the pressure, the crystal boundary layer equations have been reduced to a set of 4 non-linear ODEs (4.37)-(4.39) & (4.41). Notice in equation (4.40) the temperature has been scaled and appears in the pressure gradient in the z-direction. The result of this will be a large pressure gradient, but it does not affect the overall flow field. Since estimating the magnitude of the pressure or force at the crystal is beyond the scope of this work, equation (4.40) will not be considered. The continuity relationship (4.37) can used to eliminate f from equations (4.38) and (4.39) leaving the final form of the crystal boundary layer equations:

$$h''' = -\frac{1}{2}h'^2 + hh'' + 2g^2 \tag{4.42}$$

$$g'' = -gh' + g'h, \tag{4.43}$$

$$\Theta'' = \mathrm{Pr}\Theta' h. \tag{4.44}$$

At the crystal ($\zeta = 0$), the melt temperature is at freezing ($T_f = 0$) and the no-slip condition is applied. The crystal rotation is set to ω_x by choosing the appropriate value for g. The boundary conditions at the crystal are given by

$$h = h' = 0, \quad g = \frac{\omega_x}{\Delta\omega_x}, \quad \Theta = 0 \quad \text{at} \quad \zeta = 0. \tag{4.45}$$

Moving away from the crystal we approach the core $\zeta = \infty$, where the temperature becomes T_m and the rotation rate must approach ω_m. The other velocity components (u_r, u_z) decay to zero in the core region. The boundary conditions for the far-field condition are then

$$h' \to 0, \quad g \to \frac{\omega_m}{\Delta\omega_x}, \quad \Theta \to 1 \quad \text{as} \quad \zeta \to -\infty. \tag{4.46}$$

As mentioned earlier, a difficulty arises since the size of the domain is not known, and needs to be specified. To obtain the viscous boundary layer thickness we make use of the non-dimensional version of equation (3.34) obtained via the scale analysis performed in §3.4.2:

$$\delta_v = \left(\frac{\mathrm{Pr}}{\mathrm{Bo}^{1/2}\Delta\omega_x}\right)^{1/2}, \tag{4.47}$$

now in terms of the difference between the core and crystal rotation $\Delta\omega_x = \omega_m - \omega_x$, and the fluid parameters Pr, Bo. The length δ_v will be the domain that equations (4.42)-(4.44) are solved on to determine the azimuthal velocity gradient at the crystal.

Since the heat flux is crucial to the crystal growth dynamics, it is necessary to define the thermal boundary layer thickness δ_T. The scale analysis (3.25) revealed that the thermal boundary layer thickness is related to the viscous boundary layer thickness by rearranging (3.37):

$$\delta_T = \frac{\delta_v}{\mathrm{Pr}^{1/2}},$$

The idea for the crystal boundary layer is to use the fluid parameters and relative rotation rates to determine the momentum boundary layer, then obtain the thermal

boundary layer thickness. The length δ_T will be the domain that equations (4.42)-(4.44) are solved on to determine the temperature gradient at the crystal.

This completes the boundary layer description of the melt flow, although the parameters T_m and ω_m are still unknown. They are determined iteratively such that they satisfy conditions at the crucible and at the crystal, by coupling the entire system together.

4.5 Model Closure

In order to fully close the coupled boundary layer model, a few simple relationships are required. By conservation of energy, the amount of heat entering the crucible must flow out at the crystal (and to shielding gas if desired). Also, the amount of torque generated at the surface of the crystal must be balanced by the torque at the crucible wall.

The non-dimensional heat flow for the crystal and crucible are given by

$$Q_x = \int \frac{dT}{dz} dA_x \qquad Q_c = \int \frac{\partial T}{\partial n} dA_c. \tag{4.48}$$

Evaluating the crucible integral is not trivial since the temperature gradient changes along the surface and numerical integration is therefore required.

Similarly, the torque generated by the crystal and crucible are respectively

$$\tau_x = \int \frac{\partial u_\theta}{\partial z} r dA, \qquad \tau_c = \int \frac{\partial u_\theta}{\partial n} r dA. \tag{4.49}$$

Again, numerical integration is required for the angular velocity gradient at the surface of the crucible. The fluid height decreases with time so the integration along the crucible wall is performed only up to the appropriate fluid height, $s \in [0, s(H)]$.

These quantities obviously depend on the parameters T_m and ω_m, which need to be consistent with all three flow regimes (core, crucible boundary layer, crystal boundary layer). To start the calculation, T_m and ω_m are estimated to solve the coupled system and then iterated using an unconstrained non-linear optimization

scheme (eg. Nelder-Mead Simplex method [64]), until the heat and torque balance requirements are met.

The effects at the shielding gas are ignored in the following calculation in an effort to reduce the number of process variables we need to consider. The boundary conditions at the melt/gas interface are no-shear and no heat loss. Hence this interface does not participate in the coupled boundary layer model and may be neglected. It should be realized that these quantities could easily be added, but we have omitted them for simplicity.

Once the correct values are obtained for T_m and ω_m the model is capable of predicting heating and rotation rates for the melt flow throughout the crystal growth process.

4.6 Results

In this section we wish to show two main types of results for the coupled boundary layer model. The first set of plots will be results from the crucible and crystal boundary layer calculations individually, which will allow us to inspect the solutions of the boundary layer flow and thermal fields. The second set present all three regions coupled to obtain the heat flux to the crystal, T_m and ω_m, to show that the model is consistent using actual crystal growth data. Further validation is carried out in Chapter 6 by comparing the results with a Finite Element solution. However, for now we wish only to show that the coupled boundary layer model produces results that appear reasonable.

4.6.1 Crucible Boundary Layer Calculations

The system of ODEs (4.28)-(4.30) was solved using a commercial boundary value problem solver that uses collocation. Ascher *et al* [65] provide a description of this algorithm and other methods for solving boundary value problems. A relative tolerance was set to 10^{-4} and an absolute tolerance of 10^{-6}, with a starting mesh

size of 50 points.

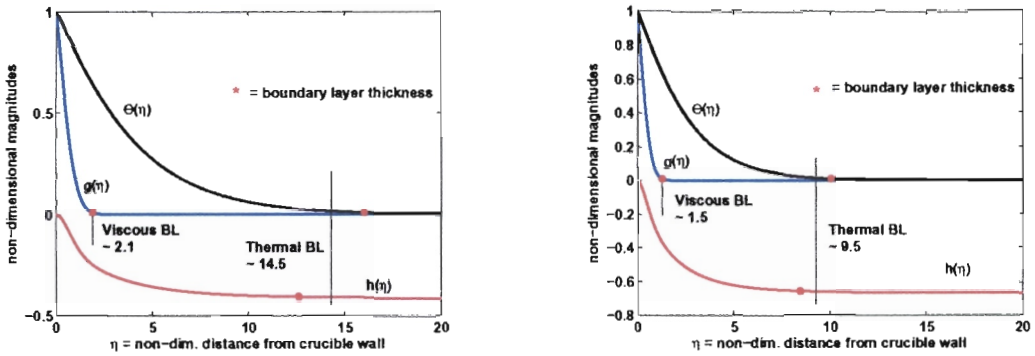

(a) $s = 0.1$ (b) $s = 0.9$

Figure 4.4: Crucible boundary layer profiles

The system of equations (4.28)-(4.30) are solved at a large value of $\eta = 20$, which overshoots the boundary layer thickness, as shown in Figures 4.4(a) & 4.4(b). The parameters used in this calculation are presented in Table 3.1. The parameter values for the core have been chosen as $T_m = 0.90$ and $\omega_m = 0.80$. The solution is plotted at two locations along the crucible $s = 0.1$ and 0.9 to show how the boundary layers vary along the crucible wall.

It may appear in Figure 4.4 that the boundary layer thickness at the bottom of the crucible ($s = 0.1$) is larger than that at the top ($s = 0.9$). This is not the case, recall the definition of η in equation (4.20). Rearranging this for the normal distance from the surface gives $n = \eta s^{1/4}$. The distances in terms of n then become, at $s = 0.1$: $\delta_v = 1.1, \delta_T = 8.1$ and at $s = 0.9$: $\delta_v = 1.5, \delta_T = 9.2$. As expected, in both cases, the thermal boundary layer thickness is approximately $\mathrm{Pr}^{-1/2} \sim 4.5$ times larger than the viscous boundary layer thickness as predicted in §3.4.

An interesting feature of this model occurs from examining equation (4.28), which involves the reduced stream function h, the crucible rotation ω_c, the core rotation ω_m and the temperature Θ. In particular we wish to emphasize the right hand side of (4.28):

$$\frac{\sin(2\phi)}{2}(\Delta\omega_c^2 g^2 + 2\omega_m \Delta\omega_c g) + \sin\phi(1 - T_m)\Theta.$$

The only term that can be negative is the core rotation ω_m (if the crystal rotation is sufficiently large). Notice the counter rotating effect will be maximum when $\sin(2\phi)$ is maximum at $\phi = \pi/4$, which corresponds to the midpoint on the crucible. This indicates that any change in flow will emanate from $\phi = \pi/4$ and will occur if there is sufficient counter rotation. A change in the flow field is not easily shown analytically but can occur in numerical calculations whereby h will actually change sign. This is an extremely important observation because the midpoint of the crucible is the most favourable location for the radial and axial velocities to change directions.

4.6.2 Crystal Boundary Layer Calculations

The boundary layer ODEs (4.37)-(4.39) & (4.41) have been solved with values of $T_m = 0.90$ and $\omega_m = 0.80$, shown in Figure 4.5.

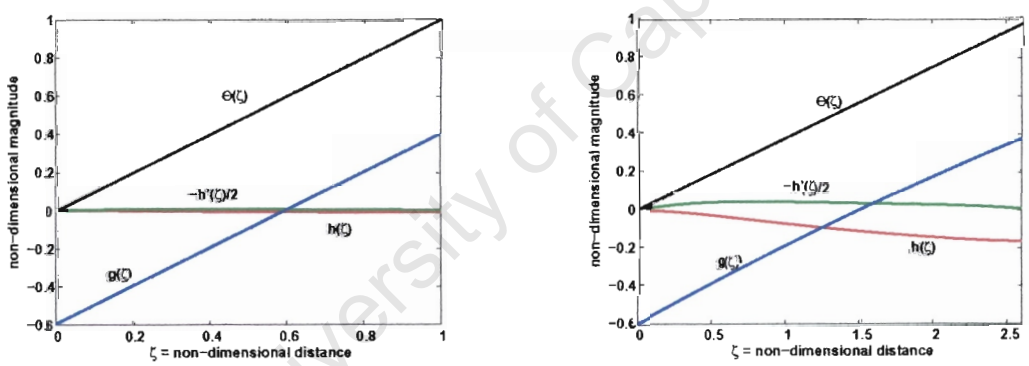

(a) $\zeta \in (0, 1)$ (b) $\zeta \in (0, 2.6)$

Figure 4.5: Crystal boundary layer profiles

The gradient for the azimuthal velocity can be calculated from Figure 4.5(a) and the temperature gradient can be calculated from Figure 4.5(b), to ensure the appropriate viscous or thermal boundary layer is used, respectively. The temperature profiles are not very interesting because the temperature gradient is strongly linear. There is little variation in the radial and axial velocity components in this case, which is also found in the numerical solutions presented in Chapter 6.

4.6.3 Coupled Model with Crystal Growth Profile

In order to use this model with ease it is convenient to create a database of the derivatives at the crucible wall and store them, rather than re-solve the ODEs (4.28)-(4.30) at each iteration. The system of equations for the crucible was therefore solved for different values of s, T_m and ω_m; with the gradients stored in a three-dimensional array. Then for actual grower calculations, the values are looked up and interpolated if necessary. This method dramatically increases the efficiency of the calculation.

In this section, we have re-scaled the variable ω such that $\omega_m = 0$ corresponds to the non-dimensional crystal rotation rate and $\omega_m = 1$ corresponds to the non-dimensional crucible rotation rate:

$$\omega_m = \frac{\omega_m - \omega_x}{\omega_c - \omega_x}. \tag{4.50}$$

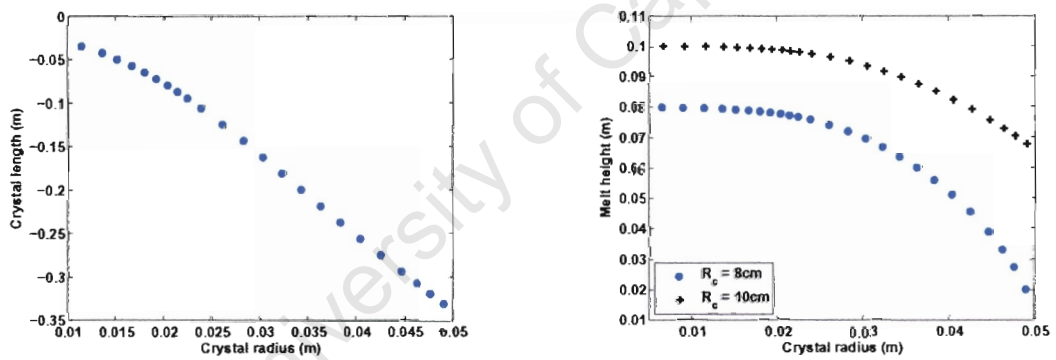

(a) Typical InSb crystal growth profile

(b) Corresponding fluid heights

Figure 4.6: Input values for coupled calculation

Figure 4.6(a) shows the crystal shape data used in this calculation. The values for the crystal profile are interpolated from actual crystal data shown in Figure 2.2. The crucible is assumed full initially, and the corresponding melt heights were calculated for two different crucible sizes: $\hat{R}_c = 0.1$ m, 0.08 m, presented in Figure 4.6(b). The parameters used are again those presented in Table 3.1.

Using these profiles the height of the fluid in the crucible and the crystal radius are updated at each calculation. Figure 4.7 shows the core temperature and rotational

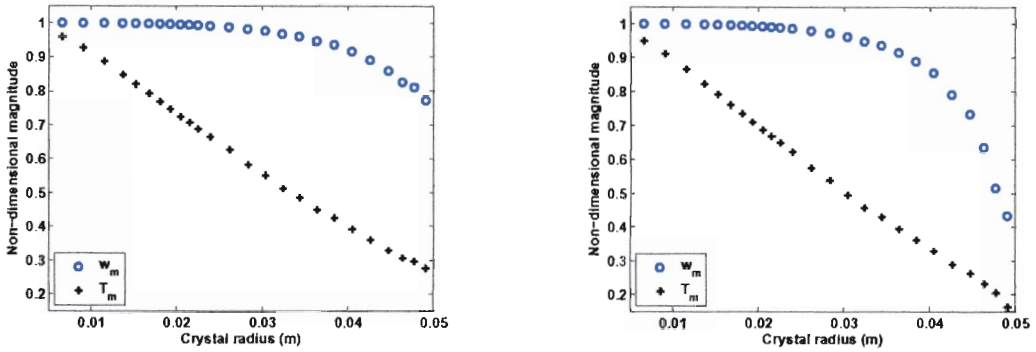

(a) $\hat{R}_c = 0.1$ m (b) $\hat{R}_c = 0.08$ m

Figure 4.7: Calculated core temperature and rotation rates

velocity values throughout the growth process. Figure 4.7(a) shows a core temperature decrease that is almost linear. This is surprising since the heat flow to the crystal should be proportional to the area or radius squared. It is likely the melt height decreasing has the effect of cancelling out any curvature due to the mass balance between the crystal and fluid height. If the melt height were constant then the core temperature would drop even faster. The core temperature seems to be mainly dependent on the crystal radius itself, not the cross-sectional area.

Notice the crystal rotation ω_m is constant until $\hat{r} = 3$ cm, shown in Figure 4.7(b). The geometry of the small crystal and large crucible radius initially favour the crucible in terms of rotation, but as the crystal gets larger the counter rotation becomes substantial. Comparing the rotation curve with the fluid height profile in Figure 4.6(b), the crystal rotation appears to be strongly dependent on the drop in fluid height, and to a lesser extent the crystal radius. The dramatic slowing of the rotation towards the end of the growth period could contribute to having the melt freeze, or other undesirable effects on the crystal.

Figure 4.8 shows a comparison of the temperature gradient and the total heat flow from the melt to the crystal, with $\hat{R}_c = 0.1$ m. The interesting point here is that the temperature gradient is extremely high initially and decays rapidly. This profile suggests the assumed constant temperature difference between the crystal and crucible $\Delta T = 10K$ may be unrealistic. Clearly if the melt heat flux varied by al-

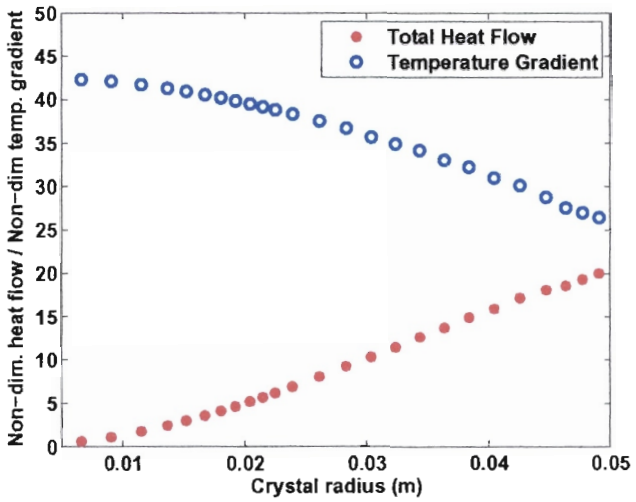

Figure 4.8: Comparison of heat flow and temperature gradient at crystal

most a factor of 2, pulling the crystal at a constant rate would be impossible. This gives a new purpose to our model: to obtain a realistic crucible temperature profile suitable for crystal growth. This idea will be dealt with in detail in Chapter 7, as an application of the quasi-steady model.

4.7 Summary

The asymptotic approach developed in this chapter is useful because it provides a solution to the melt flow equations that is valid at low Prandtl numbers. The calculation time is short and is intended to capture the dominant behaviour of the melt flow field without resorting to CFD. The asymptotic model is capable of providing an overall or average picture of a Czochralski melt, and can also determine the heat flux to the crystal.

An interesting observation was made by looking at the crucible boundary layer equation (4.28), which predicts the flow field is most likely to change direction at the midpoint of the crucible, if sufficient counter rotation is present. This type of observation would unlikely be noticed by looking at results from only numerical or

CFD solutions. This is important in order to maintain a consistent flow structure and demonstrates the usefulness of asymptotic approximations.

We also learned, at the end of §4.6 that a constant crucible wall temperature over the entire growth process is unrealistic. The asymptotic flow calculation can be used to develop a heating strategy, based on the crucible wall temperature. This type of analysis will be performed in Chapter 7.

The main purpose of the asymptotic flow model is to be used with the solidification model for the crystal, derived in Chapter 2. Then we will be able to show directly how the melt conditions affect crystal growth. Before doing so, it is necessary to validate the asymptotic model with a numerical solution.

Chapter 5

Melt Fluid Mechanics III: Finite Element Solution

In the previous chapter, an asymptotic model was constructed that satisfies the Navier-Stokes equations by assuming the presence of a core region surrounded by boundary layers. In this chapter, we will make use of the Finite Element (FE) method to solve the full incompressible Navier-Stokes equations (3.11)-(3.15).

5.1 Previous Work and Motivation

The Finite Element Method is one of the most powerful computational techniques available to mathematicians and engineers. This method is a generalization of classical variational techniques, for example the Ritz method [66] and weighted-residual methods (Galerkin, least-squares [67]). The basic premise is to represent the solution of partial differential equations (PDEs) as a linear combination of unknown parameters and appropriately selected functions over the entire domain. The unknown parameters are then determined such that the differential is satisfied in a

weighted-residual sense.

The limitation of this approach is the difficulty in constructing an approximation function to satisfy the PDEs and the boundary conditions. Finding a function that can approximate physically realistic boundary conditions on complex geometry can be very difficult, if not impossible. If the domain can be approximated by a collection of smaller sub-domains, then piecewise approximations can be used instead of a single function over the entire domain. This is essentially the idea behind the Finite Element Method. Subdivide the domain into smaller regions, and use an element wise approximation (with interpolation functions) on each sub-domain, then reassemble the element equations into a global system to obtain an approximation to the full system of equations.

The analysis for this work is taken primarily by the methods given in the work by Reddy and Gartling [68], although we deviate slightly. Their summary of mixed finite elements for incompressible flow and convective heat transfer are used in this work, and adapted to an axisymmetric system.

5.2 Geometry and Coordinate System

A 1/4 circle domain, defined by Ω, is all that is needed to represent the crucible geometry due to the azimuthal symmetry. The triangle is the standard element shape used to subdivide the crucible domain, chosen for its simplicity.

5.2.1 Discretization of Domain (Meshing)

The domain Ω is discretized into triangular non-uniform subdomains Ω_e. The aim here is to have relatively small elements and therefore obtain higher resolution near the solid boundaries, where it is believed that the solution will change rapidly. This is also desirable in order to resolve any boundary layers, if present. Two of the meshes that were used are presented in Figure 5.1.

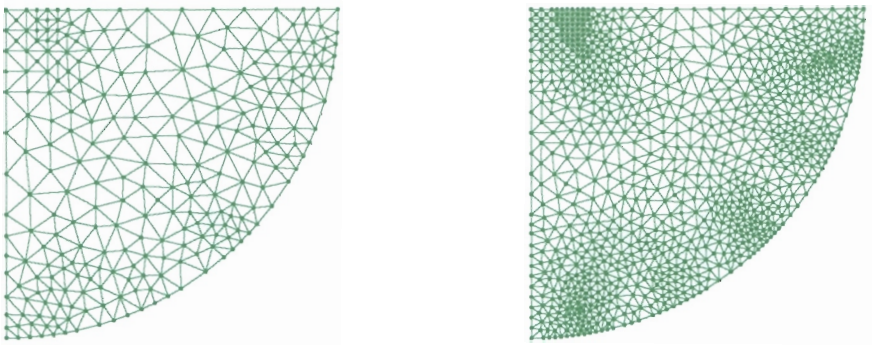

Figure 5.1: Coarse mesh with 518 vertices and 294 elements and refined mesh with 1118 and 571 elements

The unstructured meshes were generated using the GRUMMP software developed by Ollivier-Gooch [69]. Notice we attempt to have more cells near the crucible wall and crystal boundaries to detect rapidly changing solutions. In order to automate the calculation (or integration) it is desirable to transform every triangle in the domain to a standard triangle. This is a standard transformation that is described most modern Finite Element textbooks.

5.2.2 Coordinate Transformation

To simplify the calculation of integrals, it is convenient to map all triangles to a standard triangle using a coordinate mapping, known as *area coordinates* for Lagrange elements. First, denote any triangular element vertices: $(v_1, v_2, v_3) = ([r_1, z_1], [r_2, z_2], [r_3, z_3])$, in the global coordinate system of (r, z). Area coordinates can be defined to map any point from the global system (r, z) to a local coordinate system (L_1, L_2, L_3) using the following relations:

$$L_1 r_1 + L_2 r_2 + L_3 r_3 = r, \tag{5.1}$$

$$L_1 z_1 + L_2 z_2 + L_3 z_3 = z, \tag{5.2}$$

$$L_1 + L_2 + L_3 = 1, \tag{5.3}$$

which is solved simultaneously to give:

$$L_1 = a_1 + b_1 r + c_1 z \tag{5.4}$$

$$L_2 = a_2 + b_2 r + c_2 z \tag{5.5}$$

$$L_3 = a_3 + b_3 r + c_3 z. \tag{5.6}$$

The values for the coefficients a_i, b_i, c_i in equations (5.4)-(5.6) are given by:

$$a_1 = \frac{r_2 z_3 - r_3 z_2}{A} \quad a_2 = \frac{r_3 z_1 - r_1 z_3}{A} \quad a_3 = \frac{r_1 z_2 - r_2 z_1}{A} \tag{5.7}$$

$$b_1 = \frac{z_2 - z_3}{A} \quad b_2 = \frac{z_3 - z_1}{A} \quad b_3 = \frac{z_1 - z_2}{A} \tag{5.8}$$

$$c_1 = \frac{r_3 - r_2}{A} \quad c_2 = \frac{r_1 - r_3}{A} \quad c_3 = \frac{r_2 - r_1}{A} \tag{5.9}$$

where A is the area of the triangle in the global system.

5.2.3 Element Interpolation Functions

The interpolation functions used in this work are the linear and quadratic Lagrange functions for a triangular element. It is well known that instabilities arise (see [70, 71]) if equal order interpolation functions are used for the pressure and velocity variables. To overcome this the velocity interpolation function will be one order higher than the pressure, which is a stable formulation according to the work of Taylor [72]. The linear interpolation function in area coordinates has the following form:

$$\Phi_1 = L_1 \quad \Phi_2 = L_2 \quad \Phi_3 = L_3 \tag{5.10}$$

The coordinates for any triangle vertices in terms of Φ become
$([r_1, z_1], [r_2, z_2], [r_3, z_3]) = ([1, 0, 0], [0, 1, 0], [0, 0, 1])$.

For the quadratic elements (velocity and temperature variables), the following quadratic interpolation functions are used for a triangular element, with 6 nodes:

$$\psi_1 = L_1(2L_1 - 1) \quad \psi_2 = L_2(2L_2 - 1) \quad \psi_3 = L_3(2L_3 - 1)$$

$$\psi_4 = 4L_2L_3 \quad \psi_5 = 4L_1L_3 \quad \psi_6 = 4L_1L_2 \tag{5.11}$$

The coordinates for the vertices in terms of ψ are

$([r_1, z_1], [r_2, z_2], [r_3, z_3]) = ([1, 0, 0, 0, 0, 0], [0, 1, 0, 0, 0, 0], [0, 0, 1, 0, 0, 0])$

in the natural form. The additional nodes are then given by:

$([0, 0, 0, 1, 0, 0], [0, 0, 0, 0, 1, 0], [0, 0, 0, 0, 0, 1])$.

The triangles for the linear and quadratic elements are presented in Figure 5.2. The

Figure 5.2: Linear triangle (left) and quadratic triangle (right) used in calculations

linear triangular element has 3 components in its interpolation function (Φ), and the quadratic element has 6 components in its interpolation function (ψ). In this formulation, the nodal values will correspond to the results in primitive variable form.

5.3 Weak Form

The next step is to obtain the weak form of the 2D axisymmetric Navier-Stokes equations (3.11)-(3.15) derived in Chapter 3. This method consists of multiplying the equations by a test function, either N or w, and integrating the system over each element:

$$\int_{\Omega_e} N \left[\frac{\partial u_r}{\partial r} + \frac{u_r}{r} + \frac{\partial u_z}{\partial z} \right] d\Omega = 0 \tag{5.12}$$

$$\int_{\Omega_e} w \left[u_r \frac{\partial u_r}{\partial r} + u_z \frac{\partial u_r}{\partial z} - \frac{u_\theta^2}{r} + \frac{\partial P}{\partial r} \right. \tag{5.13}$$

$$-\frac{\mathrm{Pr}}{\mathrm{Bo}^{1/2}}\left(\frac{\partial^2 u_r}{\partial r^2}+\frac{1}{r}\frac{\partial u_r}{\partial r}-\frac{u_r}{r^2}+\frac{\partial^2 u_r}{\partial z^2}\right)\Bigg]\,d\Omega=0$$

$$\int_{\Omega_e} w\left[u_r\frac{\partial u_\theta}{\partial r}+u_z\frac{\partial u_\theta}{\partial z}+\frac{u_r u_\theta}{r}\right. \tag{5.14}$$
$$\left.-\frac{\mathrm{Pr}}{\mathrm{Bo}^{1/2}}\left(\frac{\partial^2 u_\theta}{\partial r^2}+\frac{1}{r}\frac{\partial u_\theta}{\partial r}-\frac{u_\theta}{r^2}+\frac{\partial^2 u_\theta}{\partial z^2}\right)\right]d\Omega=0$$

$$\int_{\Omega_e} w\left[u_r\frac{\partial u_z}{\partial r}+u_z\frac{\partial u_z}{\partial z}+\frac{\partial P}{\partial z}\right. \tag{5.15}$$
$$\left.-\frac{\mathrm{Pr}}{\mathrm{Bo}^{1/2}}\left(\frac{\partial^2 u_z}{\partial r^2}+\frac{1}{r}\frac{\partial u_z}{\partial r}+\frac{\partial^2 u_z}{\partial z^2}\right)-T\right]d\Omega=0$$

$$\int_{\Omega_e} w\left[u_r\frac{\partial T}{\partial r}+u_z\frac{\partial T}{\partial z}-\frac{1}{\mathrm{Bo}^{1/2}}\left(\frac{\partial^2 T}{\partial r^2}+\frac{1}{r}\frac{\partial T}{\partial r}+\frac{\partial^2 T}{\partial z^2}\right)\right]d\Omega=0 \tag{5.16}$$

The integrations are performed over a differential area $d\Omega = rdrdz$. The equations are simplified by using integration by parts and the Divergence Theorem (see Reddy [73] for details). The final variational system in weak form is then

$$\int_{d\Omega_e}\left(N\frac{\partial u_r}{\partial r}+N\frac{u_r}{r}+N\frac{\partial u_z}{\partial z}\right)d\Omega=0 \tag{5.17}$$

$$\int_{\Omega_e}\left(wu_r\frac{\partial u_r}{\partial r}+wu_z\frac{\partial u_r}{\partial z}-w\frac{u_\theta^2}{r}-\frac{\partial w}{\partial r}P-wP\right)d\Omega \tag{5.18}$$
$$+\frac{\mathrm{Pr}}{\mathrm{Bo}^{1/2}}\int_{\Omega_e}\left(\frac{\partial w}{\partial r}\frac{\partial u_r}{\partial r}+\frac{\partial w}{\partial z}\frac{\partial u_r}{\partial z}+w\frac{u_r}{r^2}\right)d\Omega-\oint_{d\Gamma_e} w\Upsilon_r ds=0$$

$$\int_{\Omega_e}\left(wu_r\frac{\partial u_\theta}{\partial r}+wu_z\frac{\partial u_\theta}{\partial z}+w\frac{u_r u_\theta}{r}\right)d\Omega \tag{5.19}$$
$$+\frac{\mathrm{Pr}}{\mathrm{Bo}^{1/2}}\int_{\Omega_e}\left(\frac{\partial w}{\partial r}\frac{\partial u_\theta}{\partial r}+\frac{\partial w}{\partial z}\frac{\partial u_\theta}{\partial z}+w\frac{u_\theta}{r^2}\right)d\Omega-\oint_{d\Gamma_e} w\Upsilon_\theta ds=0$$

$$\int_{\Omega_e}\left(wu_r\frac{\partial u_z}{\partial r}+wu_z\frac{\partial u_z}{\partial z}-\frac{\partial w}{\partial z}P-wT\right)d\Omega \tag{5.20}$$
$$+\frac{\mathrm{Pr}}{\mathrm{Bo}^{1/2}}\int_{\Omega_e}\left(\frac{\partial w}{\partial r}\frac{\partial u_z}{\partial r}+\frac{\partial w}{\partial z}\frac{\partial u_z}{\partial z}\right)d\Omega-\oint_{d\Gamma_e}w\Upsilon_z ds=0$$

$$\int_{\Omega_e}\left(wu_r\frac{\partial T}{\partial r}+wu_z\frac{\partial T}{\partial z}\right)d\Omega \tag{5.21}$$
$$+\frac{1}{\mathrm{Bo}^{1/2}}\int_{\Omega_e}\left(\frac{\partial w}{\partial r}\frac{\partial T}{\partial r}+\frac{\partial^2 w}{\partial z^2}\frac{\partial T}{\partial z}\right)d\Omega-\oint_{d\Gamma_e}w\Upsilon_T ds=0.$$

Note the term Υ denotes the left over terms from using the Divergence Theorem in the boundary integral.

5.3.1 Finite Element Method

As mentioned in the previous subsection, the weight functions are restricted such that the pressure interpolation function must be one order lower than the velocity and temperature. Therefore, all variables can be approximated by the expansions

$$P(r,z)=\sum_{i=1}^{m}\phi_i(r,z)P(i)=\Phi^T\mathbf{P} \tag{5.22}$$
$$u_r(r,z)=\sum_{i=1}^{n}\psi_i(r,z)u_r(i)=\Psi^T\mathbf{u_r} \tag{5.23}$$
$$u_\theta(r,z)=\sum_{i=1}^{n}\psi_i(r,z)u_\theta(i)=\Psi^T\mathbf{u}_\theta \tag{5.24}$$
$$u_z(r,z)=\sum_{i=1}^{n}\psi_i(r,z)u_z(i)=\Psi^T\mathbf{u_z} \tag{5.25}$$
$$T(r,z)=\sum_{i=1}^{n}\psi_i(r,z)T(i)=\Psi^T\mathbf{T} \tag{5.26}$$

where Ψ and Φ are column vectors of interpolation presented in the previous section, and $\mathbf{P}, \mathbf{u_r}, \mathbf{u}_\theta, \mathbf{u_z}, \mathbf{T}$ are column vectors of the nodal values for the pressure, velocity components and temperature respectively.

Any weight function is admissible so we choose the weight functions to be the same

as the interpolation functions, evaluated at each point

$$N(r,z) = \phi_j(r,z) \qquad w(r,z) = \psi_j(r,z). \tag{5.27}$$

These substitutions lead to the vector form of the finite element equations

Continuity

$$\left[\int_{\Omega_e}\left(\Phi\frac{\partial\Psi^T}{\partial r} + \Phi\frac{\Psi^T}{r}\right)d\Omega\right]\mathbf{u_r} + \left[\int_{\Omega_e}\Phi\frac{\partial\Psi^T}{\partial z}d\Omega\right]\mathbf{u_z} = 0 \tag{5.28}$$

Momentum (r,θ,z)

$$\begin{aligned}&\left[\int_{\Omega_e}\left(\Psi u_r\frac{\partial\Psi^T}{\partial r} + \Psi u_z\frac{\partial\Psi^T}{\partial z}\right)d\Omega\right]\mathbf{u_r} - \left[\int_{\Omega_e}\Psi\frac{u_\theta}{r}\Psi^T d\Omega\right]\mathbf{u}_\theta \\ &- \left[\int_{\Omega_e}\left(\frac{\partial\Psi}{\partial r}\Phi^T + \frac{\Psi\Phi^T}{r}\right)d\Omega\right]\mathbf{P} + \frac{\mathrm{Pr}}{\mathrm{Bo}^{1/2}}\left[\int_{\Omega_e}\left(\frac{\partial\Psi}{\partial r}\frac{\partial\Psi^T}{\partial r} + \frac{\partial\Psi}{\partial z}\frac{\partial\Psi^T}{\partial z} + \Psi\frac{\Psi^T}{r^2}\right)d\Omega\right]\mathbf{u_r} \\ &- \oint_{d\Gamma_e} w\Upsilon_r ds = 0\end{aligned} \tag{5.29}$$

$$\begin{aligned}&\left[\int_{\Omega_e}\left(\Psi u_r\frac{\partial\Psi^T}{\partial r} + \Psi u_z\frac{\partial\Psi^T}{\partial z}\right)d\Omega\right]\mathbf{u}_\theta + \left[\int_{\Omega_e}\Psi\frac{u_\theta}{r}\Psi^T d\Omega\right]\mathbf{u_r} \\ &+\frac{\mathrm{Pr}}{\mathrm{Bo}^{1/2}}\left[\int_{\Omega_e}\left(\frac{\partial\Psi}{\partial r}\frac{\partial\Psi^T}{\partial r} + \frac{\partial\Psi}{\partial z}\frac{\partial\Psi^T}{\partial z} + \Psi\frac{\Psi^T}{r^2}\right)d\Omega\right]\mathbf{u}_\theta - \oint_{d\Gamma_e} w\Upsilon_\theta ds = 0\end{aligned} \tag{5.30}$$

$$\begin{aligned}&\left[\int_{\Omega_e}\left(\Psi u_r\frac{\partial\Psi^T}{\partial r} + \Psi u_z\frac{\partial\Psi^T}{\partial z}\right)d\Omega\right]\mathbf{u_z} - \left[\int_{\Omega_e}\frac{\partial\Psi}{\partial z}\Phi^T d\Omega\right]\mathbf{P} \\ &+\frac{\mathrm{Pr}}{\mathrm{Bo}^{1/2}}\left[\int_{\Omega_e}\left(\frac{\partial\Psi}{\partial r}\frac{\partial\Psi^T}{\partial r} + \frac{\partial\Psi}{\partial z}\frac{\partial\Psi^T}{\partial z}\right)d\Omega\right]\mathbf{u_z} - \left[\int_{\Omega_e}\Psi\Psi^T d\Omega\right]\mathbf{T} - \oint_{d\Gamma_e} w\Upsilon_z ds = 0\end{aligned} \tag{5.31}$$

Energy

$$\begin{aligned}&\left[\int_{\Omega_e}\left(\Psi u_r\frac{\partial\Psi^T}{\partial r} + \Psi u_z\frac{\partial\Psi^T}{\partial z}\right)d\Omega\right]\mathbf{T} \\ &+\frac{\mathrm{Pr}}{\mathrm{Bo}^{1/2}}\left[\int_{\Omega_e}\left(\frac{\partial\Psi}{\partial r}\frac{\partial\Psi^T}{\partial r} + \frac{\partial\Psi}{\partial z}\frac{\partial\Psi^T}{\partial z}\right)d\Omega\right]\mathbf{T} - \oint_{d\Gamma_e} w\Upsilon_T ds = 0\end{aligned} \tag{5.32}$$

These equations still contain the primitive variables (u_r, u_θ, u_z) in the non-linear terms. It is necessary to linearize equations (5.29)-(5.32) before putting them into matrix form.

5.3.2 Linearization

In order to obtain a consistent matrix form, the above system needs to be transformed from a non-linear system of equations to a linear set. This is accomplished by assuming part of the non-linear velocity terms are constant or known, and iterated until they converge to the actual solution. Initially, the constant values are taken to be zero, which is equivalent to solving the Stokes flow problem. The solution progresses using the velocities from the previous iteration. This is known as the Picard iteration scheme [74], and can be described for each iteration k by denoting:

$$(U_r, U_\theta, U_z) = \begin{cases} 0 & k = 1 \\ (u_r, u_\theta, u_z)^{k-1} & k > 1 \end{cases}$$

The variational integrals are then given by:

Continuity

$$\left[\int_{\Omega_e} \left(\Phi \frac{\partial \Psi^T}{\partial r} + \frac{\Phi \Psi^T}{r}\right) d\Omega\right] \mathbf{u_r} + \left[\int_{\Omega_e} \Phi \frac{\partial \Psi^T}{\partial z} d\Omega\right] \mathbf{u_z} = 0 \tag{5.33}$$

Momentum (r, θ, z)

$$\begin{aligned} &\left[\int_{\Omega_e} \left(U_r \Psi \frac{\partial \Psi^T}{\partial r} + U_z \Psi \frac{\partial \Psi^T}{\partial z}\right) d\Omega\right] \mathbf{u_r} - \left[\int_{\Omega_e} \frac{U_\theta \Psi \Psi^T}{r} d\Omega\right] \mathbf{u}_\theta \\ &+ \left[\int_{\Omega_e} \left(\frac{\partial \Psi}{\partial r} \Phi^T + \frac{\Psi \Phi^T}{r}\right) d\Omega\right] \mathbf{P} + \frac{\mathrm{Pr}}{\mathrm{Bo}^{1/2}} \left[\int_{\Omega_e} \left(\frac{\partial \Psi}{\partial r}\frac{\partial \Psi^T}{\partial r} + \frac{\partial \Psi}{\partial z}\frac{\partial \Psi^T}{\partial z} + \frac{\Psi \Psi^T}{r^2}\right) d\Omega\right] \mathbf{u_r} \\ &- \oint_{d\Gamma_e} w \Upsilon_r ds = 0 \end{aligned} \tag{5.34}$$

$$\begin{aligned} &\left[\int_{\Omega_e} \left(U_r \Psi \frac{\partial \Psi^T}{\partial r} + U_z \Psi \frac{\partial \Psi^T}{\partial z}\right) d\Omega\right] \mathbf{u}_\theta + \left[\int_{\Omega_e} \frac{U_\theta \Psi \Psi^T}{r} d\Omega\right] \mathbf{u_r} \\ &+ \frac{\mathrm{Pr}}{\mathrm{Bo}^{1/2}} \left[\int_{\Omega_e} \left(\frac{\partial \Psi}{\partial r}\frac{\partial \Psi^T}{\partial r} + \frac{\partial \Psi}{\partial z}\frac{\partial \Psi^T}{\partial z} + \frac{\Psi \Psi^T}{r^2}\right) d\Omega\right] \mathbf{u}_\theta - \oint_{d\Gamma_e} w \Upsilon_\theta ds = 0 \end{aligned} \tag{5.35}$$

$$\begin{aligned} &\left[\int_{\Omega_e} \left(U_r \Psi \frac{\partial \Psi^T}{\partial r} + U_z \Psi \frac{\partial \Psi^T}{\partial z}\right) d\Omega\right] \mathbf{u_z} + \left[\int_{\Omega_e} \frac{\partial \Psi}{\partial z} \Phi^T d\Omega\right] \mathbf{P} \\ &+ \frac{\mathrm{Pr}}{\mathrm{Bo}^{1/2}} \left[\int_{\Omega_e} \left(\frac{\partial \Psi}{\partial r}\frac{\partial \Psi^T}{\partial r} + \frac{\partial \Psi}{\partial z}\frac{\partial \Psi^T}{\partial z}\right) d\Omega\right] \mathbf{u_z} - \left[\int_{\Omega_e} \Psi \Psi^T d\Omega\right] \mathbf{T} - \oint_{d\Gamma_e} w \Upsilon_z ds = 0 \end{aligned} \tag{5.36}$$

Energy

$$\left[\int_{\Omega_e}\left(U_r\Psi\frac{\partial\Psi^T}{\partial r}+U_z\Psi\frac{\partial\Psi^T}{\partial z}\right)d\Omega\right]\mathbf{T} \\ +\frac{\mathrm{Pr}}{\mathrm{Bo}^{1/2}}\left[\int_{\Omega_e}\left(\frac{\partial\Psi}{\partial r}\frac{\partial\Psi^T}{\partial r}+\frac{\partial\Psi}{\partial z}\frac{\partial\Psi^T}{\partial z}\right)d\Omega\right]\mathbf{T}-\oint_{d\Gamma_e}w\Upsilon_T ds=0 \tag{5.37}$$

5.4 Matrix Formulation

The integrals in the system of equations (5.34)-(5.37) must be evaluated over each element yielding a local stiffness matrix, denoted with lower case variables. The local stiffness matrices are then entered into a global stiffness matrix that yields the global approximation. The following matrices are defined for each element

$$k_{11}=k_{22}=\frac{\mathrm{Pr}}{\mathrm{Bo}^{1/2}}\int_{\Omega_e}\left(\frac{\partial\Psi}{\partial r}\frac{\partial\Psi^T}{\partial r}+\frac{\partial\Psi}{\partial z}\frac{\partial\Psi^T}{\partial z}+\frac{\Psi\Psi^T}{r^2}\right)d\Omega \tag{5.38}$$

$$k_{33}=\frac{\mathrm{Pr}}{\mathrm{Bo}^{1/2}}\int_{\Omega_e}\left(\frac{\partial\Psi}{\partial r}\frac{\partial\Psi^T}{\partial r}+\frac{\partial\Psi}{\partial z}\frac{\partial\Psi^T}{\partial z}\right)d\Omega \tag{5.39}$$

$$k_{44}=\frac{1}{\mathrm{Bo}^{1/2}}\int_{\Omega_e}\left(\frac{\partial\Psi}{\partial r}\frac{\partial\Psi^T}{\partial r}+\frac{\partial\Psi}{\partial z}\frac{\partial\Psi^T}{\partial z}\right)d\Omega \tag{5.40}$$

$$n_1=\int_{\Omega_e}\left(U_r\Psi\frac{\partial\Psi^T}{\partial r}+U_z\Psi\frac{\partial\Psi^T}{\partial z}\right)d\Omega,\qquad n_2=\int_{\Omega_e}\frac{U_\theta\Psi\Psi^T}{r}d\Omega \tag{5.41}$$

$$q_1=\int_{\Omega_e}\left(\frac{\partial\Psi}{\partial r}\Phi^T+\frac{\Psi\Phi^T}{r}\right)d\Omega,\quad q_3=\int_{\Omega_e}\frac{\partial\Psi}{\partial z}\Phi^T d\Omega,\quad h_1=\int_{\Omega_e}\Psi\Psi^T d\Omega. \tag{5.42}$$

In order to evaluate integrals (5.38)-(5.42), a 4-point numerical quadrature was implemented, with the coordinates and weights presented in Table 5.1. The evaluation points are shown schematically in Figure 5.3. This system was used because of the

L_1	L_2	L_3	W	Location	m
1/3	1/3	1/3	-27/48	a	1
0.6	0.2	0.2	25/48	b	2
0.2	0.6	0.2	25/48	c	3
0.2	0.2	0.6	25/48	d	4

Table 5.1: Integration Points and Weights

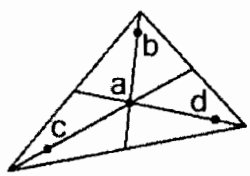

Figure 5.3: Integration point locations

axisymmetric formulation. Since all of the points on the triangle are internal, the $1/r$ terms will not be singular at the boundary $r = 0$. This quadrature is exact for polynomials of degree ≤ 3.

Evaluating integrals (5.38)-(5.42) also requires mapping each triangle to the standard triangle, performing the integration and then multiplying by the Jacobian. For example, the Laplacian of the radial velocity (u_r) is

$$k_{11} = \frac{\mathrm{Pr}}{\mathrm{Bo}^{1/2}} \int_{\Omega_e} \left(\frac{\partial \Psi}{\partial r}\frac{\partial \Psi^T}{\partial r} + \frac{\partial \Psi}{\partial z}\frac{\partial \Psi^T}{\partial z} + \frac{\Psi \Psi^T}{r^2} \right) d\Omega, \tag{5.43}$$

which can be evaluated by

$$k_{11} = \frac{\mathrm{Pr}}{\mathrm{Bo}^{1/2}} \triangle \sum_{i=1}^{4} \left(\frac{\partial \Psi}{\partial r}\frac{\partial \Psi^T}{\partial r} + \frac{\partial \Psi}{\partial z}\frac{\partial \Psi^T}{\partial z} + \frac{\Psi \Psi^T}{r^2} \right)\Bigg|_{(m)} r(m)W(m). \tag{5.44}$$

Here $\triangle$ is the area of the triangle, and m denotes the integration point where the variables are being evaluated. The same methodology is applied to calculating the other matrices in the system (5.38)-(5.42).

The next step is to add each individual element contribution to the global stiffness matrix. To distinguish a local element node from a global node we let i_g denote a global node index and i_l correspond to a local node index. The element contribution

are summed to give

$$K_{11}(i_g) = \sum_{e=1}^{n} k_{11}^e(i_l) \quad K_{22}(i_g) = \sum_{e=1}^{n} k_{22}^e(i_l) \quad K_{33}(i_g) = \sum_{e=1}^{n} k_{33}^e(i_l) \tag{5.45}$$

$$K_{44}(i_g) = \sum_{e=1}^{n} k_{44}^e(i_l) \quad N_1(i_g) = \sum_{e=1}^{n} n_1^e(i_l) \quad N_2(i_g) = \sum_{e=1}^{n} n_2^e(i_l) \tag{5.46}$$

$$Q_1(i_g) = \sum_{e=1}^{n} q_1^e(i_l) \quad Q_2(i_g) = \sum_{e=1}^{n} q_2^e(i_l) \quad H_1(i_g) = \sum_{e=1}^{n} h_1^e(i_l). \tag{5.47}$$

The resulting matrices can be combined to form the global stiffness matrix $\mathbf{A}$:

$$\begin{bmatrix} K_{11}+N_1 & -N_2 & 0 & 0 & -Q_1 \\ N_2 & K_{22}+N_1 & 0 & 0 & 0 \\ 0 & 0 & K_{33}+N_1 & -H_1 & -Q_3 \\ 0 & 0 & 0 & K_{44}+N_1 & 0 \\ -Q_1^T & 0 & -Q_3^T & 0 & 0 \end{bmatrix} \begin{bmatrix} \mathbf{u_r} \\ \mathbf{u_\theta} \\ \mathbf{u_z} \\ \mathbf{T} \\ \mathbf{P} \end{bmatrix} = 0.$$

These element stiffness matrices are assembled into the global form by relating the local nodes for each element to the global nodes for the entire domain. The result is a system of linear equations that is $(4N + L)$ by $(4N + L)$, where N is the number of quadratic nodes and L is the number of linear nodes in the mesh.

$$\mathbf{Ax} = \mathbf{b} \tag{5.48}$$

where $\mathbf{x}$ is a vector containing the nodal values of the velocity, temperature and pressure; $\mathbf{b}$ is the global load vector.

The only remaining operation is to make the pressure field non-unique otherwise system (5.48) will remain ill-conditioned. Before solving for the flow field, the pressure at the top right of the crucible is set to zero, then it is possible solve the linear system of equations.

5.4.1 Relaxation Factor

In order to reduce or damp out oscillations that can occur in the Picard iteration scheme (again, see [68]), a relaxation factor is often used. The relaxation factor

slows the variation of the solution, for example at step k the solution to the flow field would be determined by:

$$\mathbf{x}^{k+1} = (1-\gamma)\mathbf{x}^k + \gamma \mathbf{A}^{-1}\mathbf{b}. \tag{5.49}$$

The relaxation factor γ is a value chosen between zero and one.

5.5 Results for a Specified Flow Field

The purpose of this section is to test the solver accuracy and to perform sample calculations. In Chapter 6, results will be presented for the actual flow field for the Czochralski process. For the moment, we wish to show equations (3.11)-(3.15) are solved properly with a specified flow field. The FE solver was tested by imposing boundary conditions for a flow field that identically satisfies the Navier-Stokes equations. The specified flow field is

$$u_r = r, \quad u_\theta = 2rz, \quad u_z = -2z \tag{5.50}$$

$$T = 4z - 0.5, \quad P = 1 - r - 0.5z \tag{5.51}$$

$$F_r = r - 4rz^2 - 1, \quad F_\theta = F_z = 0, \quad F_T = -8z. \tag{5.52}$$

Since quadratic elements are used for the velocity and linear elements for the pressure, the solution resides in the finite element space, and the results should be exact.

5.5.1 Solver Accuracy and Convergence

A total of seven iterations is required for the solver to converge to the specified solution (5.50)-(5.52). The convergence of the solution is presented in Table 5.2 with a minimum value of 3×10^{-11}.

It should be pointed out this error occurs in the pressure field and the velocity field was accurate to approximately 5×10^{-13}. Colour maps of the velocity, temperature and pressure fields are presented in Figures 5.4(a)-5.4(f).

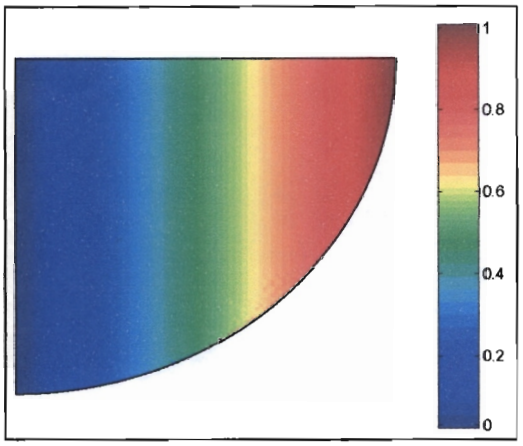

(a) Radial velocity: $u_r = r$

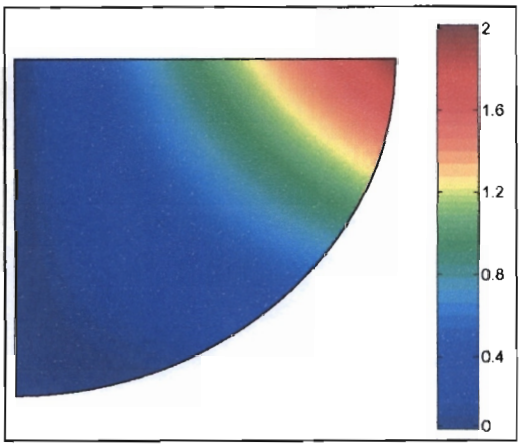

(b) Azimuthal velocity: $u_\theta = 2rz$

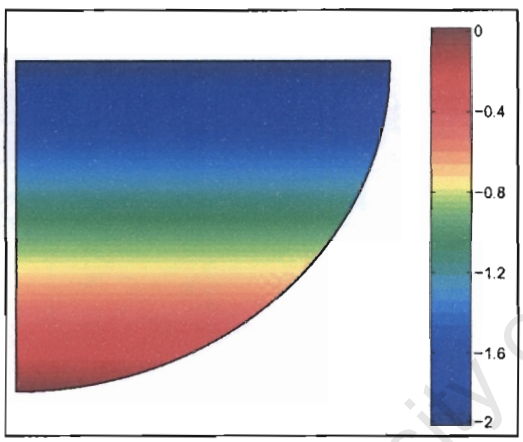

(c) Axial velocity: $u_z = -2z$

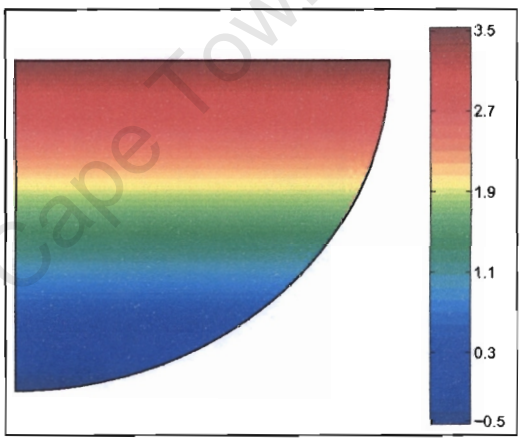

(d) Temperature: $T = 4z - 0.5$

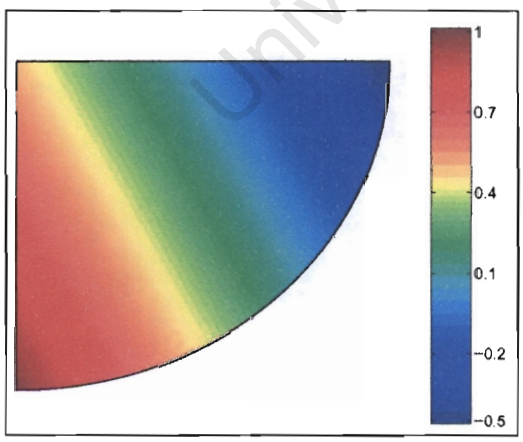

(e) Pressure: $P = 1 - r - 0.5z$

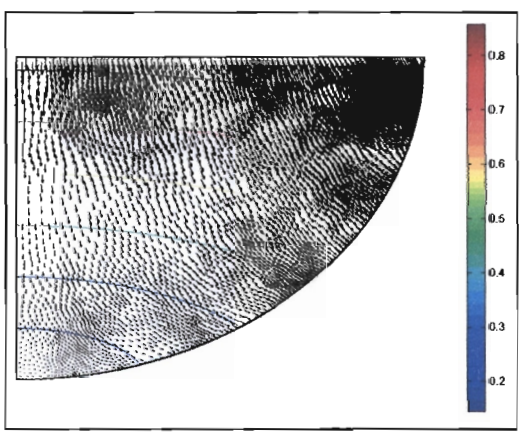

(f) Vector field: $\vec{u} = (r, -2z)$

Figure 5.4: Results from test calculation

Iteration	Node number	Max Residual
1	15790	1.98
2	15863	6.91×10^{-3}
3	15928	1.04×10^{-4}
4	15928	8.54×10^{-7}
5	15881	1.32×10^{-8}
6	15834	4.50×10^{-10}
7	16047	3.85×10^{-11}

Table 5.2: Convergence of FE solver on test case

5.5.2 Heat Flux / Torque Calculation

The important output values are the temperature and azimuthal velocity gradients at the crystal and crucible boundaries. The temperature gradient is vital because it directly affects the crystal solidification rate. The azimuthal velocity gradient can be related to the torque on the crystal and is used to validate the asymptotic model developed in Chapter 4.

These values are obtained by differentiating the interpolation functions and evaluating the solutions at the boundary nodes. We begin by differentiating the quadratic interpolation function

$$\frac{\partial \psi}{\partial r} = \frac{\partial \psi}{\partial L_1}\frac{\partial L_1}{\partial r} + \frac{\partial \psi}{\partial L_2}\frac{\partial L_2}{\partial r} + \frac{\partial \psi}{\partial L_3}\frac{\partial L_3}{\partial r}, \tag{5.53}$$

$$\frac{\partial \psi}{\partial z} = \frac{\partial \psi}{\partial L_1}\frac{\partial L_1}{\partial z} + \frac{\partial \psi}{\partial L_2}\frac{\partial L_2}{\partial z} + \frac{\partial \psi}{\partial L_3}\frac{\partial L_3}{\partial z}. \tag{5.54}$$

The derivatives of L with respect to r and z can be quickly evaluated using (5.4)-(5.6):

$$\frac{\partial L_1}{\partial r} = b_1 \quad \frac{\partial L_2}{\partial r} = b_2 \quad \frac{\partial L_3}{\partial r} = b_3, \tag{5.55}$$

$$\frac{\partial L_1}{\partial z} = c_1 \quad \frac{\partial L_2}{\partial z} = c_2 \quad \frac{\partial L_3}{\partial z} = c_3. \tag{5.56}$$

The derivative of the quadratic interpolation function with respect to L_1, L_2, L_3 are then

$$\frac{\partial \psi}{\partial L_1} = \begin{pmatrix} 4L_1 - 1 \\ 0 \\ 0 \\ 4L_2 \\ 0 \\ 4L_3 \end{pmatrix}, \quad \frac{\partial \psi}{\partial L_2} = \begin{pmatrix} 0 \\ 4L_2 - 1 \\ 0 \\ 4L_1 \\ 4L_3 \\ 0 \end{pmatrix}, \quad \frac{\partial \psi}{\partial L_2} = \begin{pmatrix} 0 \\ 0 \\ 4L_3 - 1 \\ 0 \\ 4L_2 \\ 4L_1 \end{pmatrix}.$$

Combining (5.53) with (5.55) and (5.54) with (5.56) enable the gradients of the interpolation functions to be calculated by

$$\frac{\partial \psi}{\partial r} = b_1 \frac{\partial \psi}{\partial L_1} + b_2 \frac{\partial \psi}{\partial L_2} + b_3 \frac{\partial \psi}{\partial L_1}, \qquad \frac{\partial \psi}{\partial z} = c_1 \frac{\partial \psi}{\partial L_1} + c_2 \frac{\partial \psi}{\partial L_2} + c_3 \frac{\partial \psi}{\partial L_1}. \tag{5.57}$$

The gradient of the temperature and the azimuthal velocity are then given by the vector product of the interpolation function gradients and the nodal values. At the crystal, only derivatives with respect to z are required resulting in

$$\frac{\partial T}{\partial z} = \frac{\partial \psi}{\partial z} \cdot \mathbf{T}_e, \quad \frac{\partial u_\theta}{\partial z} = \frac{\partial \psi}{\partial z} \cdot \mathbf{u}_{\theta e}, \tag{5.58}$$

where $\mathbf{T}_e$ and $\mathbf{u}_{\theta e}$ are the nodal temperature and azimuthal velocity nodal values. Equation (5.58) is sufficient to calculate the gradients at the crystal boundary using the solution at boundary elements. For the crucible wall derivatives, it is necessary to calculate the gradients with respect to the normal direction, which is given by

$$\frac{\partial T}{\partial n} = \left(-\frac{\partial \psi}{\partial r} \sin(\phi) + \frac{\partial \psi}{\partial z} \cos(\phi) \right) \cdot \mathbf{T}_e, \tag{5.59}$$

where ϕ is the corresponding position along the crucible. Similarly, the azimuthal velocity gradient is

$$\frac{\partial u_\theta}{\partial n} = \left(-\frac{\partial \psi}{\partial r} \sin(\phi) + \frac{\partial \psi}{\partial z} \cos(\phi) \right) \cdot \mathbf{u}_{\theta e}. \tag{5.60}$$

This completely defines the description of the Finite Element calculation.

Figure 5.5 shows the computed temperature and velocity gradients for the top surface of the crucible geometry at $z = 1$, for the specified flow field.

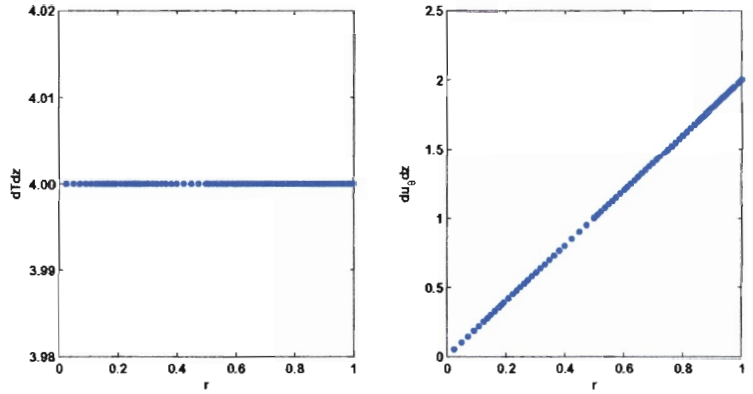

Figure 5.5: Temperature and azimuthal velocity gradients at $z = 1$

Figure 5.6 shows the temperature and velocity gradients for the crucible wall. As expected the angular velocity gradient becomes negative towards the top of the crucible.

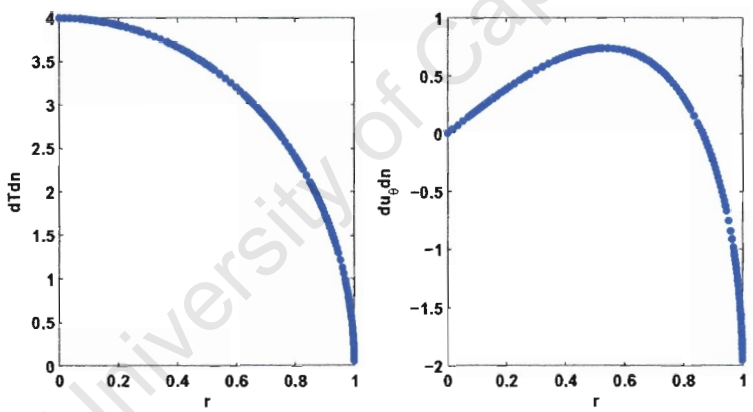

Figure 5.6: Temperature and azimuthal gradients along crucible wall

In order to compute the heat flow and torque we integrate the temperature and azimuthal gradients over the appropriate boundaries, described by equations (4.48). For the finite element calculation, the integrals must be evaluated numerically since the gradients vary with position. The numerical values for the heat flow and torque at the crucible wall and top of the crucible ($z = 1$) have been calculated. The values obtained via numerical integration are compared with the analytical values for the

specified flow field and are presented in Table 5.3.

Quantity	Computed Value	Analytical Value
Total heat at crucible wall	12.564	12.566
Total heat at fluid surface $z = 1$	12.558	12.566
Total torque at crucible wall	-2.102	-2.094
Total torque at fluid surface $z = 1$	3.140	3.142

Table 5.3: Non-dimensional heat flow and torque values for specified flow field

The results show the numerical method and gradient processing calculation is accurate within 1%. A slight interpolation error is introduced since the mesh is unstructured and the intervals are not constant width, but it is well within our necessary limits of precision. The next step is to use the solver to simulate an actual InSb melt.

5.5.3 Boundary Conditions for Melt Flow

The boundary conditions for the idealized system are summarized in Figure 5.7. At the crystal/melt interface, the temperature is specified ($T = 0$) with no-slip at the crystal surface. Since the crystal is rotating at ω_x, this becomes the boundary condition for the azimuthal velocity. We impose the crucible rotation ω_c and temperature $T = 1$ at the crucible wall. At the origin ($r = 0$), the symmetry boundary conditions are imposed. At the gas/melt interface we simplify the dynamics by fixing the fluid height at $z = H$. Since there is very little resistance to the flow by the gas we impose no-shear. The heat transfer between the gas and melt will be small in comparison to the conduction to the crystal so we assume the heat flux to the gas is zero.

Note these boundary conditions imply that all the boundary integrals are zero ($\Upsilon_r = \Upsilon_\theta = \Upsilon_z = \Upsilon_T = 0$) in the system of equations (5.33) - (5.37). The Dirichlet boundary conditions are applied by assigning a node with a specified value in the load vector. The Dirichlet boundary conditions are already satisfied by the formulation.

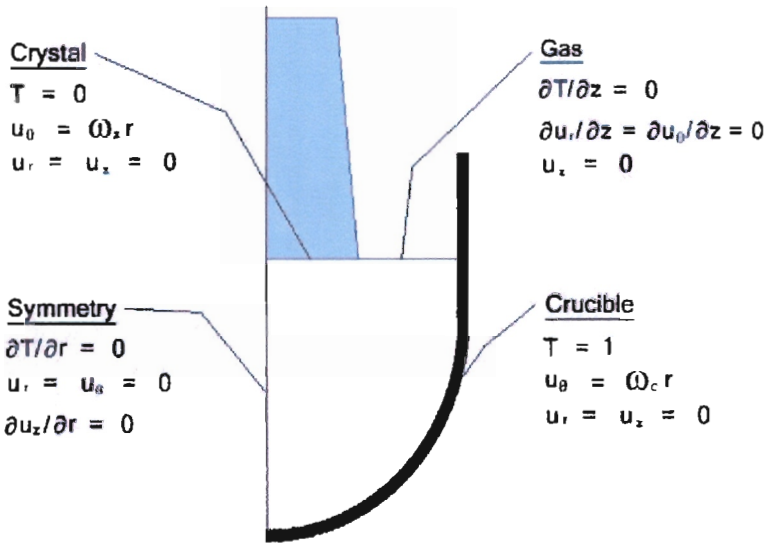

Figure 5.7: Boundary conditions for 2D axisymmetric finite element model

5.6 Summary

This chapter was dedicated to constructing a Finite Element solver for the axisymmetric Navier-Stokes equations (3.11)-(3.15). The sample calculations indicate that the solver provides an accurate approximation of the full equations.

The Finite Element approximation will be used to validate the coupled boundary layer model from Chapter 4 and to provide a more detailed description of the Czochralski crucible melt flow field. We proceed by using this solver with physically realistic boundary conditions for a melt with a Prandtl number of 0.5.

Chapter 6

Melt Structure and Coupled Boundary Layer Model Validation

The purpose of this chapter is twofold. First, we will use the Finite Element approximation developed in the previous chapter to show the detailed thermal and flow profile of an InSb Czochralski melt. This will include examining the effects of the crystal/crucible rotation and the buoyancy, in an attempt to describe a fundamental flow structure.

The second objective is to compare the numerical results with the asymptotic results, in order to validate the coupled boundary layer model developed in Chapter 4. The motivation for doing so is to couple the solidification model from Chapter 2 with the asymptotic flow model to obtain an overall quasi-steady process model.

6.1 Overview

A difficulty arises since the Finite Element calculation needs to be performed at a higher Prandtl number than in actual InSb melts, in order for the solver to converge.

This is unfortunate since the crucible boundary layer model assumes a Prandtl number much less than unity. For this reason, the comparison between the numeric and asymptotic results is not expected to be highly accurate, but at least an idea of the structure can be elucidated. Since the actual physical values cannot be modelled, the Pr number has been slightly increased, and the Bo number slightly reduced, as indicated in Table 6.1, which lists the simulation and actual process parameters. The same problem has been encountered with Si melts, which are also low Prandtl number fluids. The more recent work by Kakimoto [75] attempts to deal with low Prandtl number melts but only considers the "small crucible"case. The only other option is to assume the flow is turbulent but we do not believe this is the case. We intend to validate the asymptotic model at these idealized parameters and hope that the assumptions hold at the actual process values.

symbol	actual value	simulation value	units
α	6.0 x 10^{-6}	6.0 x 10^{-6}	m^2/s
ν	3.3 x 10^{-7}	2.7 x 10^{-6}	m^2/s
β	1 x 10^{-4}	1 x 10^{-4}	1/K
$\hat{R}_c$	0.075 - 0.10	0.05	m
$\hat{R}_x$	0.04 - 0.05	0.04	m
$\hat{\omega}_c$	0 - 10	5	RPM
$\hat{\omega}_x$	0 - (-10)	-5	RPM
$\Delta\hat{T}$	$10 - 20^*$	10	K
$Pr/Bo^{1/2}$	$5 \times 10^{-5} - 1 \times 10^{-4}$	2.5×10^{-3}	
$1/Bo^{1/2}$	$9 \times 10^{-4} - 2 \times 10^{-3}$	5.0×10^{-3}	
	$* =$ estimated		

Table 6.1: Parameters used in FE calculation of crucible flow

The other simplification the reader should be aware of is that the melt-crystal interface is assumed perfectly flat. This will have a small effect on the flow near the crystal, but should not be significant to the bulk of the crucible flow. As mentioned

earlier, we are mainly interested in the large scale flow patterns that will form.

6.2 FE Simulation Results I: The Effect of Buoyancy and Rotation

The first step in understanding the Czochralski melt fluid mechanics is to isolate the buoyancy from the crucible/crystal rotation, and then show how these effects interact. Simulations have been performed with the melt flow field dominated by either: buoyancy (little or no rotation), crystal rotation, crucible rotation, or are approximately balanced, as shown in Table 6.2. A relatively large crystal $R_x = 0.8$ was used with a full crucible to display more extreme conditions. The effects of the fluid height and crystal size are discussed in §7.2. Each variable $(u_r, u_\theta, u_z, T, P)$ is presented separately on its own page to highlight the changes in the flow field.

relative rotation	$\hat{\omega}_x$ (RPM)	$\hat{\omega}_c$ (RPM)
a) low crystal, low crucible	-0.5	0.5
b) high crystal, low crucible	-5.0	0.5
c) low crystal, high crucible	-0.5	5.0
d) high crystal, high crucible	-5.0	5.0
e) none - buoyant flow	0.0	0.0
f) very high crystal, very high crucible	-10.0	10.0

Table 6.2: Simulation parameters for melt with Pr = 0.5

The asymptotic model will also be used to calculate the crucible/crystal heat flux and torque. A numerical comparison between the asymptotic and numerical values will be presented in §6.3.

6.2.1 Structure of Crucible Flow

Figures 6.1 - 6.6 show the different flow structures that occur in a Czochralski melt. It is interesting to note when the crystal and crucible rotation rates are approximately balanced, as shown in Figures 6.1(a), 6.1(d) 6.3(a),6.3(d), a single convection cell forms. If the crystal or crucible rotation is dominant, as shown in Figures 6.1(b), 6.1(c), 6.3(b), 6.3(c), the flow separates at the crucible wall and a double convection cell forms. The axial velocity in these crystal or crucible rotation dominated flows, becomes positive at $r = 0$. This is important because towards the end of the growth process the crystal radius becomes large and the melt height decreases, so the crystal rotation can dominate the flow. Hence, it is a realistic possibility for the flow field to change from a single convection cell to a double convection cell. Figures 6.1(f) & 6.3(f) show a flow pattern that has a deformed cell but still in the form of a single convection cell.

The rotation of the crystal and crucible have the effect of throwing fluid away from the center at $r = 0$. The result is a warmer region at the center of the crucible $r = 0$, shown for high crucible rotation in Figure 6.5(c), and a more pronounced effect for high crystal rotation shown in Figure 6.5(b). The surprising feature is when the crystal and crucible rotations are similar the effects seem to cancel each other out in the thermal profile, shown in Figures 6.5(a) & 6.5(d).

The purpose of Figures 6.1(e) - 6.6(e) is to show a flow field that is purely driven by buoyancy. Since these figures very closely resemble the plots for the low crucible, low crystal rotation 6.1(a) - 6.6(a), it is clear that simulation number 1 is representative of a buoyancy dominated flow.

The effects of the crystal and crucible rotation can be summarized as follows. If the crystal and crucible rotation are similar in magnitude, a single convection cell will develop. If either dominates the flow field, the flow pattern undergoes a dramatic

6.2.2 Radial Velocity (u_r) Profiles

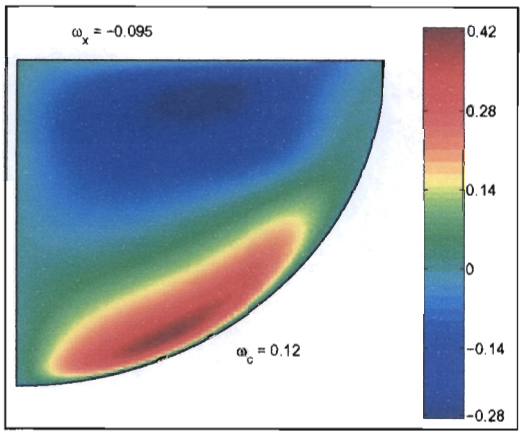

(a) Low ω_x, low ω_c

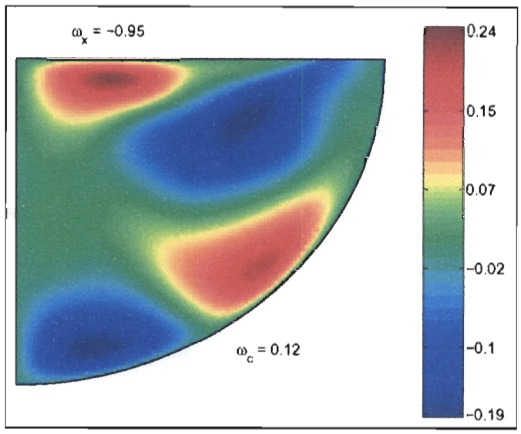

(b) High ω_x, low ω_c

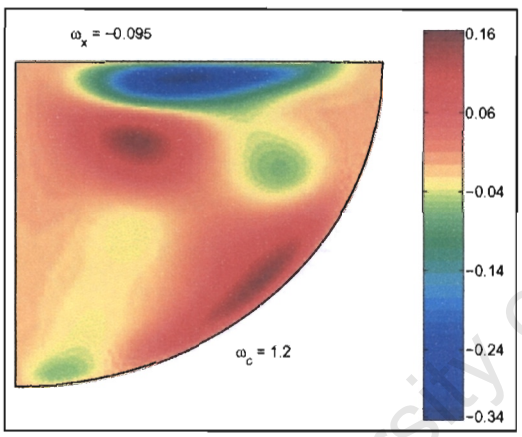

(c) Low ω_x, high ω_c

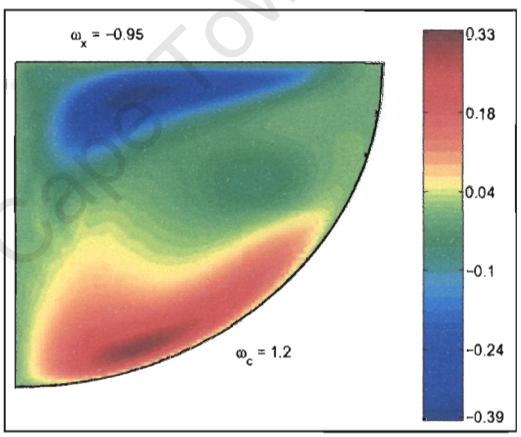

(d) High ω_x, high ω_c

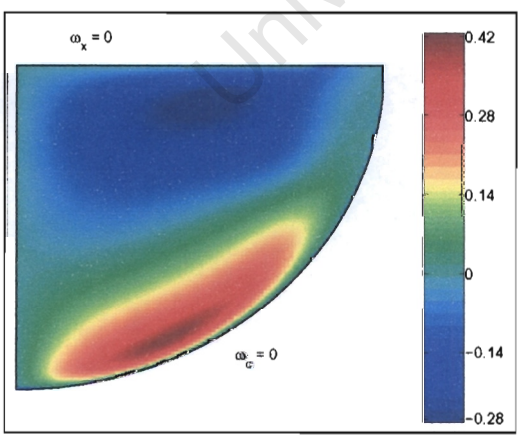

(e) Buoyant flow

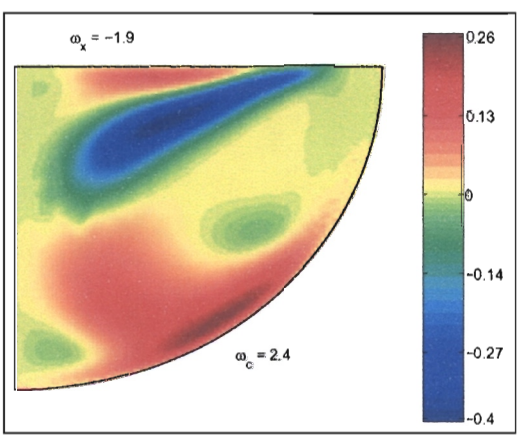

(f) Very high ω_x, very high ω_c

Figure 6.1: Simulated radial velocity profiles

6.2.3 Azimuthal Velocity (u_θ) Profiles

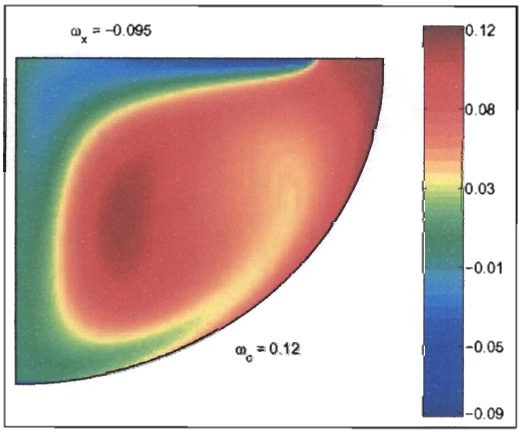

(a) Low ω_x, low ω_c

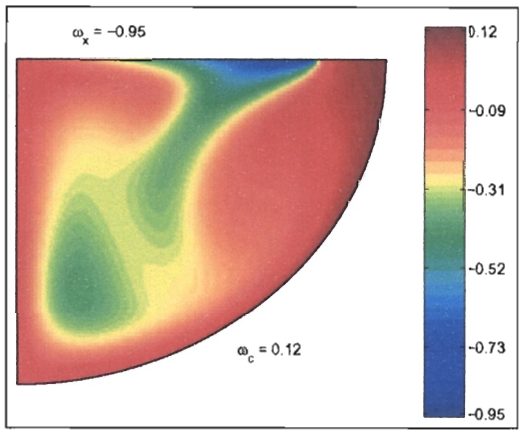

(b) High ω_x, low ω_c

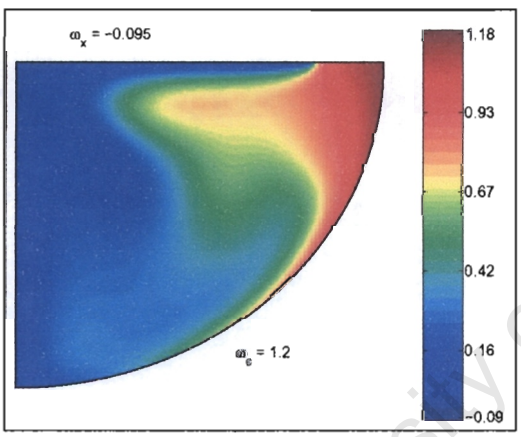

(c) Low ω_x, high ω_c

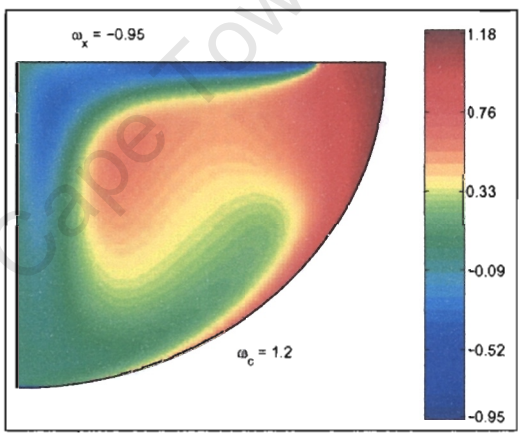

(d) High ω_x, high ω_c

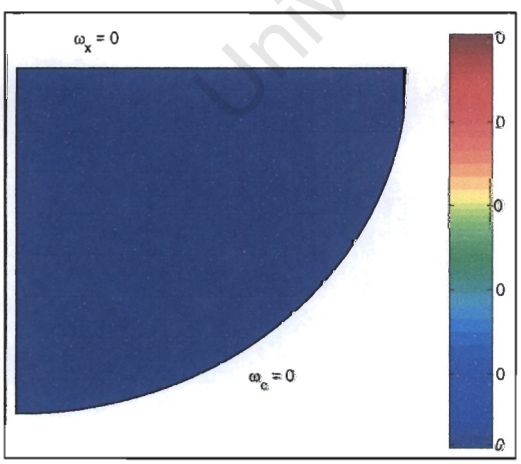

(e) Buoyant flow

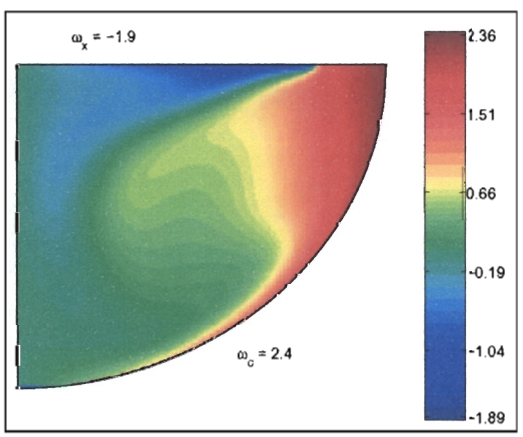

(f) Very high ω_x, very high ω_c

Figure 6.2: Simulated azimuthal velocity profiles

6.2.4 Axial Velocity (u_z) Profiles

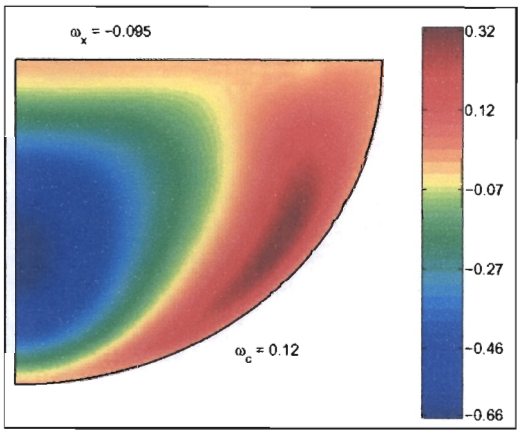

(a) Low ω_x, low ω_c

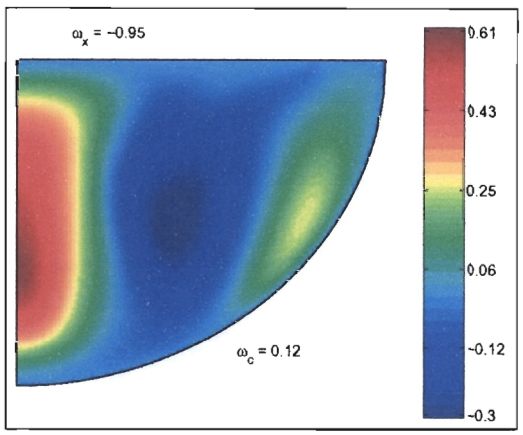

(b) High ω_x, low ω_c

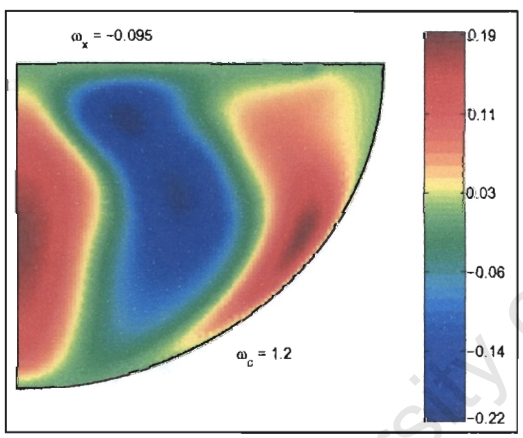

(c) Low ω_x, high ω_c

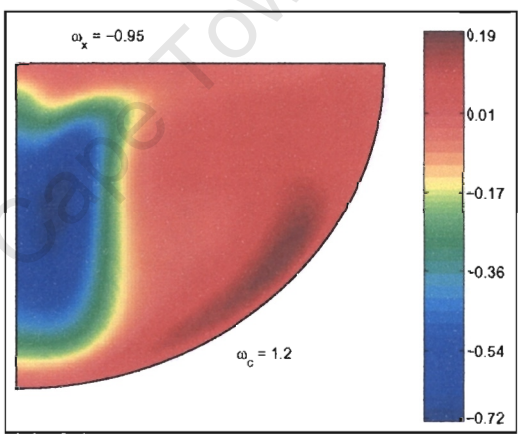

(d) High ω_x, high ω_c

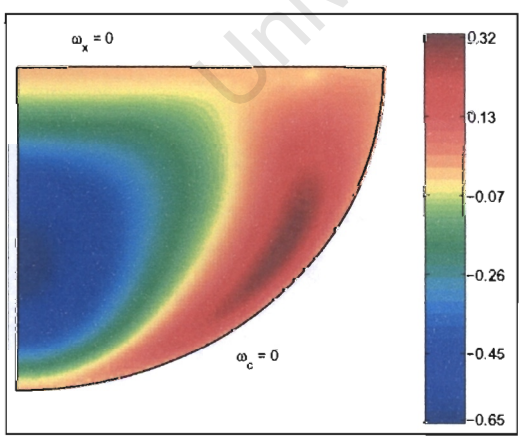

(e) Buoyant flow

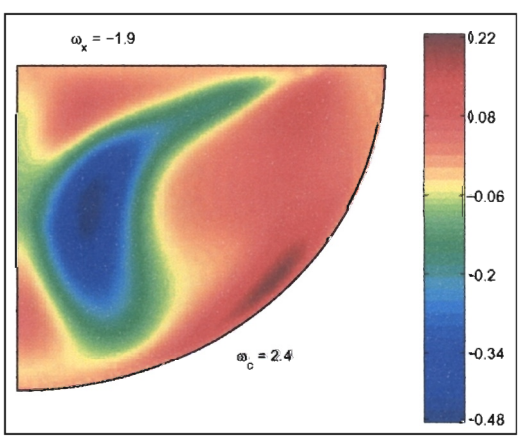

(f) Very high ω_x, very high ω_c

Figure 6.3: Simulated axial velocity profiles

6.2.5 Velocity Vectors (r, z)

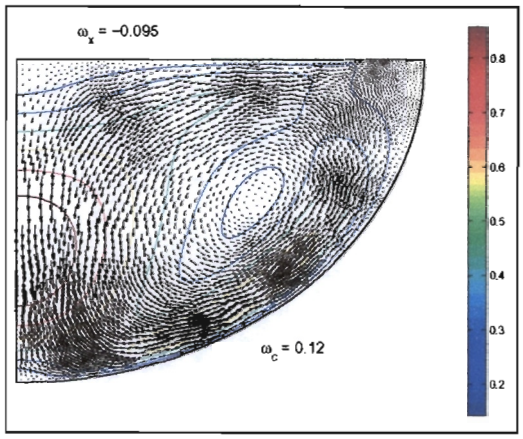

(a) Low ω_x, low ω_c

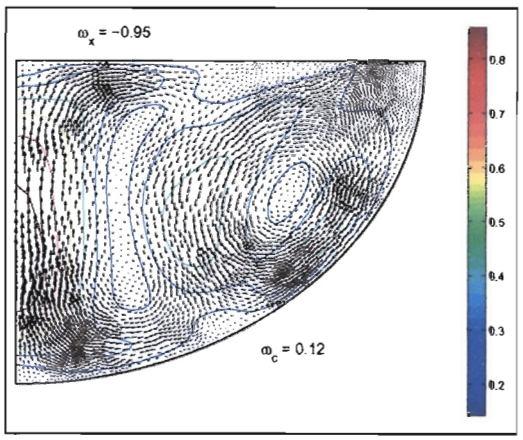

(b) High ω_x, low ω_c

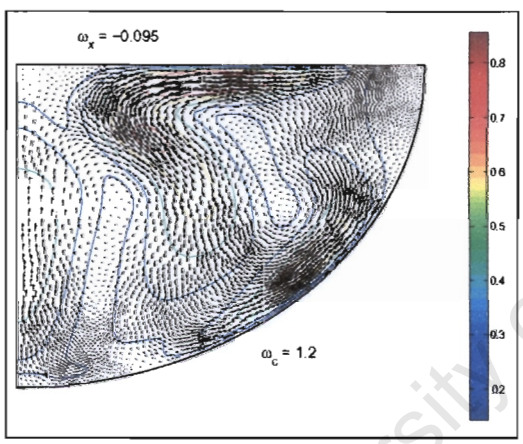

(c) Low ω_x, high ω_c

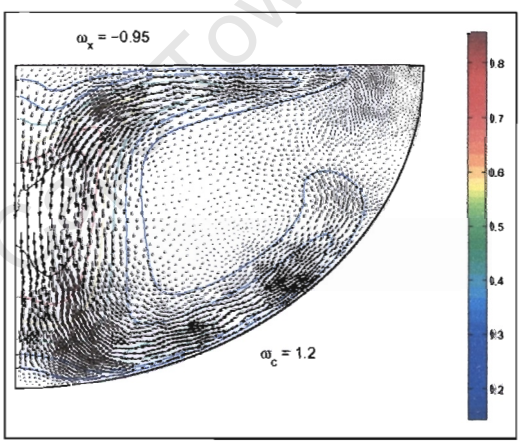

(d) High ω_x, high ω_c

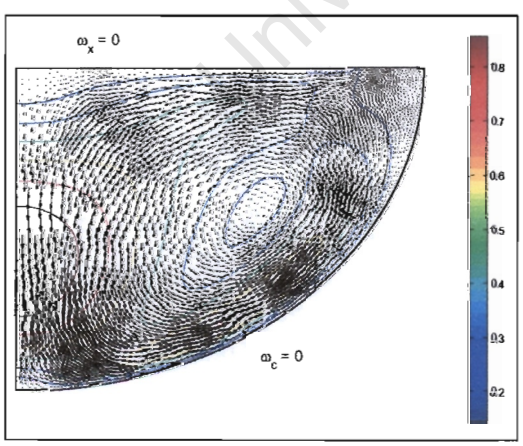

(e) Buoyant flow

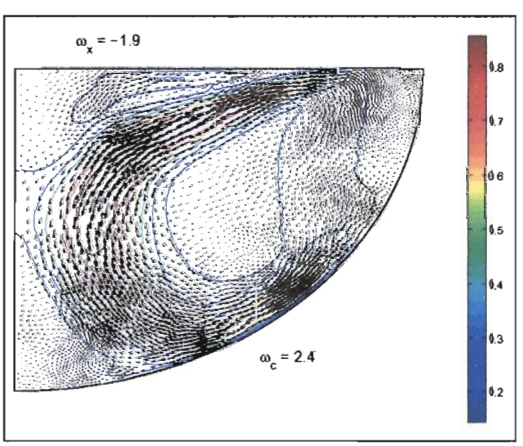

(f) Very high ω_x, very high ω_c

Figure 6.4: Simulated velocity fields (r, z)

6.2.6 Temperature (T) Profiles

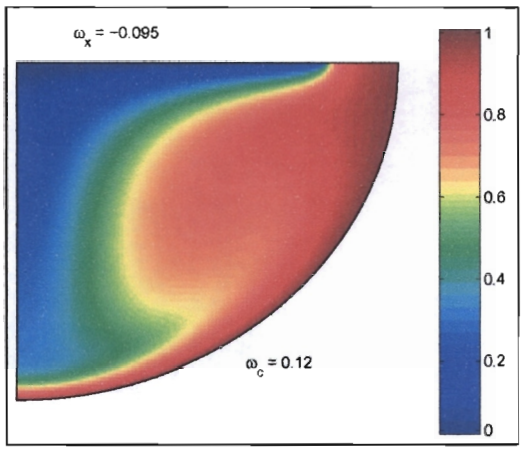

(a) Low ω_x, low ω_c

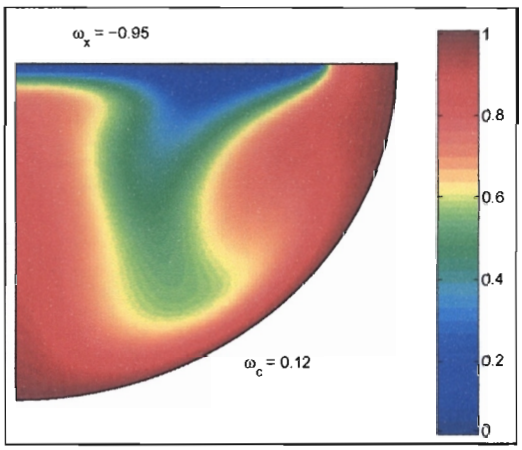

(b) High ω_x, low ω_c

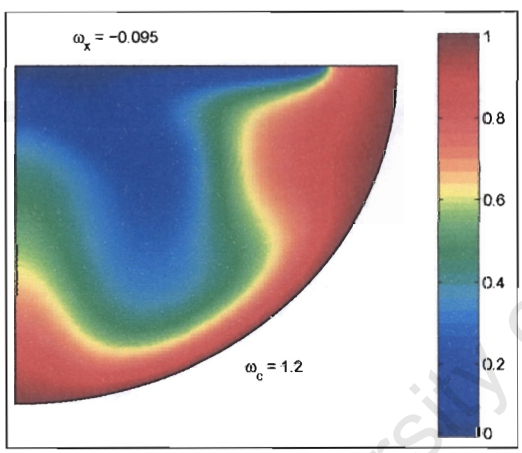

(c) Low ω_x, high ω_c

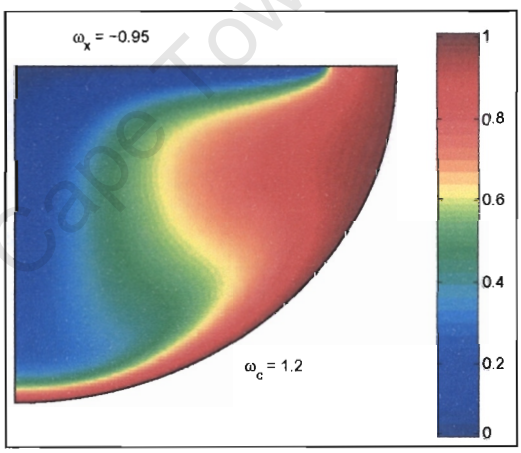

(d) High ω_x, high ω_c

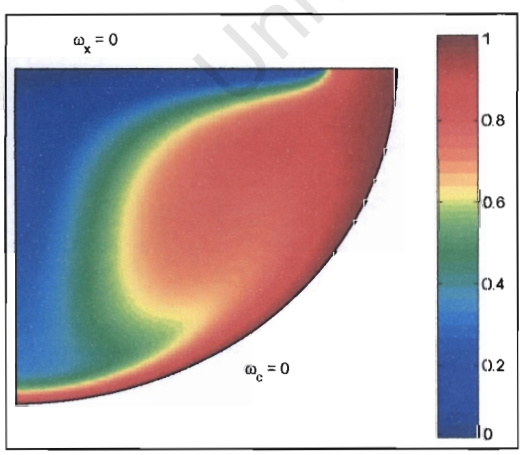

(e) Buoyant flow

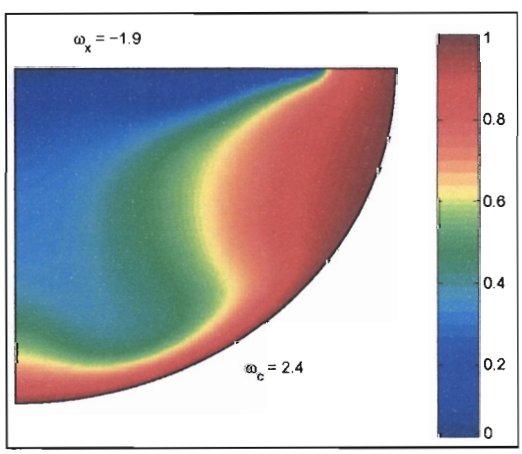

(f) Very high ω_x, very high ω_c

Figure 6.5: Simulated temperature fields

6.2.7 Pressure (P) Profiles

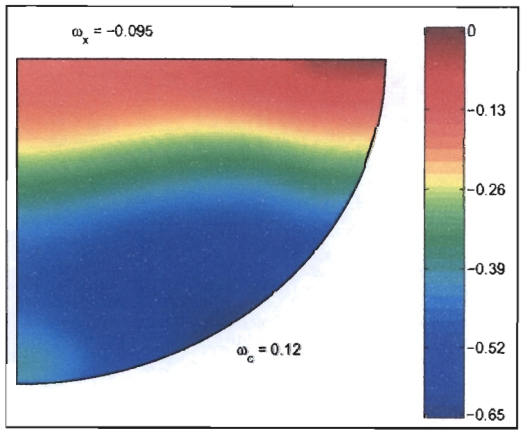

(a) Low ω_x, low ω_c

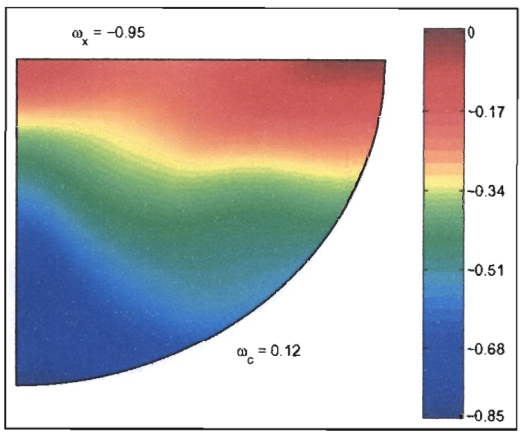

(b) High ω_x, low ω_c

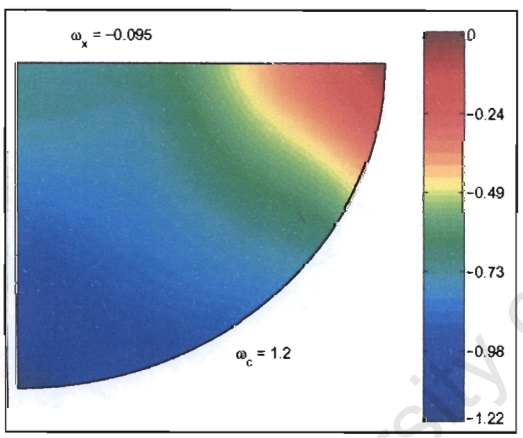

(c) Low ω_x, high ω_c

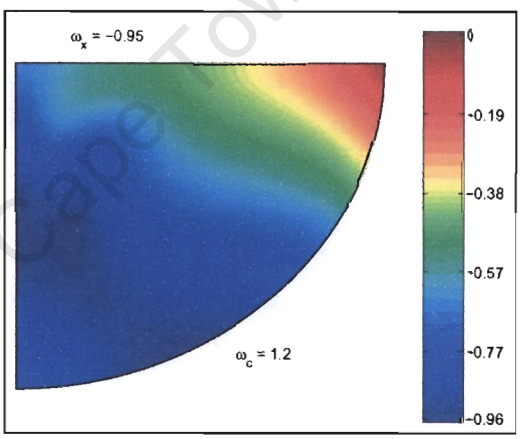

(d) High ω_x, high ω_c

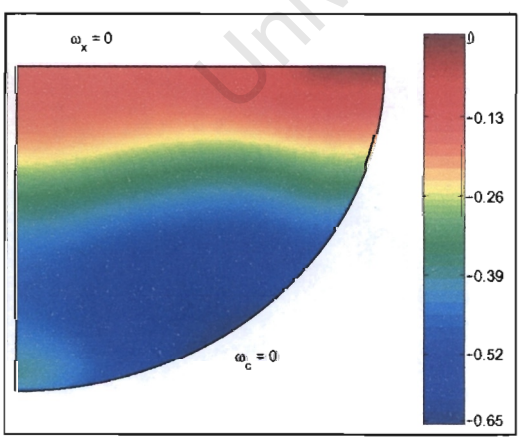

(e) Buoyant flow

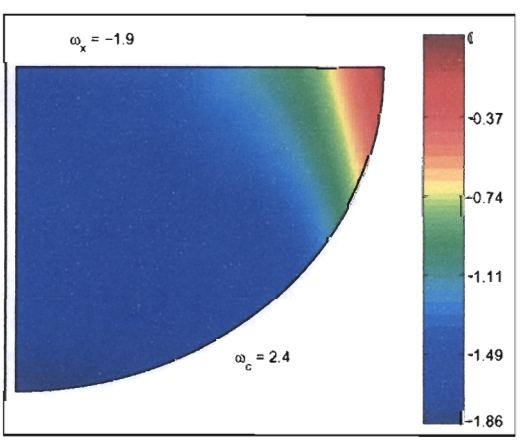

(f) Very high ω_x, very high ω_c

Figure 6.6: Simulated pressure fields

change into a double convective cell. The effect on the temperature gradients will be discussed in §6.4.

It is also likely that other structures can form, particularly with more rotation and buoyancy present. With more rotation, as shown in Figures 6.1(f) - 6.6(f), a more deformed structure, dissimilar to the other flow fields appears. It would be beneficial to ensure that the fluid motion is kept constant and fluctuations do not occur.

6.3 Coupled Boundary Layer Model Validation

In this section, we scrutinize the coupled boundary layer model assumptions. First, a qualitative comparison is performed with the velocity and temperature plots in §6.2, then a numerical comparison is performed on the temperature and azimuthal velocity gradients. These values are chosen for comparison because they are the basis for closure in the coupled boundary layer model.

It should also be noted the scale analysis performed in Chapter 3 indicated the balance between buoyancy and inertia was valid provided the Prandtl number was much less than unity. The asymptotic model is being compared at $\mathrm{Pr} = 0.5$, instead of $\mathrm{Pr} = 0.05$, in order for the finite element solver to converge. Better agreement is expected in the crucible boundary layer for smaller Prandtl numbers.

The assumptions for the coupled boundary layer model can be summarized as follows:

1. There exists a thermal boundary layer at the crucible wall
2. There is a momentum boundary layer underneath the crystal
3. The exists an isothermal core with rotational velocity field close to solid body rotation ($\omega_m r$)

A thermal boundary layer can loosely be defined as a rapid change in temperature occurring in a relatively small layer of fluid. For axisymmetric geometry, the volume

of fluid increases with the cube of the radius. This means that temperature gradients at the crucible wall may be smaller, as compared to the center of the crucible, simply because the volume of fluid is significantly less. Bearing this in mind, a boundary layer clearly exists at the crucible wall as shown in the thermal profiles in Figures 6.5. The discrepancy between the asymptotic and finite element solution is due to the complexity of the shape of the boundary layer. The asymptotic model is based on a buoyant boundary layer in a semi-infinite domain. The crucible has enclosed convection and thus produces a more complex shaped thermal boundary layer, not smooth and uniform. The other problem is the asymptotic model does not capture the shifting in the thermal profile as shown in 6.5(b) & 6.5(c), when the crystal or crucible rotation is relatively large.

The momentum boundary layer under the crystal is clearly visible in Figures 6.2(a)-6.2(d), 6.2(f). There is a definite abrupt transition in the angular velocity that decays very rapidly. Figures 6.2(a), 6.2(b), 6.2(d) display large core regions, where the rotation is relatively constant. The crucible rotation dominated case (Figure 6.2(c)) does not appear to have a core region. The core assumption for isothermal temperature is clearly an inaccurate idealization, as shown in Figures 6.5(a) - 6.5(f). The pressure fields appear to be close to varying linearly with temperature and quadratic with radius in Figures 6.6(c), 6.6(d), 6.6(f) where the crucible rotation is high. This is important because the core equations are linked to the crucible boundary layer, through pressure equation (4.7). The pressure fields in 6.6(a) & 6.6(b) appear to vary only linearly in z, since there is not sufficient rotation to give the solid body rotation form.

Next we wish to compare the numerical values of the gradients at the crystal and crucible, since they govern the closure for the coupled boundary layer model. We are also particularly interested in the temperature gradient at the crystal since this value is needed for the solidification calculation in Chapter 7. Table 6.3 shows the corresponding simulation numbers. Figure 6.7 shows the value of the temperature derivatives integrated over the surface of the crystal and crucible.

label	$\hat{\omega}_x$ (RPM)	$\hat{\omega}_c$ (RPM)
Simulation 1	-0.5	0.5
Simulation 2	-5.0	0.5
Simulation 3	-0.5	5.0
Simulation 4	-5.0	5.0

Table 6.3: Simulation labels for flux / torque comparison

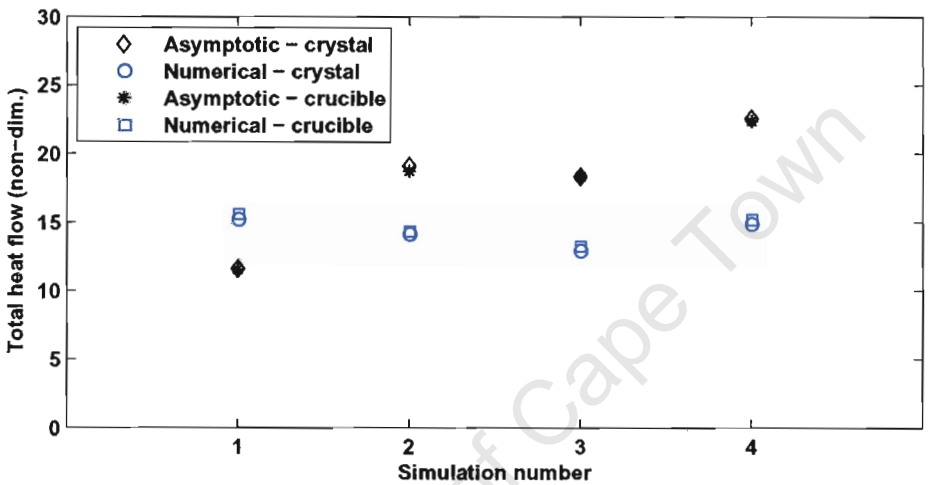

Figure 6.7: Integrated temperature gradients at crystal and crucible

The major observation that can made from Figure 6.7 is the rotation has little effect on the heat transfer. A limitation of the coupled boundary layer model may be the dependence of the temperature gradient on the boundary layer thickness underneath the crystal. This will have the effect of exaggerating the change in heat flux due to rotation. However, an estimate of the heat flow is possible, that differs by approximately 20-30%.

There is better agreement between the azimuthal velocity gradients, as shown in Figure 6.8, although the coupled boundary layer model seems to be over-sensitive to the rotational effects. Clearly the azimuthal gradients depend only on the relative difference in rotation, not either the crystal or crucible individually.

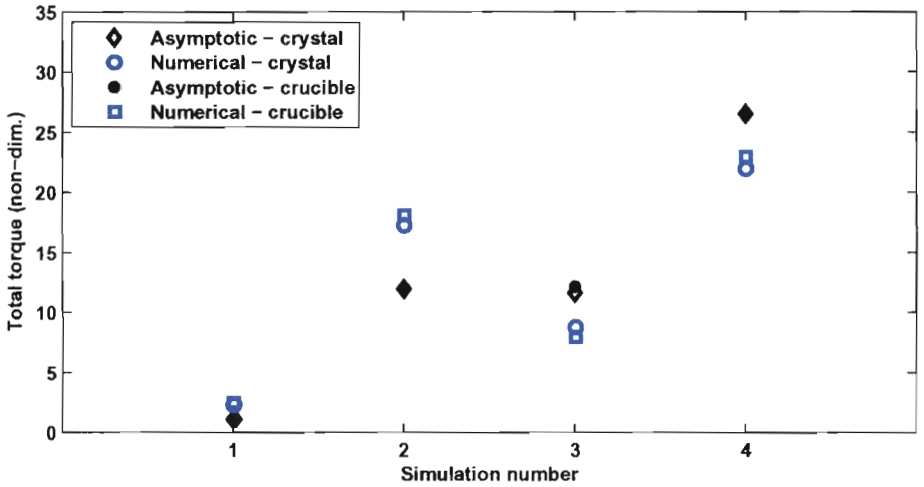

Figure 6.8: Integrated azimuthal velocity gradients at crystal and crucible

In order to determine the source of these discrepancies, it is necessary to examine the individual gradient profiles. Note for the crystal, the temperature is assumed to be 1D, so the derivative is constant across the crystal. Figure 6.9 shows that the 1D approximation does not accurately represent the temperature gradient, although there is slight agreement in an averaged sense. This is definitely a region where the asymptotic approximation is not entirely valid and could be improved.

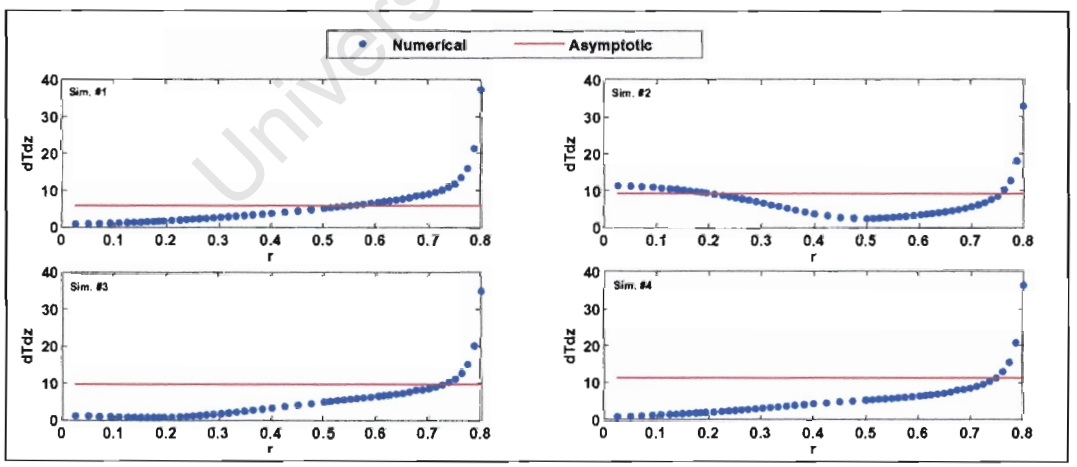

Figure 6.9: Temperature gradients at crystal

Similar poor agreement occurs between the coupled boundary layer model and the

Finite Element solution at the crucible wall, shown in Figure 6.10. The problem here is the asymptotic model does not capture the complexity of the changing crucible flow field. The melt is recirculating cooler parts that impact the center of the crucible and cause more heat transfer to occur towards $r = 0$. The coupled boundary layer model assumes buoyancy adjacent to a non-interacting rotating core. Clearly the recirculating fluid cell contributes to the discrepancy between the two models. One positive feature is the integrated derivatives are approximately the same. Even though the gradient is shifted toward the center in the FE solution, the asymptotic approximation can be used to estimate the total heat flow.

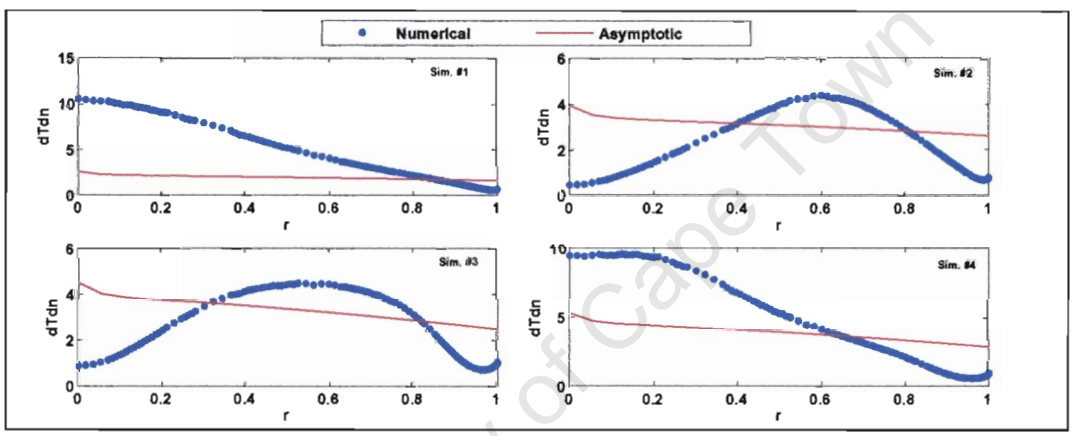

Figure 6.10: Temperature gradients at crucible

The azimuthal velocity gradients show stronger agreement, presented in Figures 6.11 and 6.12. The exception is when the crucible rotation is low, as shown in Figure 6.12, and poor agreement is obtained. This is likely due to the fact that buoyancy is dominating the flow and the asymptotic approximation does not capture this contribution. The only other shortcoming is the asymptotic model predicts a linear change in the azimuthal gradient at the crystal, which is unlikely since the gradients increase substantially as shown in Figure 6.11.

The coupled boundary layer model provides an approximate estimate of the heat flux and torque values that agree somewhat with the Finite Element solution. The main problem appears to be that the crucible flow is very complex, particularly for

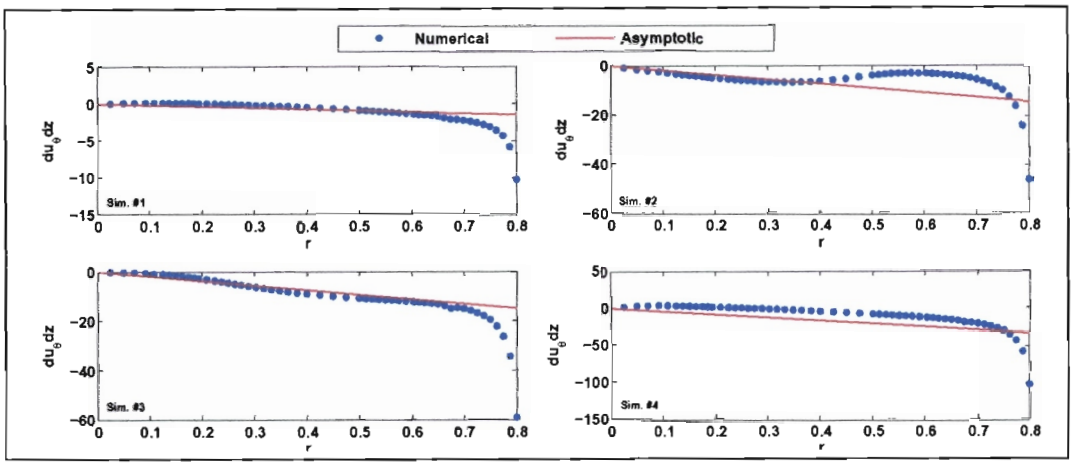

Figure 6.11: Azimuthal velocity gradients at crystal

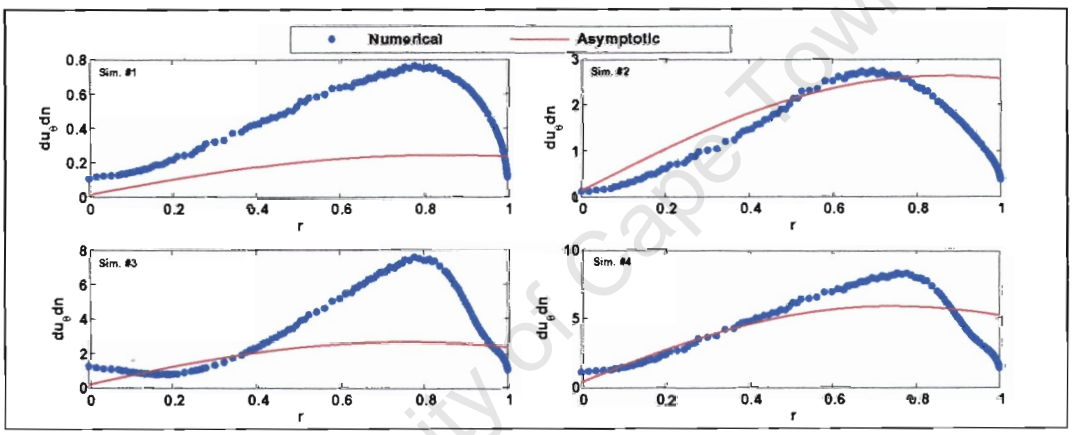

Figure 6.12: Azimuthal velocity gradients at crucible

the thermal profile, but the integrated values provide reasonable estimates of these quantities.

The other inaccurate assumption appears to be with the crystal boundary layer. The crystal boundary layer definitely dictates the angular velocity profiles, where strong agreement was obtained. However, the crystal boundary layer seems to have little effect on the thermal behaviour of the melt.

6.4 Temperature Gradient at the Crystal

The feature of the melt that governs solidification is the temperature gradient at the crystal. Figure 6.13 shows the temperature gradients at the crystal/melt interface, and the variation with rotation.

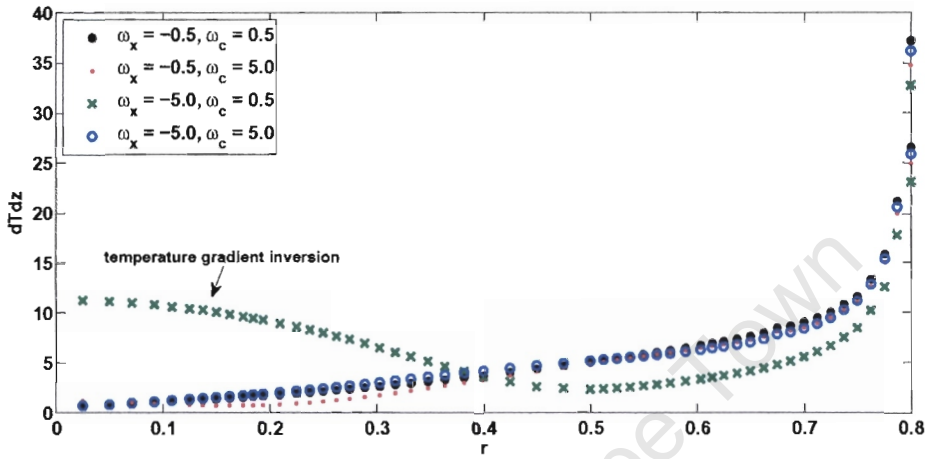

Figure 6.13: Temperature gradient profiles at crystal

When producing crystals, an invariant flow and thermal profile are desirable. All the profiles of the temperature gradient are similar, except for the crystal rotation dominated case, where a drastic change of shape occurs. In actual processing, this would likely cause the crystal/melt interface to change shape. Figure 6.13 shows an inversion of the heat concentration to the crystal. The typical profile is linearly increasing and peaking towards the outer edge of the crystal. As the crystal rotation is increased more of the heat transfer occurs towards the center of the crystal.

The other concern comes from the large increase at the edge of the crystal. This is likely due to the hot jet coming off the crucible and coming into contact with the cooler crystal. As indicated earlier, the heat transfer should be kept uniform and the profiles in Figure 6.13 show large increases at the end of the crystal. It appears much of the heat enters the crystal in the outer 10% of the radius, which could also lead to large radial stresses.

6.5 Summary

In this chapter we showed the complexity of Czochralski melts at a slightly higher Prandtl number. In the Finite Element results in §6.2, part of the assumed structure was present from the coupled boundary layer model. We also saw that if the crystal and crucible rotation are approximately balanced, then a single convection cell forms. If either rotation dominates the flow, then a double convection cell appears.

The integrated temperature gradients at the crystal were within approximately 20%, although we expect the results to agree better at lower Prandtl numbers. This difference is likely due to the fact that the temperature is assumed 1D in the asymptotic flow underneath the crystal and the detailed temperature profile is not captured. It is still necessary to verify the temperature gradient for different crystal radii to ensure the asymptotic melt heat flux is relatively accurate.

One important effect was shown in §6.4 where excessive crystal rotation dramatically changed the shape of the temperature gradient at the crystal. If the temperature gradient profile changes shape, the heat transfer to the crystal also changes, which can give rise to radial thermal stresses and produce crystals with defects.

In the next chapter, we couple the asymptotic melt calculation to the solidification model from Chapter 2. The result is a fully coupled model that can be used to show how the melt parameters affect solidification.

Chapter 7

Quasi-Steady Crystal Growth with Varying Parameters

The focus of this chapter is the variation of process parameters throughout the crystal growth period. First, the coupled boundary layer model will be validated with the Finite Element solution using different crystal radii and melt heights. It is necessary to ensure the asymptotic melt heat fluxes remain accurate as these variables change.

We will then proceed by combining the solidification model from Chapter 2 with the coupled boundary layer calculation from Chapter 4. This will allow the melt heat flux to be determined at the actual melt Prandtl number ($\mathrm{Pr} = 0.055$) and operating conditions, shown in the left hand column of Table 6.1. Our pseudo-steady analysis is a novel calculation that allows the Czochralski crystal solidification dynamics to depend on actual melt conditions.

7.1 Overview

As discussed in §2.3, the coupling between the crystal and melt only occurs through mass transfer. As the crystal grows and the melt shrinks, both domains are changing with time. For this reason, the governing equations in both regions may be solved separately using the appropriate crystal radius and melt height.

We will present Finite Element solutions for the melt flow field using different crystal radii and the corresponding melt heights. The numerical temperature gradients at the crystal will be compared with the asymptotic values to verify if our coupled boundary layer model remains valid under various crystal radius / melt height combinations.

We will then rearrange the Stefan condition (2.21) to be able to calculate other process parameters. In particular, we will examine the variation of the radial growth rate, crucible wall temperature and surrounding gas temperature in the following manner:

1. Specify the radial crystal growth rate and keep the gas temperature constant to obtain a realistic crucible wall temperature profile

2. Again specify the radial crystal growth rate, but modify the crucible wall temperature profile from (1), to obtain the surrounding gas temperature variation

3. Finally, we will specify a modified crucible wall temperature profile and modify the ambient gas temperature profile from (2) to calculate the resulting crystal shape

We do not consider the effect of transient crystal or crucible rotation because, as shown in §6.3, changes in rotation did not significantly affect the heat transfer to the crystal. This type of calculation could easily be performed if desired, but we will focus on varying the chamber conditions.

7.2 FE Simulation Results II: Variable Crystal Radius and Melt Height

We begin by examining the crucible fluid mechanics and heat transfer via the Finite Element solution with the radii and melt heights presented in Table 7.1.

crystal radius (R_x)	crucible height (H)
0.16	1.0
0.29	0.96
0.36	0.91
0.43	0.82
0.50	0.70
0.57	0.51

Table 7.1: Crystal radius and melt heights for QS simulations

Figures 7.1 through 7.6 contain the results of the Finite Element simulations.

The crucible and crystal rotation rates are constant, at 5.0 RPM and -5.0 RPM respectively, but the azimuthal velocity depends on where the fluid is in contact with each boundary. To clarify, the values from the azimuthal velocity plots (Figure 7.2) will be summarized. The maximum azimuthal velocity due to the crucible rotation occurs at the start of the process with a value of 0.95, at the top of the crucible shown in 7.2(a). At the end of the process, shown in 7.2(f), the maximum azimuthal velocity value has dropped to a value of only 0.82, approximately a 15% decrease. The majority of this decrease occurs between $R_x = 0.50$ and $R_x = 0.57$ when the values drop from 0.90 to 0.82. The change in azimuthal velocity due to crystal rotation is more significant, starting at -0.19 (in Figure 7.2(a)) and ending at -0.67 (in Figure 7.2(f)), over three times the amount. This indicates a very significant increase in the azimuthal velocity component from the crystal and a decreasing component from the crucible. The consequence of the crystal rotation

7.2.1 Radial Velocity (u_r) Profiles

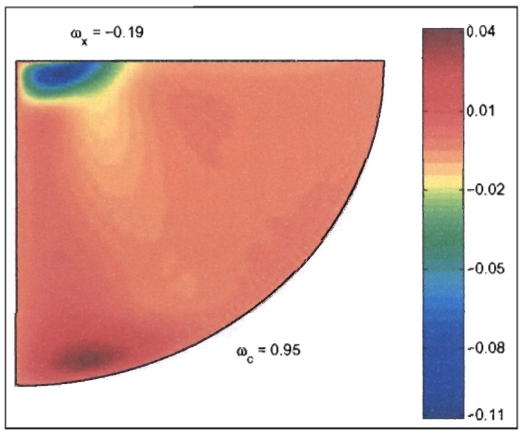

(a) $R_x = 0.16$, $H = 1.0$

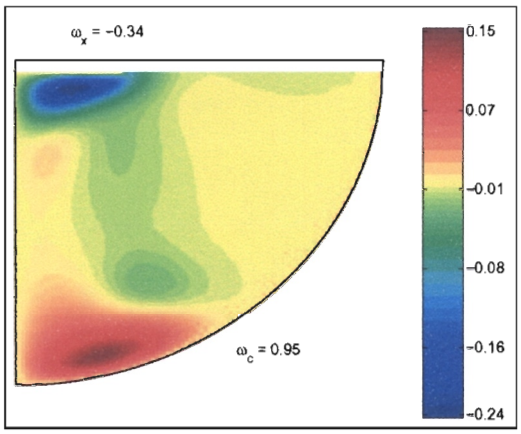

(b) $R_x = 0.29$, $H = 0.96$

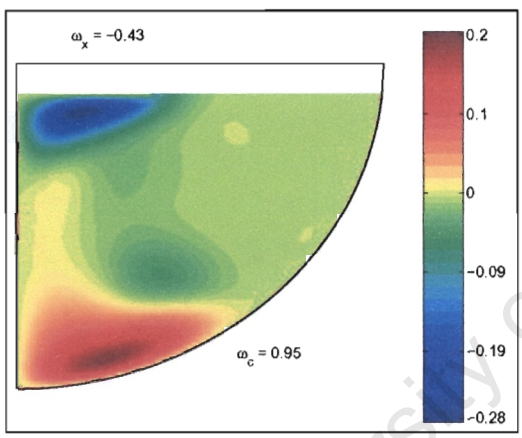

(c) $R_x = 0.36$, $H = 0.91$

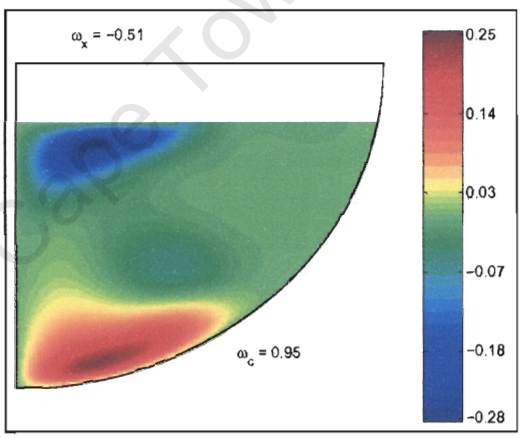

(d) $R_x = 0.43$, $H = 0.82$

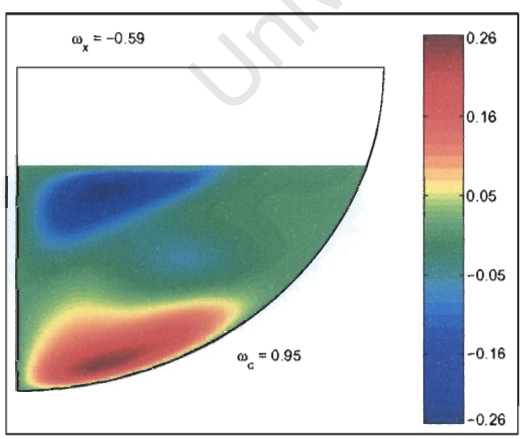

(e) $R_x = 0.50$, $H = 0.70$

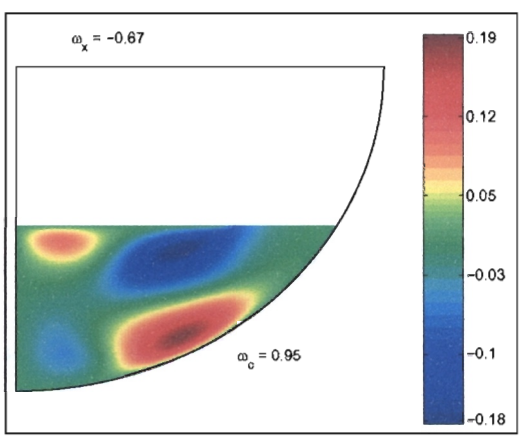

(f) $R_x = 0.57$, $H = 0.51$

Figure 7.1: Radial velocity profiles

7.2.2 Azimuthal Velocity (u_θ) Profiles

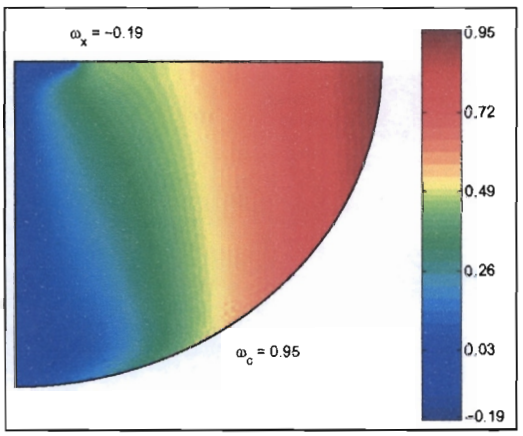

(a) $R_x = 0.16$, $H = 1.0$

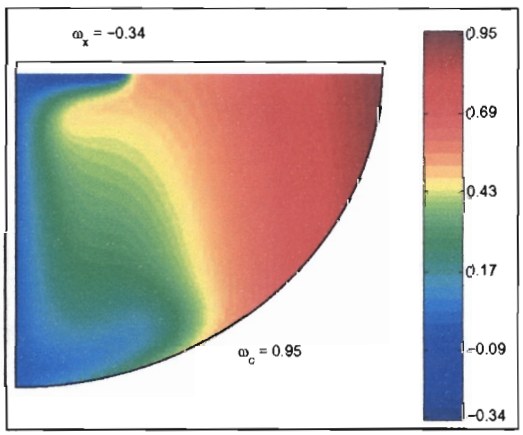

(b) $R_x = 0.29$, $H = 0.96$

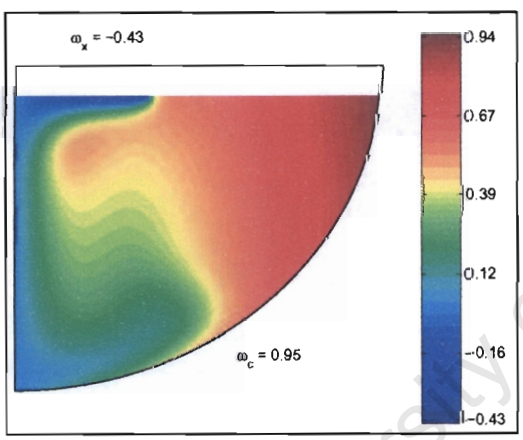

(c) $R_x = 0.36$, $H = 0.91$

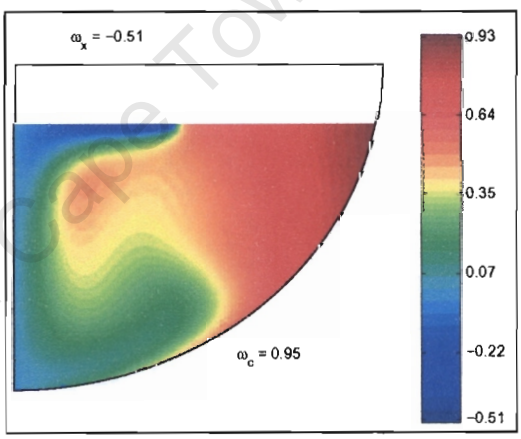

(d) $R_x = 0.43$, $H = 0.82$

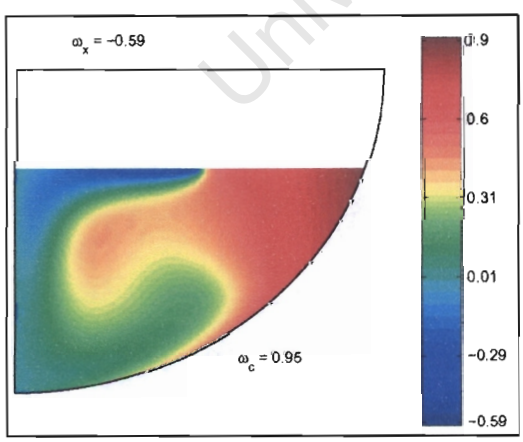

(e) $R_x = 0.50$, $H = 0.70$

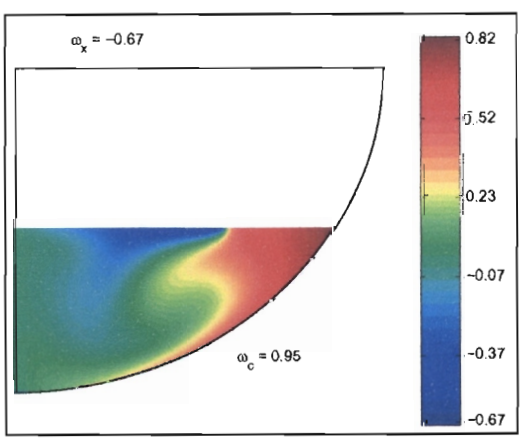

(f) $R_x = 0.57$, $H = 0.51$

Figure 7.2: Azimuthal velocity profiles

7.2.3 Axial Velocity (u_z) Profiles

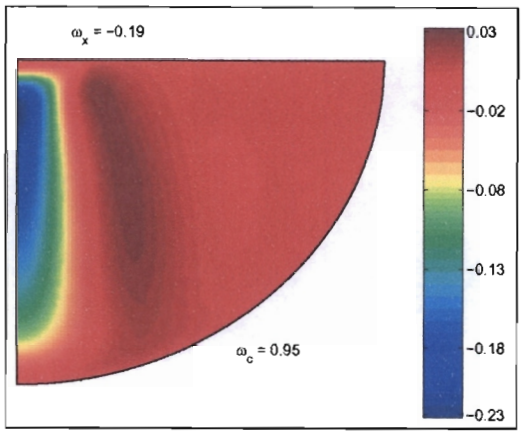

(a) $R_x = 0.16$, $H = 1.0$

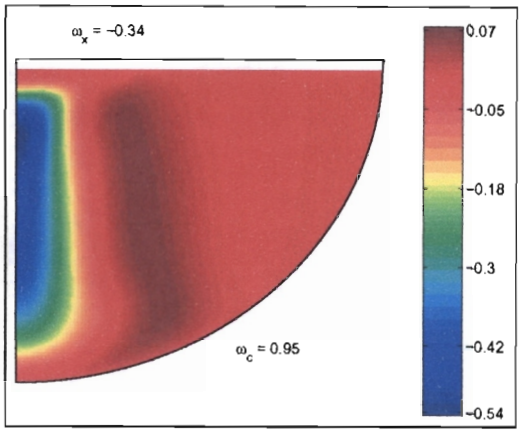

(b) $R_x = 0.29$, $H = 0.96$

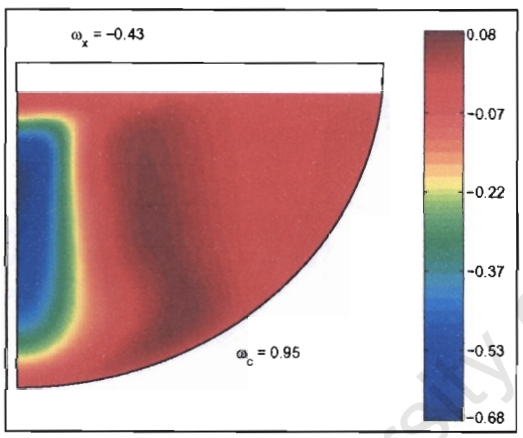

(c) $R_x = 0.36$, $H = 0.91$

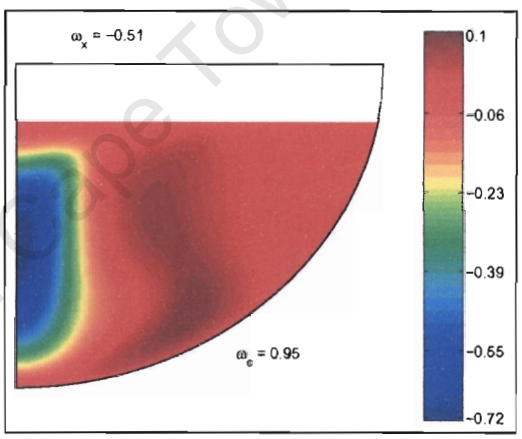

(d) $R_x = 0.43$, $H = 0.82$

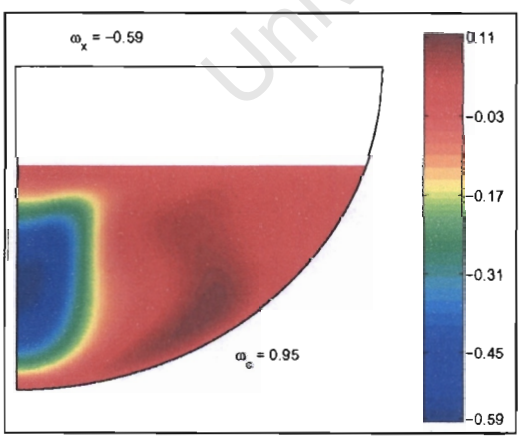

(e) $R_x = 0.50$, $H = 0.70$

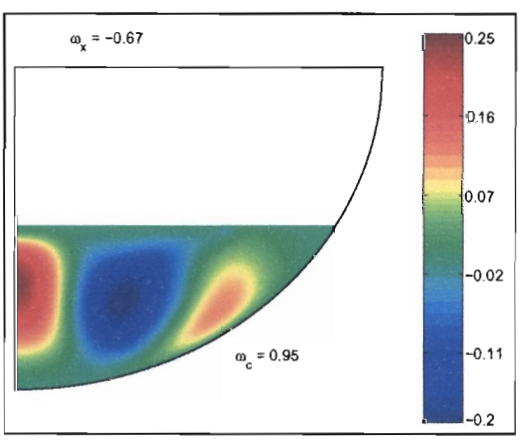

(f) $R_x = 0.57$, $H = 0.51$

Figure 7.3: Axial velocity profiles

7.2.4 Velocity Vectors (r, z)

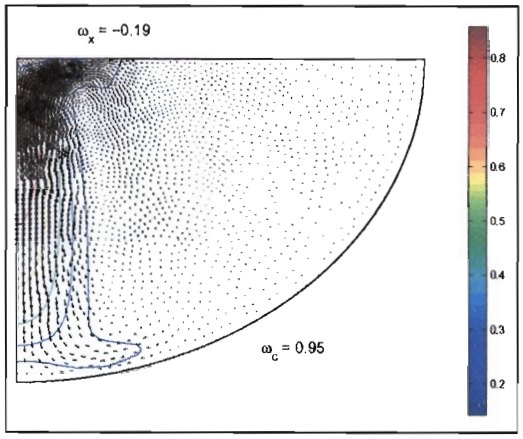

(a) $R_x = 0.16$, $H = 1.0$

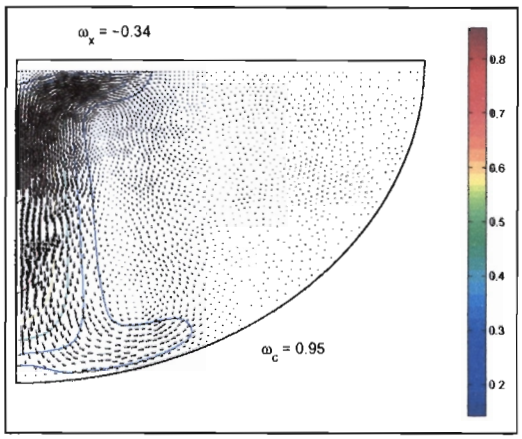

(b) $R_x = 0.29$, $H = 0.96$

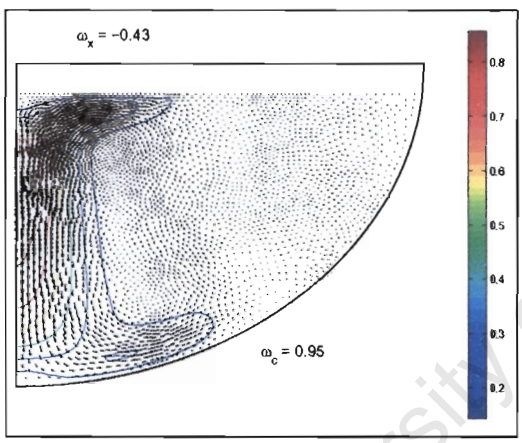

(c) $R_x = 0.36$, $H = 0.91$

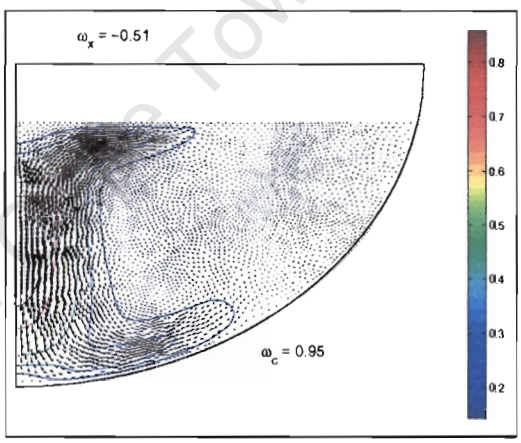

(d) $R_x = 0.43$, $H = 0.82$

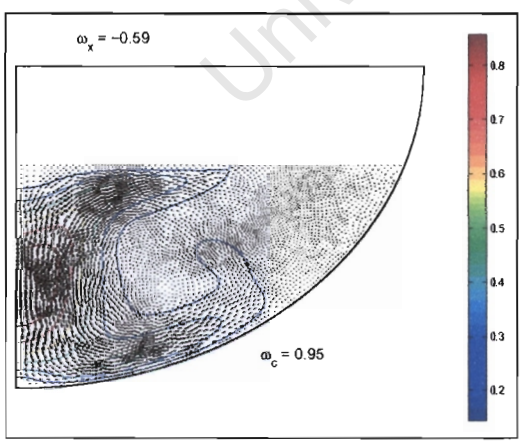

(e) $R_x = 0.50$, $H = 0.70$

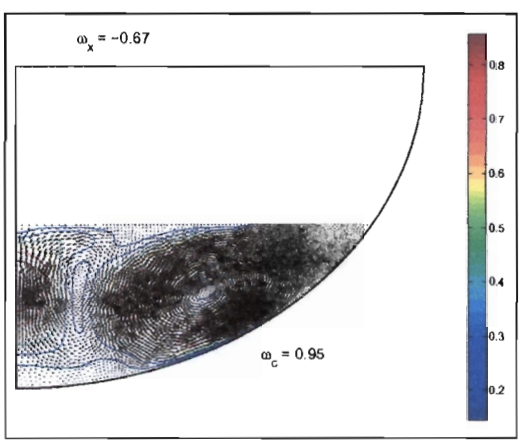

(f) $R_x = 0.57$, $H = 0.51$

Figure 7.4: Velocity vectors in (r, z)

7.2.5 Temperature (T) Profiles)

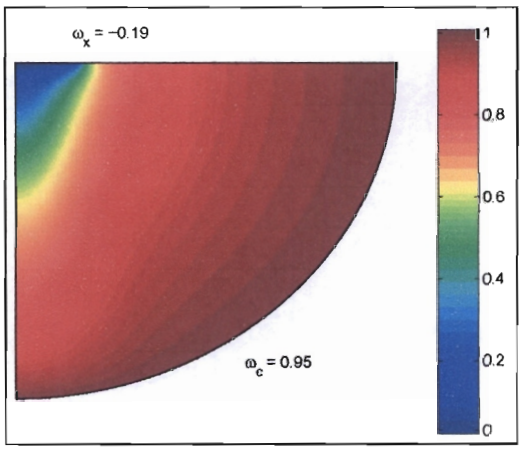

(a) $R_x = 0.16$, $H = 1.0$

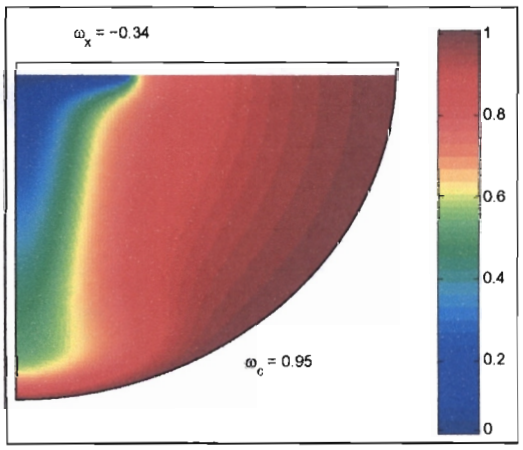

(b) $R_x = 0.29$, $H = 0.96$

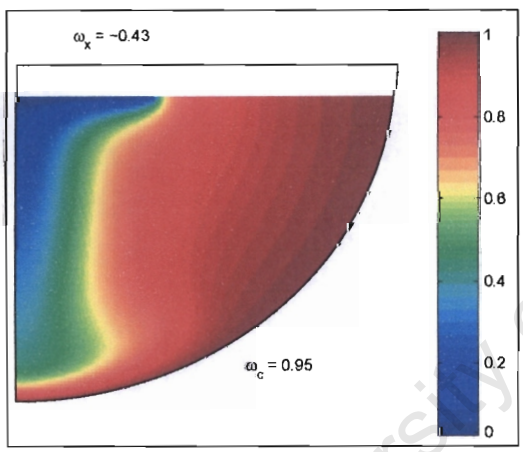

(c) $R_x = 0.36$, $H = 0.91$

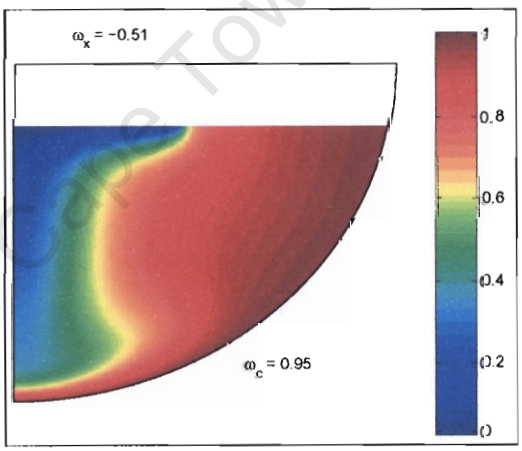

(d) $R_x = 0.43$, $H = 0.82$

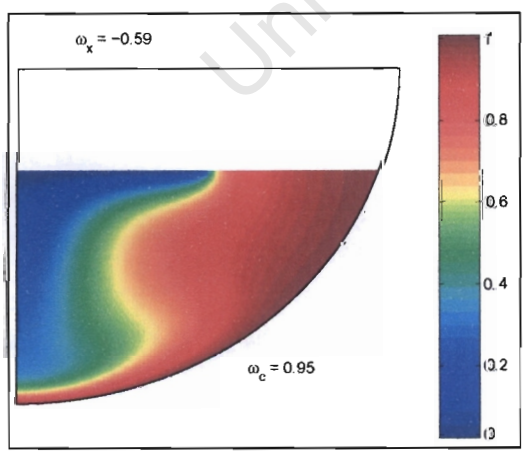

(e) $R_x = 0.50$, $H = 0.70$

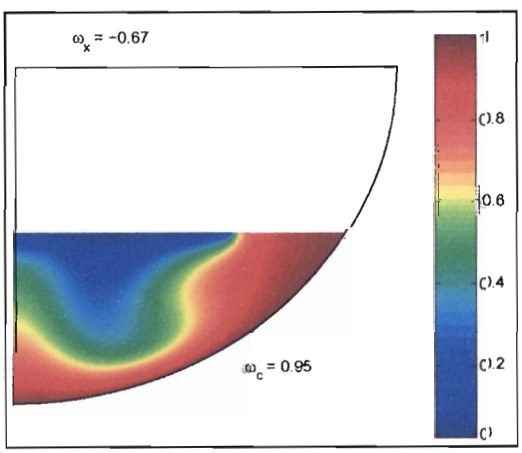

(f) $R_x = 0.57$, $H = 0.51$

Figure 7.5: Temperature profiles

7.2.6 Pressure (P) Profiles

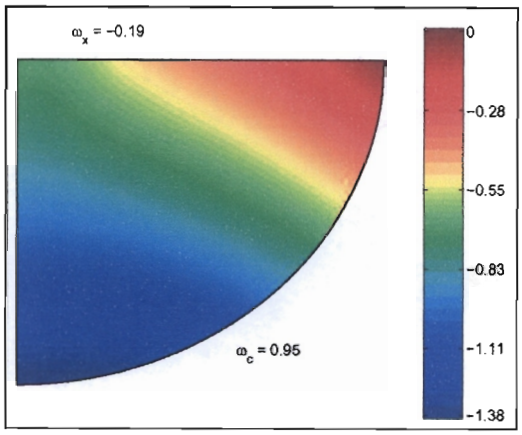

(a) $R_x = 0.16$, $H = 1.0$

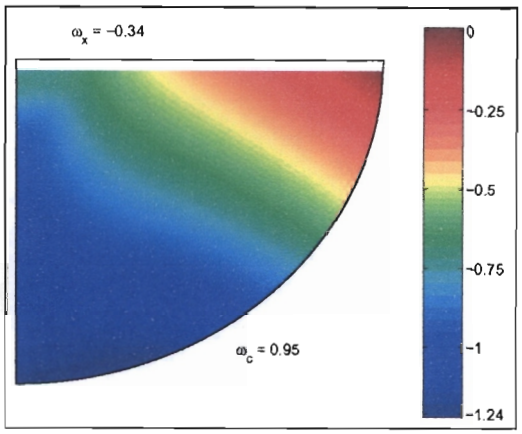

(b) $R_x = 0.29$, $H = 0.96$

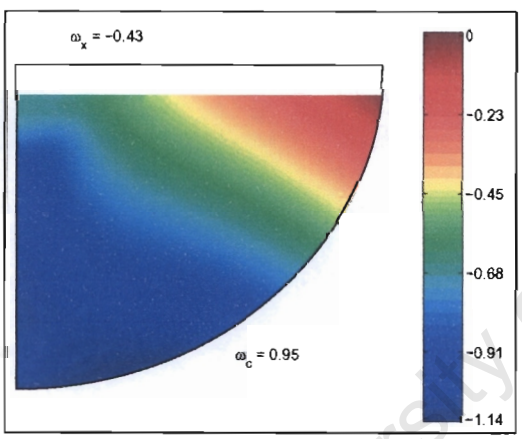

(c) $R_x = 0.36$, $H = 0.91$

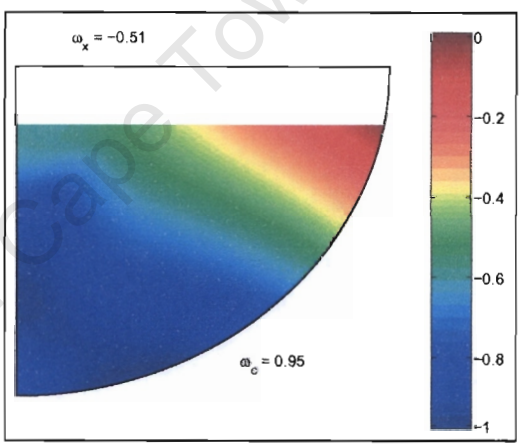

(d) $R_x = 0.43$, $H = 0.82$

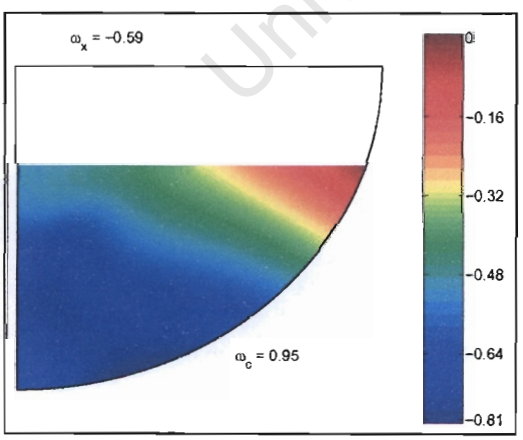

(e) $R_x = 0.50$, $H = 0.70$

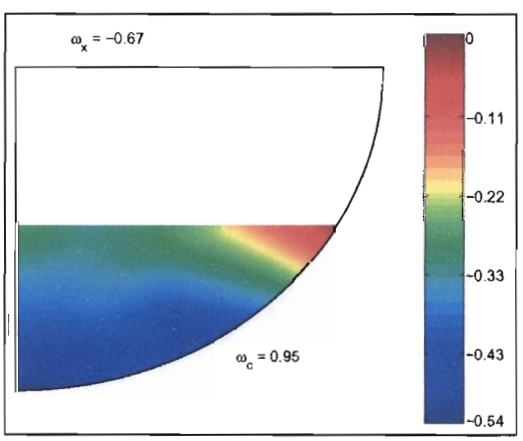

(f) $R_x = 0.57$, $H = 0.51$

Figure 7.6: Pressure profiles

becoming more dominant is shown in the changing flow pattern visible in Figures 7.1(f), 7.3(f) and 7.4(f). This change in flow field pattern could have a negative on the crystal solidification, since a warm jet forms at the center of the crucible at $r = 0$. This is similar to the temperature gradient inversion described in §6.4.

Figure 7.5 shows how the crystal area plays an important role in shaping the melt thermal field. A constant temperature difference between the crystal and crucible is imposed ($\hat{T}_c - \hat{T}_f = 10$ K). Notice at the beginning of the growth process in Figure 7.5(a), there is little sign of a boundary layer and the vertical velocity is almost insignificant, seen in 7.3(a). Once the crystal area is slightly larger, the boundary layer region becomes visible but again only in a small region under the crystal, as in Figures 7.3(b) and 7.5(b). This trend continues since the majority of buoyant motion occurs directly beneath the crystal in $0 < r < R_x$ as shown in Figures 7.1, 7.3, 7.4. A stagnant region tends to develop in the crucible at $r > R_x$. A possible improvement for the coupled boundary layer model would be to truncate the crucible boundary layer domain to $[0, R_x]$ and integrate the equations to the position on the crucible corresponding to the crystal radius.

7.2.7 Temperature Gradient Comparison

Before coupling the solidification model with the coupled boundary layer model, the asymptotic melt heat fluxes to the crystal needs to be validated. Figure 7.7 shows the integrated temperature gradients for the asymptotic and Finite Element calculations. The asymptotic model consistently overestimates the heat flow to the crystal, but does capture the overall trend. Again, this is likely due to the fact that the Prandtl number has been increased to 0.5 for the Finite Element solver to converge.

If we assume that the asymptotic boundary layer model will provide reasonable estimates of the heat flux to the crystal, in particular at lower Prandtl numbers, it can then be coupled with the crystal solidification model from Chapter 2.

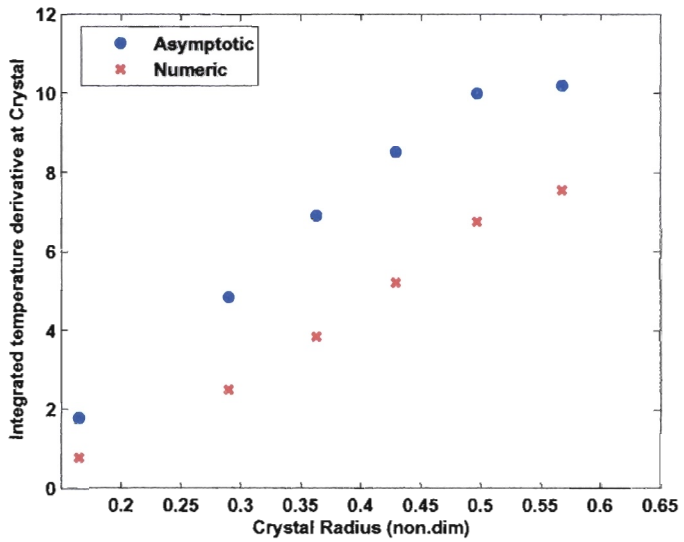

Figure 7.7: Integrated temperature gradients at crystal

7.3 Transient Crucible Wall Temperature

For all of the previous melt calculations the crucible wall temperature was assumed to be 10 K higher than the crystal melting temperature throughout the entire process, with no physical basis. In this section, we provide the radial crystal growth rate (from actual crystal data) as input for our solidification model, and calculate the crucible wall temperature.

Stefan condition (2.21) was rearranged for the melt heat flux to the crystal:

$$q_m = k_l \frac{\partial T}{\partial z} = \frac{\partial \chi}{\partial z} - \frac{S}{3}\left[\frac{da}{dt}\frac{2(a-s_0)}{ma} + \left(1 + \frac{\rho a^2}{\rho_m R_m^2}\right)\right], \tag{7.1}$$

and recall the temperatures are scaled by

$$T = \frac{\hat{T} - \hat{T}_f}{\hat{T}_c - \hat{T}_f}, \qquad \chi = \frac{\hat{\chi} - \hat{T}_f}{\hat{T}_f - \hat{T}_g}.$$

The melt heat flux is calculated using the radial growth rate data, presented in Figure 7.8, as input. $\partial\chi/\partial z$ is obtained by solving ODE (2.18) numerically.

The wall temperature $\hat{T}_c$ is iterated within the asymptotic flow model until the value of $(k_l\ \partial T/\partial z)$ matches the right hand side of (7.1). Note if the crystal shape

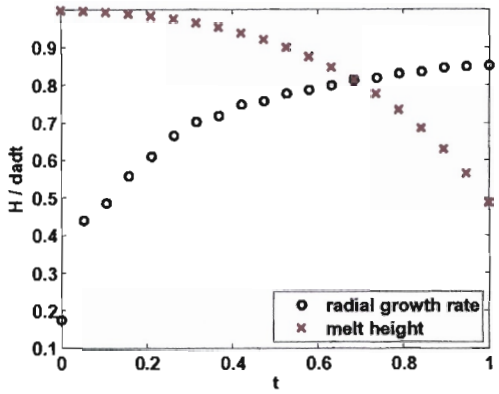

Figure 7.8: Supplied radial growth rates and melt heights

is specified, then the corresponding melt heights can be easily calculated and all the input data for the melt calculation is well defined. The resulting crucible wall temperature profile is presented in Figure 7.9.

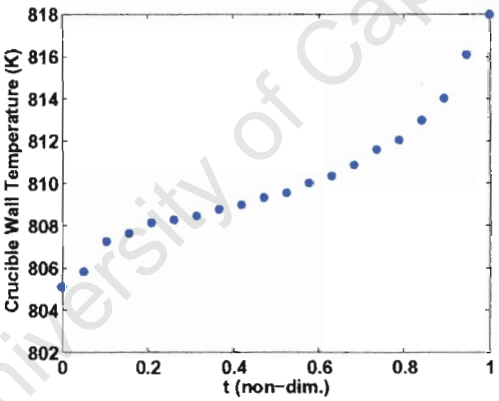

Figure 7.9: Calculated crucible wall temperature

The crucible wall temperature profile in Figure 7.9 has three sections. The wall temperature is initially low because little heat escapes through the small crystal. This is reasonable since we assume no heat is lost from the melt to the gas. As the crystal becomes larger, a steady increase occurs from approximately $t = 0.2$ until $t = 0.6$. Thereafter, the wall temperature increases sharply due to the dropping melt height that is significant around $t \sim 0.6$, shown in Figure 7.8.

Now that we have a realistic crucible wall temperature profile, we can vary it slightly and then determine the ambient gas temperature profile.

7.4 Transient Gas Temperature

One factor that is likely to change during the crystal growth period is the surrounding gas temperature, due to either the crystal surface area increasing or the chamber volume becoming larger as the seed chuck moves upwards. There may be other factors that lead to a non-constant gas temperature but it would be useful to include this variation into our solidification calculation.

Again, we rearrange Stefan condition (2.21), this time solving for the temperature gradient in the crystal:

$$\frac{\partial \chi}{\partial z} = q_m + \frac{S}{3}\left[\frac{da}{dt}\frac{2(a-s_0)}{ma} + \left(1 + \frac{\rho a^2}{\rho_m R_m^2}\right)\right] \tag{7.2}$$

We use the same radial growth rate from the asymptotic calculation as in Figure 7.8. However, the crucible temperature profile is imposed in a linear form slightly higher than the profile calculated in the previous section, shown in Figure 7.10.

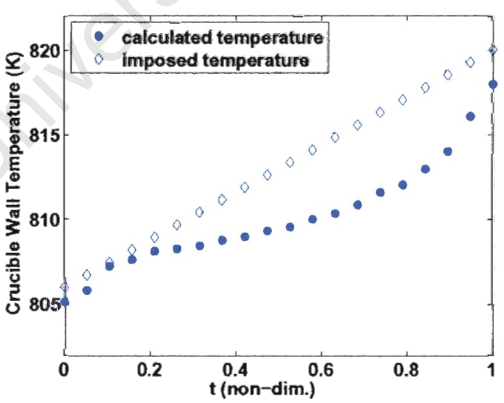

Figure 7.10: Calculated and imposed crucible wall temperature

The surrounding gas temperature can then be determined by iterating $(\hat{T}_g)$ until $\partial\chi/\partial z$ balances the right hand side of equation (7.2). The ambient gas temperature

variation is shown in Figure 7.11 for our specified input values. The estimated temperature is the value used in the solidification results in Chapter 2, which was assumed to be 648 K.

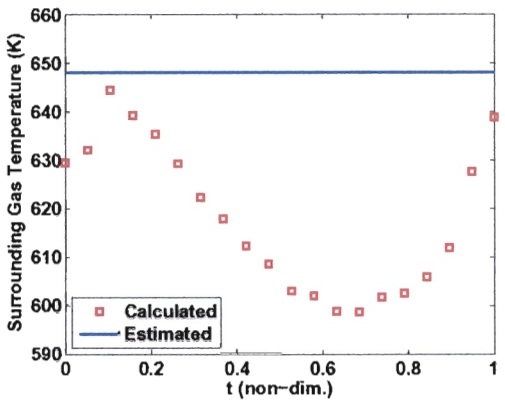

Figure 7.11: Surrounding gas temperature profile

The calculated gas temperature is essentially a scaled difference between the imposed and calculated crucible wall temperatures from Figure 7.10. Since the radial crystal growth rate is specified, if more heat is added at the crucible by our imposed wall temperature profile, then more heat must be taken away by the surrounding gas at the crystal. It is reassuring to see the results appear consistent in terms of heat flow.

The final step will be to impose crucible wall and ambient gas temperature profiles, and to then calculate the resulting crystal shape.

7.5 Crystal Shape Prediction

One of the limitations of the solidification model developed in Chapter 2 is the constant (and estimated) melt heat flux. In this section, we wish to use the coupled boundary layer model from Chapter 4 to calculate the heat flux based on the melt dynamics and crucible parameters. It was shown in §7.2.7 that the asymptotic flow model overestimated the melt heat flux at a higher Prandtl number. We assume

we will obtain stronger agreement at Pr = 0.05 and proceed to model Czochralski crystal growth with our overall process model.

The algorithm for combining the solidification model from Chapter 2, to the coupled boundary layer model for the melt from Chapter 4, is summarized in Figure 7.12. First, a starting volume of melt is specified, which can be converted into a starting melt height. For simplicity, these calculations begin with a full hemi-spherical crucible of liquid InSb. Once initial values for the crystal radius and height have been specified the calculation can commence.

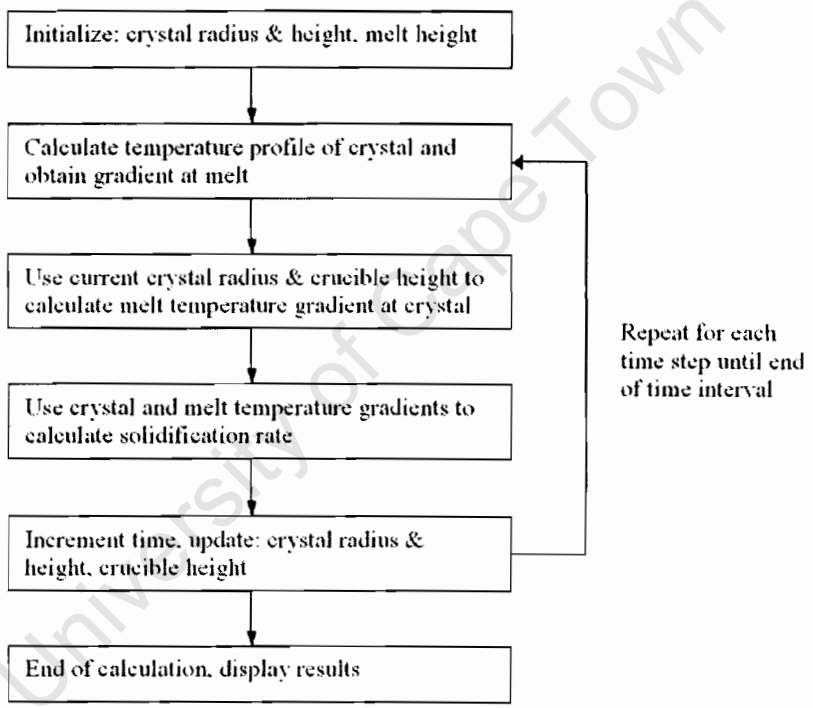

Figure 7.12: Summary of algorithm for coupled calculation

The temperature in the crystal is calculated by solving ODE (2.18) numerically and obtaining the gradient $\partial\chi/\partial z$ at $(z = b^-)$. The asymptotic melt equations (4.28)-(4.30) are then solved to predict the melt heat flux q_m at the other side of the crystal at $(z = b^+)$. Both gradients are used to determine the radial solidification rate of the crystal using the Stefan condition (2.21). The time interval is then incremented, and the crystal height is recalculated. The new mass of crystal that forms must

be deducted from the melt, resulting in an updated fluid height. The process is repeated until the time interval of interest is complete.

The first example we present uses the crucible wall temperature profile in Figure 7.9, with a constant gas temperature $\hat{T}_g = 150$K. The shape and temperature profile are presented in the form of a colour map in Figure 7.13 in time intervals of 0.25.

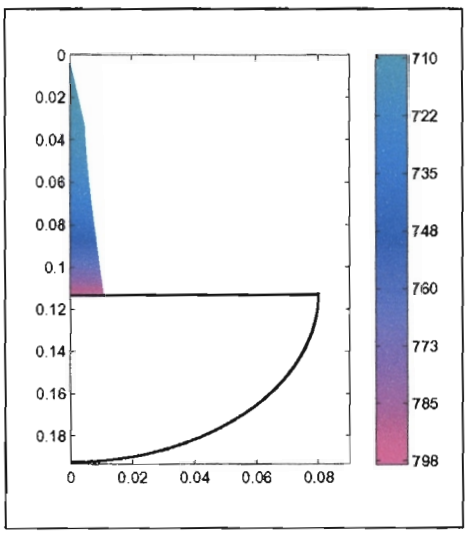

(a) coupled model: t = 0.25

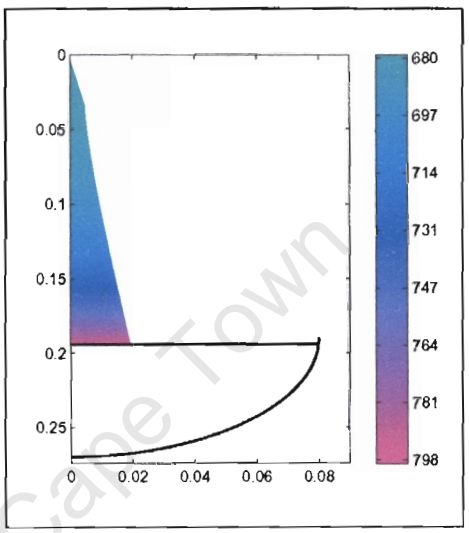

(b) coupled model: t = 0.50

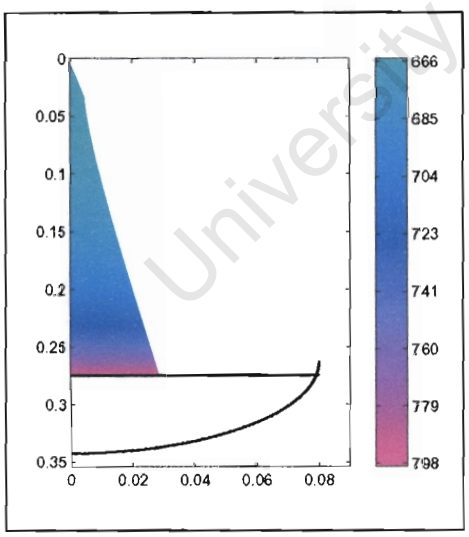

(c) coupled model: t = 0.75

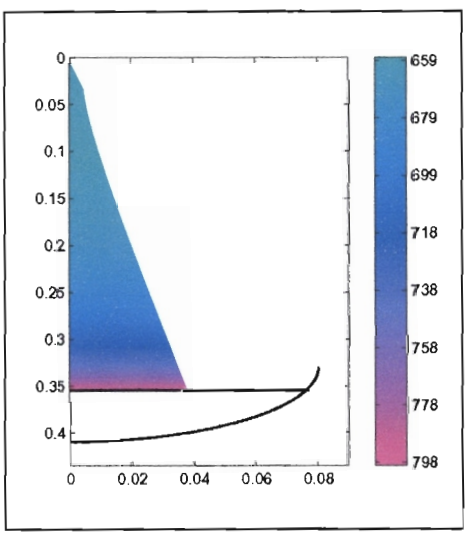

(d) coupled model: t = 1.0

Figure 7.13: Crystal calculations coupled with melt

The reason for choosing these values is the crystal profile should be the exact same

as in Figure 2.7 since this was the source of the radial growth rate in the previous two sections. In order to show the coupled calculation is consistent, we specify a crucible wall temperature profile and ambient gas temperature that will result in a known crystal shape.

Figures 7.13(a)-7.13(d) are snapshots of the crystal geometry and temperature as it is pulled out of the crucible. The shape is indeed the same as in Figure 2.7, which implies that the calculations are consistent. The main objective here is to show that crystal geometry and temperature can now be obtained with an approximation for the melt fluid mechanics.

We proceed by using a variable crucible wall and surrounding gas temperature profile to show how these effect the crystal shape. Here we wish to use hypothetical profiles that would ideally be based on experimental or laboratory results, and are shown in Figure 7.14, with the previous profiles from §7.4 and §7.5.

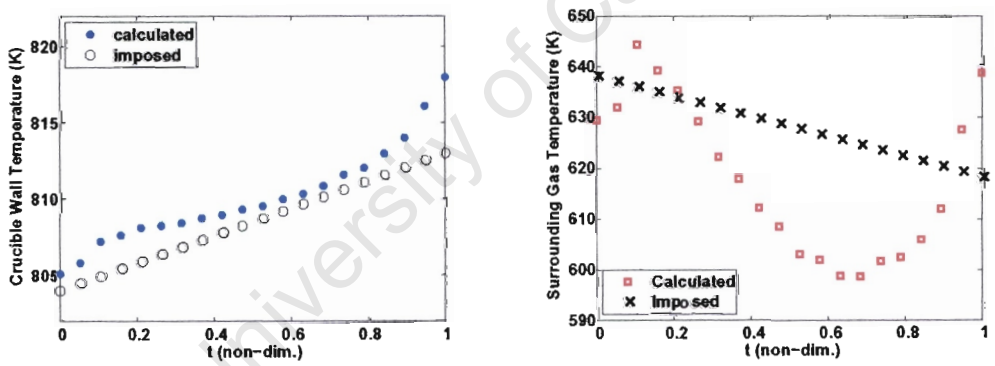

(a) Crucible wall temperature

(b) Surrounding gas

Figure 7.14: Imposed profiles for final simulations

The coupled boundary layer calculation was performed as described in Figure 7.12, with the imposed profiles from Figure 7.14. The imposed crucible temperature profile, shown in Figure 7.14(a), is chosen cooler than the previous profile used in Figure 7.9. Using a lower crucible wall temperature should reduce the melt heat flux q_m and produce a (radially) larger crystal. We attempt to offset this effect by imposing a surrounding gas temperature that is warmer than the previous computed

value, shown in Figure 7.14(b). A warmer gas temperature means less heat can be extracted from the crystal and radial growth will be suppressed. In this instance, it is unclear what the resulting crystal shape should be. The resulting crystal geometry and temperature profiles are presented in Figure 7.15, again on 0.25 time intervals.

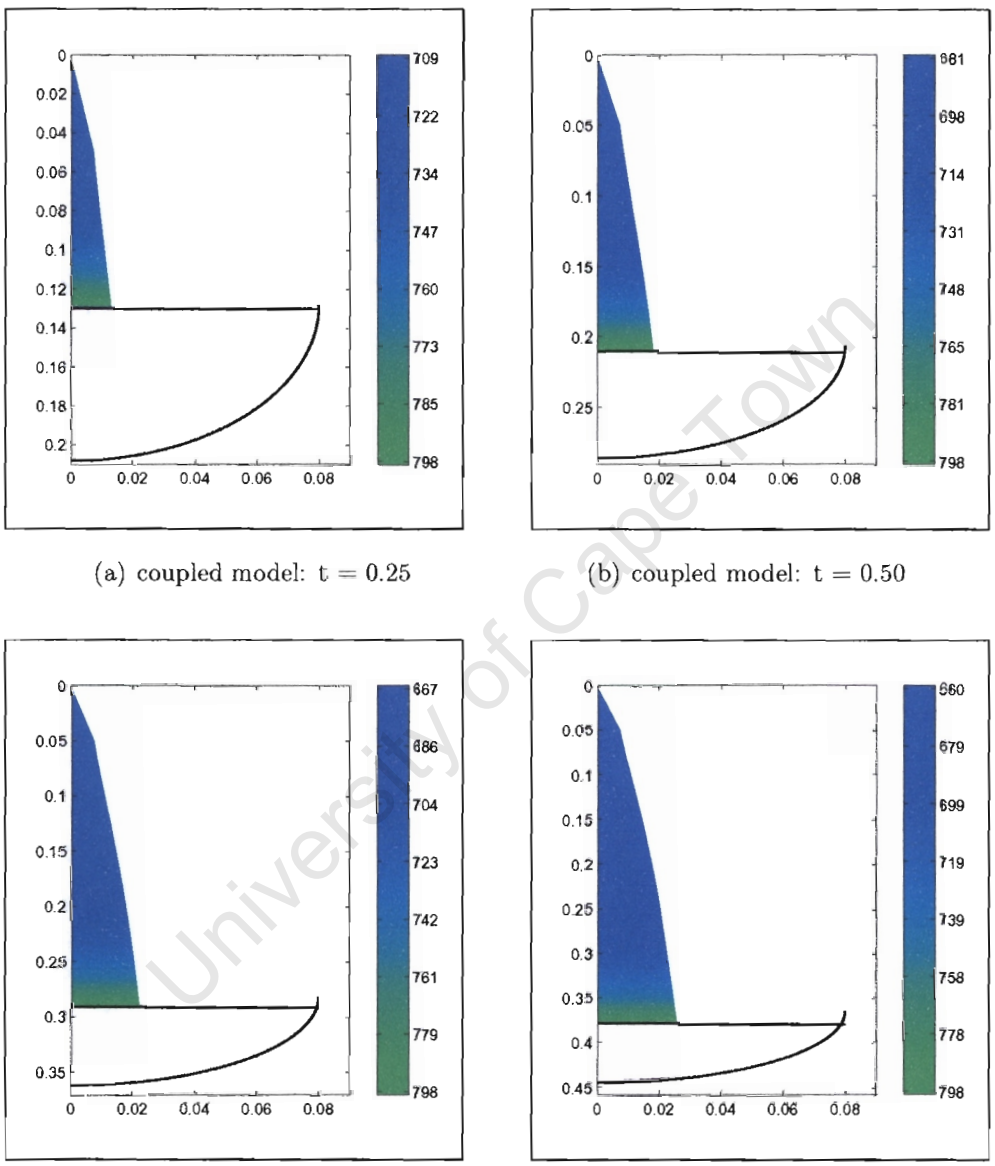

(a) coupled model: t = 0.25

(b) coupled model: t = 0.50

(c) coupled model: t = 0.75

(d) coupled model: t = 1.0

Figure 7.15: Crystal calculations coupled with melt

The result is a smaller crystal with more curvature. This is due to the fact that the gas temperature was increased excessively to account for the lower crucible

temperature.

The profiles we used were arbitrarily chosen to demonstrate the capabilities of our overall process model. We are now able to show the effect of changing process parameters on solidification and present in detail how the crystal shape will be affected.

7.6 Summary

This completes our mathematical model of the Czochralski growth process. A fully coupled model was derived that describes the crystal growth including the melt dynamics. Results were presented that calculated the following profiles: crucible wall temperatures, surrounding gas temperatures and the radial growth.

A final set of calculations were performed with specified crucible wall and gas temperature profiles, enabling the new crystal shape to be obtained. The sample calculations that we performed are hypothetical, but should be used with measured data. Our purpose was to show that given reasonable input data or process parameters we can compute the resulting crystal geometry and temperature.

In summary, this approach allows operators/engineers to have a completely self-contained process model without any estimated parameters. The fluid mechanics and a variable gas temperature can even be included.

Chapter 8

Conclusions and Future Work

8.1 Solidification

It was shown in §2.2 that the time dependence of the crystal temperature profile could be neglected if $\epsilon_x = \frac{\rho_s c_s \hat{R}_x \hat{V}_b}{2H_{gs}\hat{L}_x} \ll 1$. Physically, this implies the quasi-steady assumption is valid for high-aspect ratio (length/radius) crystals that are pulled very slowly. Since there was evidence that the temperature varied little in the radial direction the temperature field was reduced from 2D axisymmetric to 1D in the axial direction. The beauty of these simplifications is that only a second order ODE needs to be solved to obtain the crystal axial temperature profile, instead of a 2D, time-dependent PDE.

A quasi-steady solidification model was derived in §2.3 for InSb that assumed a crystal of either constant (cylindrical) or varying radius. The cylindrical case enabled analytical expressions to be extracted, in particular the maximum and ideal crystal pull rates. Under typical growth conditions for InSb, strong agreement was obtained between the quasi-steady and time dependent solutions. The quasi-steady assumption was validated by comparing results to a numerical solution that included the

time dependence. The analysis in §2.3.2 was devoted to conical crystals, since InSb crystals grown in the laboratory are highly conical in shape, and this assumption simplifies the mathematical expressions for the solidification. Arbitrarily shaped crystals could also be solved for using this method.

This solidification model can be used by engineers to develop heating profiles, predict crystal growth and examine other process parameters. The ease of use and rapid calculation are also convenient in the case where the engineer is interested in coupling the solidification model to a melt calculation.

8.2 Fluid Mechanics

In Chapter 3, the governing equations for the crucible melt were examined. It was determined by a scale analysis in §3.4 that a buoyant boundary layer is likely to form at the crucible wall, and a momentum boundary layer under the crystal. This is difficult to prove but the Finite Element results in §6.2, indicate it is definitely plausible. The asymptotic model in Chapter 4 is an idealization of the flow field based on the scale analysis. The agreement of the temperature gradient for Pr = 0.5 was weak, but this model is intended for melts with Pr$\ll$ 1. It should be made clear that there is currently no other way of estimating the melt heat flux without resorting to CFD. The model we have constructed is not highly accurate at larger Prandtl numbers, but does provide an estimate of the heat transfer to the crystal. The agreement of the rotational effects was much stronger, largely because the rotational velocity is not assumed 1D across the entire crystal, as is the temperature. The crystal boundary layer clearly affects the heat transfer, but not to such an extent that it is completely dominant. This mild effect is very difficult to capture mathematically. The coupled boundary layer model provides a rapid calculation of the heat flux to the crystal, which is convenient for coupling to a solidification model.

A very interesting feature was predicted by the asymptotic model in the crucible

boundary layer equations. If sufficient counter rotation is present, the location where the radial and axial velocities would switch direction is predicted to be at the midpoint along the crucible. This was shown in the quasi-steady solutions in §7.2, where the biaxial flow patterns formed towards the end of the growth period. The location of the flow reversal happens to be closest to the crystal, which may disrupt uniform growth. A cylindrical crucible would make this reversal region at the bottom corner, much further away from the crystal. It would also lessen the impact of the decreasing fluid height, since the radius would be constant.

The Finite Element solution presented in Chapter 5 provided tremendous insight into the melt dynamics and the effect of the crucible/crystal rotation. In §6.2, it was shown that if the crystal and crucible rotation are around the same magnitude, a single convective cell forms inside the crucible. It was also clear that if either rotation dominated, the flow field would split into a different flow pattern consisting of a double convection cell.

The double convection cell is probably not a desirable feature for the melt, particularly if this causes instabilities. In the Czochralski crystal growth process consistency is needed to grow large crystals and fluctuations are likely to disrupt regular growth. It is clear from the quasi-steady Finite Element results that this transition to the crystal dominated flow field is certain to occur. The shape of the temperature gradient across the crystal changes significantly, which will produce large radial stresses in the crystal, inducing defects and other irregularities.

8.3 Coupled Model

In Chapter 7 we coupled the solidification model from Chapter 2 with the asymptotic melt calculation developed in Chapter 4. The coupled model is useful for evaluating dynamic parameters of the crystal growth process. This is a novel calculation that enables a solidification model to be dependent on the melt and crucible parameters.

We also attempted to show the usefulness of the overall process model without any actual grower temperature measurements. First, we specified the crystal shape, since it was accurately known, to calculate a realistic crucible wall temperature profile. We then modified the crucible wall temperature profile and let the surrounding gas temperature vary.

Finally, we used hypothetical crucible wall and gas temperature profiles to obtain the resulting crystal shape. The results themselves are not important, but we showed the capability to take transient process parameters and calculate the final crystal shape.

The overall process model could be used to vary other parameters such as the crystal or crucible rotation rates. If desired, heat transfer between the melt and gas could easily be added. Our intention was to demonstrate the capabilities of the calculation and leave the details to the industrialists.

8.4 Future Work

One aspect that would have made this work more applicable to an industrial setting would have been experimental or process data for the crystal grower apparatus. For instance, an estimate of the crucible and ambient gas temperatures would ensure that the profiles are indeed realistic.

One of the important features that was neglected in this work is the crystal/melt interface shape. This location was assumed horizontal to simplify the calculation. The pressure gradient in the crystal boundary layer equations could perhaps be used to predict the melt interface shape. In actual fact there is surface tension and a meniscus at the edge of the crystal. These features likely contribute to the radial growth rate of the crystal and should also be studied.

More insight into the asymmetry of the crystal growth would likely lead to a better understanding of InSb growth. We assumed 2D axisymmetry for our crystals, mainly

to satisfy an energy balance. A fundamental study into the nature of the asymmetry and the forces that maintain it would be useful for calculating the radial growth for asymmetrical crystal.

Another interesting extension of this model would be to incorporate it as control software for the grower apparatus. The pull speed could be based on temperature measurements on the crucible wall. The rotation rates could be dynamically controlled according to the crystal size and melt height. It would be interesting to see if combining all of these features could improve current crystal growth and even allow growers to produce larger InSb crystals.

Appendix A

Crucible Boundary Layer Equations Derivation

This section is devoted to filling in some of the steps in §4.3.2. We begin at the definition of the stream function and carry on with a detailed derivation of the boundary layer equations (4.22)-(4.24).

A.1 Similarity Solution

Recall, the stream function $\psi(n, s)$ is defined such that it will satisfy the continuity equation (4.14) identically:

$$u_s = -\frac{1}{X}\frac{\partial \psi}{\partial n} \qquad u_n = \frac{1}{X}\frac{\partial \psi}{\partial s}, \tag{A.1}$$

here X denotes the transformed radial coordinate $X = r_b + (s - s_0)\cos\phi$, and notice

$$\frac{\partial X}{\partial n} = 0 \qquad \frac{\partial X}{\partial s} = \cos\phi \qquad \frac{\partial}{\partial s}\left(\frac{1}{X}\right) = -\frac{\cos\phi}{X^2} \tag{A.2}$$

It is necessary to transform equations (4.14)-(4.18) from (n, s) in terms of the similarity variables (η, ξ). This requires the following substitutions (see Bejan [51] or

Davidson [58] for the details):

$$\eta = \frac{n}{s^{1/4}} \qquad \xi = s, \tag{A.3}$$

where the differential operators in terms of (η, ξ) become

$$\frac{\partial}{\partial n} = \frac{1}{s^{1/4}}\frac{\partial}{\partial \eta} \qquad \frac{\partial^2}{\partial n^2} = \frac{1}{s^{1/2}}\frac{\partial^2}{\partial \eta^2} \tag{A.4}$$

$$\frac{\partial}{\partial s} = -\frac{n}{4s^{5/4}}\frac{\partial}{\partial \eta} + \frac{\partial}{\partial \xi} \tag{A.5}$$

$$\frac{\partial^2}{\partial n \partial s} = -\frac{1}{4s^{5/4}}\frac{\partial}{\partial \eta} - \frac{n}{4s^{3/2}}\frac{\partial^2}{\partial \eta^2} + \frac{1}{s^{1/4}}\frac{\partial^2}{\partial \eta \partial \xi}. \tag{A.6}$$

A.1.1 S-Momentum Equation

First, we will convert the s-momentum equation (4.17)

$$u_n\frac{\partial u_s}{\partial n} + u_s\frac{\partial u_s}{\partial s} - \mathrm{Pr}\frac{\partial^2 u_s}{\partial n^2} = \frac{(u_\theta^2 - u_{\theta_m}^2)\cos\phi}{X} + (T - T_m)\sin\phi, \tag{A.7}$$

in terms of the stream function. From this point forward, subscripts denote partial differentiation with respect to that variable. Substituting for the stream function into the left-hand side of (4.17) gives:

$$-\frac{\psi_n}{X}\left(-\frac{\psi_n}{X}\right)_s - \frac{1}{X^2}\psi_s\psi_{nn} + \mathrm{Pr}\left(\frac{\psi_n}{X}\right)_{nn}, \tag{A.8}$$

which can be written as

$$\frac{1}{X^2}(\psi_n\psi_{ns} - \psi_s\psi_{nn}) - \frac{\cos\phi}{X^3}\psi_n^2 + \mathrm{Pr}\frac{\psi_{nnn}}{X}. \tag{A.9}$$

Then we change variables from (n, s) to the similarity variables (η, ξ):

$$\begin{aligned}&\frac{\psi_\eta}{X^2\,\xi^{1/4}}\left[\frac{\psi_{\eta\xi}}{\xi^{1/4}} - \frac{\psi_{\eta\eta}\eta}{4\xi^{5/4}} - \frac{\psi_\eta}{4\xi^{5/4}}\right]\\ &-\frac{\psi_{\eta\eta}}{X^2\xi^{1/2}}\left[\psi_\xi - \frac{\psi_\eta\eta}{4\xi}\right] - \frac{\psi_\eta^2\cos\phi}{X^3\xi^{1/2}} + \mathrm{Pr}\frac{\psi_{\eta\eta\eta}}{X\xi^{3/4}}.\end{aligned} \tag{A.10}$$

Then it is necessary to define $f(\eta)$ in terms of the stream function. This is also part of the stream function and the reader is referred to [51, 58] for details. We proceed by using

$$\psi = f(\eta)\,\xi^{3/4}, \tag{A.11}$$

and note

$$\psi_\eta = f' \, \xi^{3/4} \qquad \psi_{\eta\eta} = f'' \, \xi^{3/4} \tag{A.12}$$

$$\psi_\xi = \frac{3}{4}\frac{f}{\xi^{1/4}} \qquad \psi_{\xi\eta} = \frac{3}{4}\frac{f'}{\xi^{1/4}} \tag{A.13}$$

here ' denotes differentiation with respect to η, ie $f' = \frac{df}{d\eta}$.

Finally, we change the stream function to f, which gives the following for (A.10)

$$\frac{1}{X^2}\left(f'\left[-\frac{1}{4}f' + \frac{3}{4}f'\right] - \frac{3}{4}f''f - \frac{\cos\phi \; \xi (f')^2}{X}\right) + \mathrm{Pr}\frac{f'''}{X} \tag{A.14}$$

The final equation can be rewritten as:

$$\begin{aligned} X\mathrm{Pr}f''' - \frac{3}{4}f''f + (f')^2\left(\frac{1}{2} - \frac{\cos\phi \; \xi}{X}\right) \\ = X\cos\phi(u_\theta^2 - u_{\theta\infty}^2) + X^2\sin\phi(T - T_m), \end{aligned} \tag{A.15}$$

which is the same form as in (4.22).

A.1.2 Energy Equation

Recall, the first-order energy equation (4.18)

$$u_n\frac{\partial T}{\partial n} + u_s\frac{\partial T}{\partial s} = \frac{\partial^2 T}{\partial n^2} \tag{A.16}$$

Substituting the stream function into the above equation yields:

$$-\frac{\psi_n T_s}{X} + \frac{\psi_s T_n}{X} = T_{nn} \tag{A.17}$$

Changing from (n, s) to (η, ξ) results in

$$\frac{1}{X}\left(-\frac{\psi_\eta}{\xi^{1/4}}\left[-\frac{\eta}{4\xi}T_\eta + T_\xi\right] + \frac{T_\eta}{\xi^{1/4}}\left[-\frac{\eta}{4\xi}\psi_\eta + \psi_\xi\right]\right) = \frac{1}{\xi^{1/2}}T_{\eta\eta} \tag{A.18}$$

Simplifying yields,

$$\frac{1}{X}(T_\eta\psi_\xi - T_\xi\psi_\eta) = \frac{1}{\xi^{1/4}}T_{\eta\eta} \tag{A.19}$$

Converting the streamfunction to $f(\eta)$, gives the result

$$T''X = \frac{3}{4}f \; T' - f'\xi T_\xi \tag{A.20}$$

A.1.3 θ-Momentum Equation

Recall, the momentum equation in the azimuthal direction (θ-direction) (4.16):

$$u_n \frac{\partial u_\theta}{\partial n} + u_s \frac{\partial u_\theta}{\partial s} - \Pr \frac{\partial^2 u_\theta}{\partial n^2} = -\frac{u_s u_\theta \cos\phi}{X} \tag{A.21}$$

By similar derivation for the energy equation, changing to stream function gives:

$$\frac{1}{X\xi^{1/4}}(u_{\theta,\eta}\ \psi_\xi - u_{\theta,\xi}\ \psi_\eta) - \frac{\Pr}{\xi^{1/2}} u_{\theta,\eta\eta} = \frac{u_\theta \cos\phi\ \psi_\eta}{X^2 \xi^{1/4}} \tag{A.22}$$

Substituting for $f(\eta)$ gives the following

$$\frac{3}{4}\frac{f\ u_{\theta,\eta}}{X\xi^{1/2}} - \frac{1}{X} f' \xi^{1/2}\ u_{\theta,\xi} - \frac{f'\xi^{1/2}\cos\phi u_\theta}{X^2} = \frac{\Pr u_{\theta,\eta\eta}}{\xi^{1/2}} \tag{A.23}$$

$$\frac{3}{4} f\ u_{\theta,\eta} - f'\xi\left(u_{\theta,\xi} + \frac{\cos\phi\ u_\theta}{X}\right) = X\Pr u_{\theta,\eta\eta} \tag{A.24}$$

A.1.4 Summary

The 3 similarity equations are presented below

$$X\Pr f''' - \frac{3}{4} f'' f + (f')^2\left(\frac{1}{2} - \frac{\cos\phi\ \xi}{X}\right) = X\cos\phi(u_\theta^2 - u_{\theta\infty}^2) + X^2 \sin\phi(T - T_m)$$

$$T_{\eta\eta} X = \frac{3}{4} f\ T_\eta - f'\xi T_\xi$$

$$\frac{3}{4} f\ u_{\theta,\eta} - f'\xi\left(u_{\theta,\xi} + \frac{\cos\phi\ u_\theta}{X}\right) = X\Pr u_{\theta,\eta\eta}$$

Bibliography

[1] J. Czochralski, "Ein neues verfahren zur messung des kristallisations-geschwindigkeit der metalle [A new method for the measurement of crystallization rate of metals]," *Z. Physik. Chem.*, **92**, 219-224 (1918).

[2] J. Czochralski, *Zeitschrift des Vereins Deutscher Ingeneurie*, **61**, 345-349 (1917).

[3] J. Czochralski, *Giesserei Zeitung*, **18**, 85-91 (1921).

[4] J. Czochralski, *Moderne Metallkunde in Theorie und Praxis*, Springer, Berlin (1924).

[5] W.E. Buckley, *Crystal Growth*, Wiley, New York (1951).

[6] H.J. Scheel, "Historical aspects of crystal growth technology," *Journal of Crystal Growth*, **211**, 1-12 (2000).

[7] P. E. Tomaszewski, "Jan Czochralski - Father of the Czochralski method (Letter to the Editor)," *Journal of Crystal Growth*, **236**, 1-4 (2002).

[8] G.K. Teal and J.B. Little, "Growth of germanium single crystals," *Physics Review*, **78**, 647-654 (1950).

[9] G.K. Teal and J.B. Little, *Bulletin of the American Physics Society*, **25**, 16-20 (1950).

[10] B. Micklethwaite, *Bulk Crystal Growth of Electronic, Optical & Optoelectronic Materials*, "Chapter 5: Bulk Growth of InSb and Related ternary Alloys," John Wiley & Sons, London (2004).

[11] Hurle, D.T.J. *Handbook of Crystal Growth*, 1 & 2, North-Holland, Amesterdam (1994).

[12] C.W. Lan, "Recent progress of crystal growth modeling and growth control," *Chemical Engineering Science*, **59**, 1437 - 1457 (2004).

[13] V.V. Kalaev, I.Yu. Evstratova, and Yu.N. Makarov, "Gas flow effect on global heat transport and melt convection in Czochralski silicon growth," *Journal of Crystal Growth*, **249**, 87-99 (2003).

[14] D.P. Lukanina, V.V. Kalaev, Yu.N. Makarov, T. Wetzelc, J. Virbulisc and W. von Ammonc, "Advances in the simulation of heat transfer and prediction of the melt-crystal interface shape in silicon CZ growth," *Journal of Crystal Growth*, **266**, 20-27 (2004).

[15] L. J. Atherton, J. J. Derby and R. A. Brown, "Radiative heat exchange in Czochralski crystal growth," *Journal of Crystal Growth*, **84**, 57-78 (1987).

[16] G. Muller and J. Friedrich, "Challenges in modeling of bulk crystal growth," *Journal of Crystal Growth*, **266**, 1-19 (2004).

[17] E. G. Tsvetkov and V. I. Tyurikov, "Specific features of seeding and growth of bulk polar crystals," *Journal of Crystal Growth Volume*, **217**, 138-144 (2000).

[18] N. Kobayashi, "Computational simulation of the melt flow during Czochralski growth," *Journal of Crystal Growth*, **43**, 357-363 (1978).

[19] W. E. Langlois, "Convection in Czochralski growth melts," *Journal of Physico Chemical Hydrodynamics*, **2**(4), 245-261 (1981).

[20] B. Basu, S. Enger, M. Breuer and F. Durst, "Three-dimensional simulation of flow and thermal field in a Czochralski melt using a block-structured finite-volume method," *Journal of Crystal Growth*, **219**, 123-143 (2000).

[21] S. Enger, B. Basu, M. Breuer and F. Durst, "Numerical study of three-dimensional mixed convection due to buoyancy and centrifugal force in an oxide melt for Czochralski growth, " *Journal of Crystal Growth*, **219**, 144-154 (2000).

[22] C. Wagner and R. Friedrich, "Direct numerical simulation of momentum and heat transport in idealized Czochralski crystal growth configurations," *International Journal of Heat and Fluid Flow*, **25**, 431-443 (2004).

[23] N. Van den Bogaert and F. Dupret, "Dynamic global simulation of the Czochralski process I. Principles of the method," *Journal of Crystal Growth*, **171**, 65-76 (1997).

[24] D.P. Lukanina, V.V. Kalaev, Yu.N. Makarovb, T. Wetzelc, J. Virbulisc and W. von Ammon, "Advances in the simulation of heat transfer and prediction of the melt-crystal interface shape in silicon CZ growth," *Journal of Crystal Growth*, **266**, 20-27 (2004).

[25] K. Kakimoto, "Flow instabilities during crystal growth from the melt," *Progresses in Crystal Growth and Characterization*, **30**, 191-215 (1995).

[26] D. T. J. Hurle, "Dynamics, stability and control of Czochralski growth," *Journal of Crystal Growth*, **128**, 15-25 (1993).

[27] D. T. J. Hurle, G. C. Joyce, M. Ghassempoory, A. B. Crowley and E. J. Stern, "The dynamics of czochralski growth Journal of Crystal Growth," **100**, 11-25 (1990).

[28] A.B. Crowley, "Mathematical modeling of heat flow in Czochralski crystal pulling, " *IMA Journal of Applied Mathematics*, **30**, 173-189 (1983).

[29] O.A. Louchev, S. Kumaragurubaran, S. Takekawa and K. Kitamura, "Thermal stress inhibition in double crucible Czochralski large diameter crystal growth," *Journal of Crystal Growth*, **274**, 307-316 (2005).

[30] C.S. Bohun, I. A. Frigaard, H. Huang and S. Liang, "A Semi-Analytical Model for InSb Crystal Growth," *SIAM*, in review.

[31] X. Wu, X. Geng and Z. Guo, "Fundamental study of crystal/melt interface shape change in Czochralski crystal growth," *Journal of Crystal Growth*, **169**, 786-794 (1996).

[32] J.J. Derby and R.A. Brown, "On the Quasi-Steady-State Assumption in Modeling Czochralski Crystal Growth," *Journal of Crystal Growth*, **87**, 251-260 (1988).

[33] F. Dupret and N. Van Den Bogaert, *Handbook of Crystal Growth, Vol. 2b: Bulk Crystal Growth, Growth Mechanisms and Dynamics*, North-Holland, Amsterdam (1994).

[34] A. van der Hart and W. Uelhoff, "Macroscopic modelling of crystal growth I: heat flow," *Journal of Crystal Growth*, **51**, 257-266 (1981).

[35] C. Schvezov, I. V. Samarasekera and F. Weinberg, "Mathematical modelling of the liquid encapsulated Czochralski growth of GaAs I - Heat flow model," *Journal of Crystal Growth*, **84**, 212-218 (1987).

[36] Y.A. Tatarchenko, *Shaped Crystal Growth*, Kluwer Academic Publishers, Boston, (1993).

[37] O.A. Louchev, S. Kumaragurubaran, S. Takekawa and K. Kitamura, "Thermally induced effects during initial stage of crystal growth from melts," *Journal of Crystal Growth*, **273**, 320-328 (2004).

[38] V.L. Indenbom, I.S. Jitomirski and T.S. Chebanova, *Kristallographiya*-in Russian, **18**, 39-49 (1973).

[39] Sumito Metals website, http://www.sumitomometals.co.jp/e/business/silicon.html. Last accessed 02/12/06.

[40] T. G. Myers and D. W. Hammond, "Ice and water film growth from incoming supercooled droplets, " *International Journal of Heat and Mass Transfer*, **42**, 2233-2245 (1999).

[41] N. Kobayashi, "Steady state flow in a Czochralski crucible," *Journal of Crystal Growth*, **147**, 382-389 (1995).

[42] U. Ascher, R. Mattheij and R. Russell, *Numerical solution of Boundary Value Problems for Ordinary Differential Equations*, SIAM, Philadelphia (1995).

[43] J. Crank, *Free and Moving Boundary Problems*, Oxford University Press, New York (1984).

[44] S. C. Gupta, E. Laitinen and T. Valterri, "Moving Grid Scheme for Multiple Moving Boundaries, " *Comput. Methods Appl. Mech. Engrg.*, **167**, 345-353 (1998).

[45] J. W. Thomas , *Numerical Partial Differential Equations - Finite Difference Methods*, Springer Texts in Applied Mathematics, Vol. 22 (1995).

[46] G. K. Batchelor, *An Introdution to Fluid Mechanics*, Cambridge University Press, Cambridge (2000).

[47] D. Givoli, J. E. Flaherty and M. S. Shephard, "Simulation of Czochralski melt flows using parallel adaptive finite element procedures," *Modelling Simul. Mater. Sci. Eng.*, **4**, 623-639 (1996).

[48] C. Wagner and R. Friedrich, "Direct numerical simulation of momentum and heat transport in idealized Czochralski crystal growth configurations," *International Journal of Heat and Fluid Flow*, **25**, 431-443 (2004).

[49] Y. Li, Y. Akiyama, N. Imaishi and T. Tsukada, "Global analysis of a small Czochralski furnace with rotating crystal and crucible," *Journal of Crystal Growth*, **255**, 81-92 (2003).

[50] J. Choi and H. Jin, "Suppression of temperature oscillation in Czochralski convection by superimposing rotating flows, " *International Jounarl of Heat and Mass Transfer*, **40**(7), 1667-1675 (1997).

[51] A. Bejan, *Convection Heat Transfer*, Second Edition, John Wiley and Sons (1995).

[52] D. J. Acheson, *Elementary Fluid Mechanics*, "Chapter 8: Boundary Layers," Oxford University Press, New York (1990).

[53] J. H. Jeong, J. Oh and I. S. Kang "Analytical studies on the crystal-melt interface shape in the Czochralski process," *Journal of Crystal Growth*, **177**, 303-314 (1997).

[54] P. A. Davidson, "Similarities in the Structure of Swirling and Buoyancy-Driven Flows," *Journal of Fluid Mechanics*, **252**, 357-382 (1993).

[55] A. A. Wheeler, "Boundary layer models in Czochralski crystal growth," *Journal of Crystal Growth*, **97**, 64-75 (1989).

[56] R. Irizarry-Rivera and Warren D. Seider, "Model-predictive control of the Czochralski crystallization process Part II. Reduced-order convection model," *Journal of Crystal Growth*, **178**, 612-633 (1997).

[57] T. von Karman, "Uber Laminare und Turbulente Reibung," *Zeitschrift Angew. Math. Mech*, **1**, 233-252 (1921).

[58] D. Kinnear and P. A. Davidson, "A Simple Method for Estimating Velocity Deistributions in Swirling Flows," *Journal of Fluids Engineering: Transactions of the ASME*, **116**, 694-701 (1994).

[59] J. R. Lloyd, and E. M. Sparrow, "Combined Forced and Free Convection Flow on Vertical Surfaces," *International Journal of Heat and Mass Transfer*, **13**, 434-438 (1969).

[60] D.T.J. Hurle, *Crystal Pulling from the Melt*, Springer-Verlag, Berlin (1993).

[61] H. Blasius, "Grenzschichten in Flussigkeiten mit kleiner Reibung," *Zeitschrift Math. Phys.*, **56**, 1-37 (1908).

[62] E. Pohlhausen, "Der Warmeaustausch zwischen festen Korpern und Flussigkeiten mit kleiner Reibung und kleiner Warmeleitung, " *Zeitschrift Angew. Math. Mech.*, **1**, 115-121 (1921).

[63] M. H. Rogers and G. N. Lance, "The Rotationally Symmetric flow of a Viscous Fluid in the Presence of a Rotating Disk," *Journal of Fluid Mechanics*, **7**, 617-631 (1960).

[64] J.C. Lagarias, J. A. Reeds, M. H. Wright, and P. E. Wright, "Convergence Properties of the Nelder-Mead Simplex Method in Low Dimensions," *SIAM Journal of Optimization*, **9**, 112-147 (1998).

[65] U. Ascher, R. Matthew and R. Russell, *Numerical Solution of Boundary Value Problems for Ordinary Differential Equations*, SIAM, Philadelphia (1995).

[66] S.G. Mikhlin, *Variational Methods in Mathematical Physics*, (translated from Russian by T. Boddington) Pergamon Press, Oxford (1964).

[67] B.A. Finlayson, *The Method of Weighted Residuals and Variational Principles*, Academic Press, New York (1972).

[68] J. N. Reddy and D. K. Garling, *The Finite Element Method in Heat Transfer and Fluid Dynamics*, Third Edition, McGraw-Hill, New York (2005).

[69] C. F. Ollivier-Gooch, *GRUMMP: Generation and Refinement of Unstructured Mixed-element Meshes in Parallel*, Department of Mechanical Engineering, University of British Columbia, details at: http://tetra.mech.ubc.ca.

[70] R. L. Sani, P. M. Gresho, R. L. Lee and D. F. Griffiths, "The cause and cure of the spurious pressures generated by certain FEM soultions for the incompressible Navier-Stokes equations: part I," *International Journal of Numerical Methods in Fluids*, **1**, 17-43 (1981).

[71] R. L. Sani, P. M. Gresho, R. L. Lee and D. F. Griffiths, "The cause and cure of the spurious pressures generated by certain FEM solutions for the incompressible Navier-Stokes equations: part II," *International Journal of Numerical Methods in Fluids*, **1**, 171-204 (1981).

[72] C. P. Taylor and P. Hood, "A numerical solution of the Navier-Stokes Equations using the FEM technique," *Computers and Fluids*, **1**, 73-100 (1973).

[73] J. N. Reddy, *An Introduction to the Finite Element Method*, Third Edition, McGraw-Hill, New York (2005).

[74] D. K. Gartling and E. B. Becker, "Finite element analysis of viscous, incompressible fluid flow : Part 1 : Basic methodology," *Computer Methods in Applied Mechanics and Engineering*, **8**, 51-60 (1976).

[75] K. Kakimoto and H. Ozoe, "Heat and mass transfer during crystal growth," *Computational Materials Science*, **10**, 127-133 (1998).